A STUDY ON FEMTOSECOND LASER IN GLAUCOMA TREATMENT: ENERGY DEPOSITION AND THERMAL INCREASE

NANYANG TECHNOLOGICAL UNIVERSITY

A STUDY ON FEMTOSECOND LASER IN GLAUCOMA TREATMENT: ENERGY DEPOSITION AND THERMAL INCREASE

HOU DONGXIA

HOU DONGXIA

SCHOOL OF MECHANICAL & AEROSPACE ENGINEERING

2007

2007

A Study on Femtosecond Laser in Glaucoma Treatment: Energy Deposition and Thermal Increase

Hou Dongxia

School of Mechanical & Aerospace Engineering

A thesis submitted to the Nanyang Technological University
in fulfilment of the requirement for the degree of
Doctor of Philosophy

2007

ABSTRACT

The generation of femtosecond pulsed laser offers completely new possibilities for multiple technical applications. Due to its non-contact processing, extremely high intensity and ultra short pulse duration, it provides precise control of material removal with negligible thermal damage. In ophthalmology, the use of femtosecond lasers is receiving more attention than ever. It opens the highly beneficial possibilities for minimized side effects during the surgery process, and one of the specific areas is laser surgery in glaucoma treatment.

Much work has been done for femtosecond laser application in ophthalmology. Some prospective results have been achieved. Meanwhile, the sophisticated interaction mechanism hampers femtosecond lasers' clinical application, and its potential in glaucoma treatment is still at the early stage.

In this research, it was the first time that a modified moving breakdown theory was applied to study laser-induced optical breakdown in ocular tissue. It aimed to apply femtosecond laser in iridotomy surgery. Based on this theory, optical breakdown and the corresponding thermal increase were studied. The femtosecond laser-induced moving breakdown model was introduced to simulate the optical breakdown threshold; the Heat Affected Zone model was used to analyze temperature increases in water and ocular tissues.

Cyclophotocoagulation is another main method to treat glaucoma. To improve the efficiency of cyclophotocoagulation procedure, a Monte Carlo program was developed and light propagation in multilayered ocular tissue was studied. The

optical properties of ocular tissues for simulation were measured by a UV-VIS-NIR spectrophotometer; an inverse adding-doubling algorithm was used to calculate the absorption coefficient and the scattering coefficient. The transmission, reflection and absorption of the light were statistically calculated.

Besides the simulation, experimental study is also essential for a novel setup development and for clinical application.. In this research, the important laser parameters (wavelength, pulse duration, numerical aperture, pulse intensity, and pulse numbers) and their effects on the ablation process in the tissue were studied in this research. Using a femtosecond Ti:Sapphire laser system, the optical breakdown during the femtosecond laser-ocular tissue interaction and the steady state ablation were investigated.

To reduce the cost of the laser surgery setup and minimize certain intra tissue damage, nano Joule processing in ocular tissues was studied using a femtosecond oscillator. Pulse intensity thresholds in water with two laser sources (the femtosecond amplifier and the femtosecond oscillator) were investigated. Nonlinear propagation of the femtosecond pulses in ocular tissue was studied. It is important for potential application of nano Joule pulse energy processing with a femtosecond oscillator in ophthalmology.

ACKNOWLEDGEMENTS

I would like to express my deepest gratitude to my supervisors, Professor David Lee Butler and Professor Bryan Ngoi Kok Ann, for their great support and invaluable guidance throughout the period of this research at Nanyang Technological University.

Sincere thanks to all the staffs and students from Metrology Laboratory and Precision Engineering & Nanotechnology (PEN) Center, for their friendly support and helpful suggestion during this research; a particular appreciation is given to Dr. He Liming for her guidance during my first year study, to Dr. Fu Yongqi for his valuable discussion. I also would like to specially thank the entire laser team in PEN Centre for their constructive advice in this research.

Dr. Hoh Sek Tien from Singapore National Eye Center deserves my special thanks and admiration for his valuable knowledge and contribution in the field of glaucoma treatment.

I would like to extend my heartfelt gratitude to Ms. Heng Chee Hoon from the Tissue Engineering Laboratory, School of Mechanical and Aerospace Engineering, Nanyang Technological University, Dr. Jiang Sujia and Mr. Jams from Singapore National Hospital, Dr. Zheng Hongyu from Singapore Institute of Manufacturing Technology (SIMTech), for their generous help that enabled me to carry out the experiments of this research.

I owe great debts of gratitude to Nanyang Technological University for providing the research scholarship and necessary funding that is needed for this project.

Finally, I would like to thank my dearest family and friends, for their support and immense encouragement throughout my study.

TABLE OF CONTENTS

LIST OF ABBREVIATIONS

ABBREVIATIONS	DESCRIPTION
3D	Three Dimensional
ALT	Argon Laser Trabeculoplasty
CABG	Coronary Artery Bypass Grafting
CCD	Charge Coupled Device
CPA	Chirped Pulse Amplification
CPC	Cyclophotocoagulation
ELAN	Extraluminal Laser Angioplasty
IOP	Intraocular Pressure
KLM	Kerr Lens Modelocking
LASIK	Laser in Situ Keratomileusis
MC	Monte Carlo
NA	Numerical Aperture
OCT	Optical Coherence Tomography
PDT	Photodynamic Therapy
PRK	Photorefractive Keratectomy
SEM	Scanning Electron Microscope
SLT	Selective laser trabeculoplasty
TM	Trabecular Meshwork

LIST OF SYMBOLS

SYMBOLS	DESCRIPTION
β	Normalized Pulse Intensity
c	The Velocity of Light in Free Space
$\tilde{\chi}$	Material Dependent Factor
C_p	Specific Heat
d	Sample Thickness
d_r	the Absorption Depth of Radiation
E	Electric Field Strength
e	Electron Charge
ε_0	The Permittivity of Free Space
e_s	Scattering Direction
e'_s	New Scattering Direction
E_{th}	Pulse Energy Threshold
ϕ	The Lens' Effective Diameter
f	The Focal Length of the Lens
fs	Femtosecond
$F_\xi(\xi)$	Cumulative distribution of Random Variable
g	The Anisotropy Factor
h	The Planck's Constant
η_{ava}	the Avalanche Ionization Rate

η_{diff}	The Electron Diffusion Rate
η_{rec}	The Electron Recombination Rate
i	the Ratio of Air Index to Work Medium Index
I	Laser Pulse Intensity
I_0	Incident Light Intensity
I_{th}	Optical Breakdown Threshold Intensity
K	The Thermal Conductivity
k	the Number of Absorbed Photons
λ_0	The Laser Wavelength in Free Space
l_p	The Pulse Length
M	The Mass of the Material Molecule
m	the Rest Mass of an Electron
m'	The Reduced Exciton Mass
μ_a	Absorption Coefficient
μ_s	Scattering Coefficient
μ_s'	The Transport (or Reduced) Scattering Coefficient
μ_t	Total Attenuation Coefficient
μ_x	Directional Cosine along x Axis
μ'_x	New Directional Cosine along x Axis
μ_y	Directional Cosine along y Axis
μ'_y	New Directional Cosine along y Axis
μ_z	Directional Cosine along z Axis
μ'_z	New Directional Cosine along z Axis
N	Pulse Number

n	The Refractive Index of the Medium
ns	Nanosecond
N_z	the Ratio of Pulse Length to Focal Region
P	Output Power
P_{max}	The Pulse Peak Power
P_p	Polarization Vector
ps	Picosecond
P_{th}	Pulse Power Threshold
θ	Deflection Angle
q	Photon survival Chance
θ_f	Focusing Angle
r	Unit Vector
ρ	Electron Density
ρ_{cr}	Electron Density Critical Value
ρ_m	material Density
s	Step Size
$S(x,z,t)$	Heat Source
s_1	Mean Free Path
σ_a	Absorption Cross Section
σ_s	Scattering Cross Section
t	The Pulse Propagation Time
$T(x,z,t)$	Temperature Increase
t_B	The Time at Which the Laser Intensity Reaches the Breakdown Threshold
T_h	Thermal Relaxation Time

τ_{ion}	The Finite Time Required for Momentum Transfer to Electrons via Collisions
τ_p	The Full Width at Half-Maximum Pulse Duration
T_t	Transmission
u	Thermal Diffusivity
ω	The Laser Frequency
W	Photon Weight
$w(z)$	The Beam Radius at Position Z
w_0	Beam Waist
W_{th}	Photon Weight Threshold
ξ	Random Variable
x_m	Light Propagation Depth in the Treated Material
x_r	Unit Vector Along x Axis
xx	Photon's Cartesian Coordinate in x Axis
xx'	Photon's New Cartesian Coordinate in x Axis
ψ	Azimuthal Angle
y_r	Unit Vector Along y Axis
yy	Photon's Cartesian Coordinate in y Axis
yy'	Photon's New Cartesian Coordinate in y Axis
z	Pulse Position During Its Propagation in Medium
z_r	Unit Vector Along z Axis
z_R	Focal Region
zz	Photon's Cartesian Coordinate in z Axis
zz'	Photon's New Cartesian Coordinate in z Axis
$\Phi(x)$	The Dawson's Integral

LIST OF FIGURES

LIST OF TABLES

CHAPTER ONE

INTRODUCTION

1.1 BACKGROUND

The word LASER is an acronym, for Light Amplification by "Stimulated Emission of Radiation". Together with the satellite, the computer and the integrated circuit, it is a symbol of "high technology". Like other technologies, laser affects our lives in many ways, and is growing steadily in importance [1-3]. Its application involves manufacturing, information and communication technologies, environmental technology and life sciences. For instance, it is able to perform heat treatment of high-strength materials, serve as a key component of some communication systems, and provides a special surgical knife for many types of medical procedures.

Lasers today can achieve pulse durations as short as 6×10^{-15} s [4]. These are classified as femtosecond pulse lasers. Due to its high intensity, ultra short pulse duration, and non-contact nature of processing, femtosecond lasers offer completely new possibilities for multiple technical applications with negligible thermal damage. It is widely used for precise and efficient material processing [5].

The femtosecond Ti:Sapphire laser system has unique advantages in biomedical applications. The main advantages are, firstly, the 800 nm wavelength of the Ti:Sapphire laser falls within the absorption window of most tissues, allowing radiation to be focused to a point within the target without damaging the outer

layers (e.g. the cornea). Secondly, the short pulse length causes the radiant energy to be absorbed on a time scale that is much shorter than both thermal diffusion and shock wave propagation. This property confines the thermal and stress extent, thus reducing the region of material damage to the vicinity of the laser focus. Finally, the lower fluence threshold for femtosecond ablation reduces the overall thermal and mechanical load on the tissue [6]. These advantages have attracted interest in the ophthalmologic field.

1.2 MOTIVATION

Glaucoma is one of the leading causes of blindness in adults over the age of 60 [7]. It accounts for 40% of all blindness in Singapore, and it is the second leading cause of blindness in China and the United States [8]. Mechanical compression on and/or decreased blood flow to the optic nerve associated with other factors can lead to glaucoma.

The most commonly practiced conventional surgical procedure is filtering surgery. In this surgery, a channel is cut from the anterior chamber of the eye through the sclera to allow fluid to drain. This procedure generally fails over time due to infection or scarring which is associated with making the incisions.

At present, laser surgery is used in glaucoma treatment due to some advantages, which include:

- It is subsurface surgery, thus the risk of infection is reduced.
- The process is bloodless.

- It causes less operative and postoperative pain.
- It is a quick, convenient procedure, and requires a shorter hospital stay compared to conventional surgery.

There are some risks with the current laser treatment such as post-operative inflammation, pressure spikes, blockage of the drainage angle, cornea cloudiness, etc. All of the above limitations are mainly due to excessive energy being deposited in the ocular tissue; besides removing the desired target, the diffused energy also causes a thermal increase, which results in the side effects in glaucoma treatment. This drawback hampers the laser application in glaucoma treatment.

Several challenges arise from employing lasers in glaucoma surgery:

1. How to overcome the existing risks in current laser glaucoma surgery?
2. What is the femtosecond laser-ocular tissue interaction mechanism, and could femtosecond lasers serve as an effective tool to treat glaucoma?
3. If the femtosecond laser can be used to improve glaucoma surgery outcome, then how to realize it?

The potential of femtosecond laser in glaucoma treatment has been investigated through experimental studies by some researchers [9], and constructive conclusions have been obtained. However, since dehydrated ocular tissues were used in these studies to improve translucency, the optical characteristics of the tissue have been changed. Hence, some uncertainties still exist regarding the applicability of these results in fresh hydrated eyes.

In addition, for the development of new instruments and procedures used for laser surgery, extensive experimental and clinical studies are typically involved.

Computational modeling can help to achieve a deeper understanding of specific laser-medical processes. While in spite of a large number of studies previously carried out [10,11], most of them were in-vitro experimental studies, and the analysis was mostly based on the experimental results rather than statistical simulation. The understanding of the laser parameters was also limited by the experimental condition. Currently, there is no clear understanding of the interaction mechanism.

1.3 OBJECTIVE

The objective of this research is to study the potential of femtosecond laser in glaucoma surgery and ultimately to develop a new femtosecond laser surgery setup for glaucoma treatment. The new setup is expected to overcome or reduce the limitations of the current laser surgical setup, with surgical safety, precision, and efficiency being enhanced.

1.4 SCOPE

This research mainly focuses on the study of energy deposition and thermal damage during femtosecond laser-ocular tissue interaction. Both simulation and in-vitro experimentation were carried out. Corresponding to each stage of this research, the scope is listed below:

- Theoretical modeling for femtosecond laser induced optical breakdown in tissues.
- Optical breakdown threshold prediction based on the femtosecond moving breakdown theory.
- Thermal increase prediction during femtosecond laser-ocular tissue interaction
- The optical properties measurement of ocular tissue.
- Monte Carlo program development for the simulation on light propagation in ocular tissue.
- Investigation of the effects of wavelength, pulse duration, numerical aperture, pulse intensity, and pulse numbers on laser-tissue interaction results.
- Optical breakdown threshold measurement during femtosecond laser-ocular tissue interaction.
- Steady state ablation using a femtosecond Ti:Sapphire laser system.
- The comparison of the optical breakdown threshold in water between two laser sources (a femtosecond amplifier system and a femtosecond oscillator system).
- Nano Joule laser pulse energy processing in ocular tissue with a femtosecond oscillator system.

1.5 ORGANIZATION

The thesis starts with a brief introduction. It represents the background and the motivation for the proposed research, and then brings out the objective and scope.

Chapter 2 consists of the literature review for this research. Firstly, femtosecond laser technology and its applications are reviewed. The limitations of material

processing with long pulse lasers are discussed. Some unique characteristics with femtosecond laser as well as the applications are addressed. Secondly, laser tissue interaction mechanisms will be introduced; femtosecond laser biomedical applications are also presented. Glaucoma and the state-of-the-art laser surgery methods for its treatment are discussed, as well as their advantages and some existing problems. Finally, the potential of applying femtosecond laser in glaucoma treatment will be highlighted.

Chapter 3 provides the theoretical study on the femtosecond laser-ocular tissue interaction mechanism. The moving breakdown theory will be introduced from the classical (nanosecond) model to a modified (femtosecond) model. Compared to the classical model, the modified model can reflect the ultra short laser-biological tissue interaction more factually. Based on the femtosecond laser moving breakdown theory, the intensity threshold and the pulse energy threshold are mathematically deduced. The Heat Affected Zone model will be used to analyze temperature increases both in water and ocular tissues. The results will be compared with that from long pulse lasers.

In chapter 4, the light propagation in ocular tissue during cyclophotocoagulation will be studied. The optical properties of ocular tissues were measured using a UV-VIS-NIR spectrophotometer. A Monte Carlo program was developed for modeling the energy transmission and absorption. The contour of fluence rate, the fluence rate change in the z direction, and the reflection in the radial direction are investigated, and the fractions of absorption, reflection, and transmission are calculated.

In chapter 5, in-vitro experimental investigation is carried out using a femtosecond Ti:Sapphire laser system. The key laser parameters are addressed, including wavelength, pulse duration, numerical aperture, pulse intensity, and pulse numbers. Their effects on ablation process are also discussed. The investigation of the optical breakdown threshold and the steady state ablation is performed.

Chapter 6 represents the study on nano Joule pulse energy processing in ocular tissues with a femtosecond oscillator. The pulse intensity thresholds between a femtosecond amplifier and a femtosecond oscillator are measured and the results are discussed. The light propagation and the simultaneous nonlinear phenomena both in cornea and sclera are investigated.

Finally in Chapter 7, a summary of the research is presented along with conclusions and recommendations for further study.

CHAPTER TWO

LITERATURE REVIEW

2.1 INTRODUCTION

The application of femtosecond lasers for high-quality laser material processing is an exciting new field that has grown rapidly in the past few years [12-15]. Due to their high intensity (>10^{12} W/cm^2), ultra short pulse duration (<1ps), and non-contact nature of processing, femtosecond lasers show great potential for precise and efficient material processing. One prospective application is femtosecond laser glaucoma treatment.

In this chapter, firstly, the current applications and research work performed using femtosecond laser technology are reviewed. The limitations of material processing with long pulse lasers will be addressed, and the characteristics and corresponding advantages with femtosecond lasers are highlighted. Some applications with femtosecond lasers are reviewed, including optical devices, photo electronics, micro fabrication, and biomedical applications. Then, the main laser-tissue interaction mechanisms will be addressed, followed by a review of femtosecond laser surgery applications, and specifically, femtosecond lasers in ophthalmology will be illuminated. Laser glaucoma surgery and some related problems will be discussed in detail. The chapter will conclude by highlighting the potential of femtosecond laser in ophthalmology.

2.2 FEMTOSECOND LASER TECHNOLOGY

2.2.1 LIMITATIONS OF LONG PULSE LASERS

In the case of material processing with conventional long pulse lasers (or more conventional machining tools), heat-diffusion dominates the micromachining process. This introduces numerous undesirable side effects that reduce the quality of the material processing. The reasons are addressed as below:

1. **Reducing efficiency**

   Heat diffusion draws energy away from the work spot, thus reducing the material processing efficiency.

2. **Reducing accuracy**

   Heat diffuses away from the focal spot and melts an area that is much larger than the laser spot size. It is therefore difficult to perform very fine machining, and this reduces the material processing accuracy.

3. **Causing mechanical stress**

   Heat-diffusion causes mechanical stress and can create micro cracks (as shown in Figure 2.1). These cracks may propagate into the bulk of the material causing premature device failure.

4. **Forming shock waves**

   Heat-diffusion is sometimes associated with the formation of surface shock waves. These shock waves can damage nearby device structures or delaminate multilayer materials as illustrated in Figure 2.1.

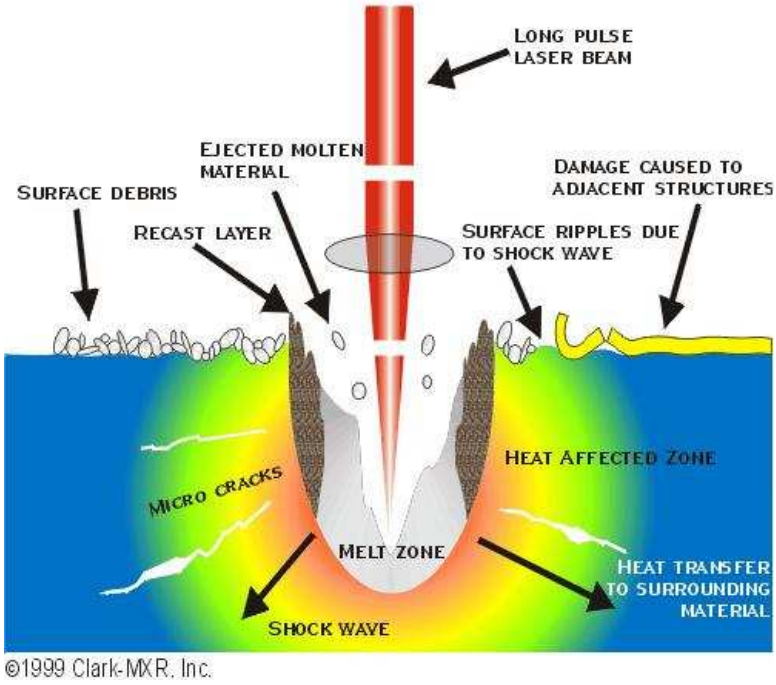

Figure 2.1 Long Pulse Laser-Material Interaction Process [16]

There are other limitations associated with long pulse laser-material processing. For example long pulse lasers cannot readily machine transparent materials. Due to their unique characteristics, femtosecond lasers can overcome the limitations associated with long pulse processing, which are introduced in the following section.

2.2.2 CHARACTERISTICS OF FEMTOSECOND LASERS

Compared with long pulse lasers and other conventional manufacturing techniques, femtosecond lasers can precisely remove material. It can also be used to process a wide range of materials, resulting in negligible thermal damage, and providing the capability for very clean, small features, which make them a promising tool for many applications.

The most striking feature of the femtosecond laser technology is the extreme short duration of the laser pulses ranging from about 10 fs to1 ps. To give an example: Within 100 fs the light travels only as far as a fraction of the diameter of a human hair. For comparison: Within one second the light can surround the earth about 7.5 times. When interacting with material, the duration of the laser pulse is shorter than the minimum heat diffusion time (several ps), as shown in Figure 2.2. Thus the deposited heat has no time to diffuse away from the work spot during the time the laser pulse is irradiating the material, which is a great advantage of femtosecond laser-material interaction. The expectation of ultra high precision and minimized thermal damage can be realized. Furthermore, because the energy does not have time to diffuse away, the efficiency of the machining process is very high.

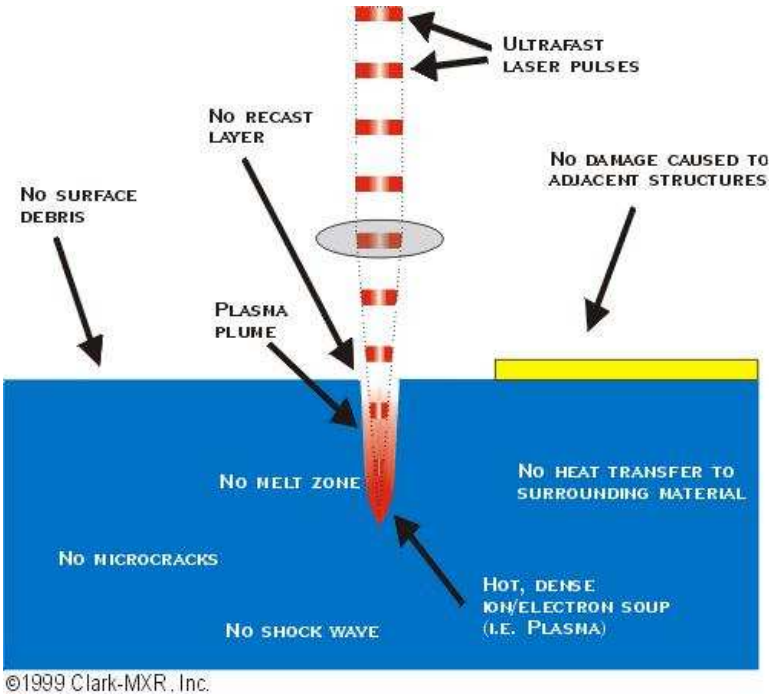

Figure 2.2 Femtosecond Pulse Laser-Material Interaction Process [16]

Another predominant feature of femtosecond pulses is their extremely high intensity. For example, at a pulse width of 100 fs and a focal area of 100 μm^2, pulse energy of 1mJ yields an intensity value of 10^{16} W/cm^2. With such high

intensities, multi-photon effects are easily achieved, allowing a wide range of material treatment. With femtosecond laser pulses, we can therefore process transparent materials, very hard materials, as well as materials with extremely high melting points such as Molybdenum, Rhenium, etc.

At the same time, it is important to note that the femtosecond laser is considerably more expensive compared to long pulse lasers. For instance, the femtosecond Ti:Sapphire laser system used in these experiments costs approximately US$ 430,000 when bought in February 2000; in comparison a YAG laser system at nanosecond pulse duration costs less than US$60,000. This financial limitation slows down the application and proliferation of femtosecond lasers. However, over the past 6 years, the cost of femtosecond laser systems has dropped significantly with a similar system to the one we used now costing 30% less. It is promising that there will be a wide application of femtosecond lasers in the near future.

2.2.3 FEMTOSECOND LASER APPLICATIONS

2.2.3.1 Optical Devices

Femtosecond laser technology is widely applied for machining of optical devices. They are used for telecommunications [17], photonic light wave circuits [18-20], etc.

In the telecommunications industry, fused silica has emerged as a major material of interest. It serves as an excellent host material for optical waveguides in the near infrared region. Micro facets that are machined in the silicon cladding of an optical

fiber are shown in Figure 2.3. The desired micromachining result can be obtained by femtosecond laser technology.

Figure 2.3 Micro Facets Machining in Silica Cladding of an Optical Fiber [13]

Glass is also commonly used in photonics and telecommunication fields. Figure 2.4 shows the comparison between a nanosecond laser drilled hole and a femtosecond laser drilled hole in glass, the hole size is about 115μm. It can be clearly seen from Figure 2.4, the better machining achieved with a femtosecond laser.

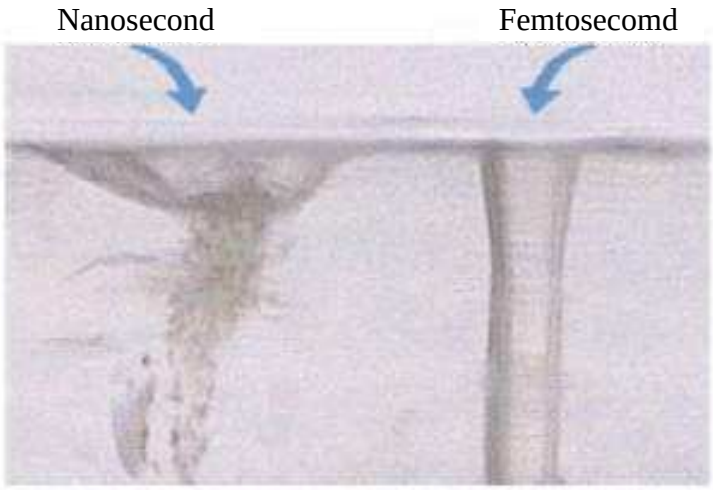

Figure 2.4 Holes Drilled in Glass with Nanosecond- and Femtosecond-Duration Pulses Compared [15]

2.2.3.2 Micro Electronics

Microelectronics application with femtosecond laser covers laser micro machining in integrated circuits, repairing lithographic masks, machining of electro-mechanical devices, etc [13, 21-24].

The use of very thin silicon wafers (50 μm thick and less) can help to increase the circuit density of modern microelectronics. Since these thin wafers are very fragile, conventional mechanical cutting techniques, such as using a diamond saw, are simply not viable. Due to the absence of the heat-affected zone and limited induced mechanical stress, femtosecond laser appears to be a viable alternative cutting method.

Figure 2.5 shows the SEM image of cut edges on a 50 μm thick Silicon wafer from its front and rear sides after 20, 40, 60 80 and 100 passages. The focal spot size and the scanning speed were 4 μm and 300 μm/s, respectively.

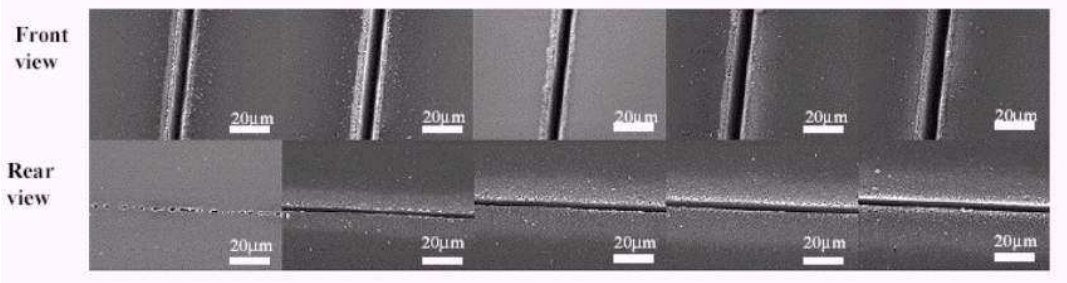

Figure 2.5 SEM Images of Cut Edges on a 50 μm Thick Silicon Wafer from Its Front and Rear Sides Performed at Different Laser Fluences [24]

Figure 2.6 shows an example of femtosecond laser technology in mask reparation applications. It represents a commercial photomask, with 10 μm wide tracks made in a 100 nm thick chrome layer. Although this track width is an order of magnitude

or larger than the smallest features required to be removed from modern masks, it demonstrates the effectiveness of femtosecond pulses in the high quality removal of chrome layers for mask repair applications.

Figure 2.6 A Chrome-on-Quartz Photomask where the Chrome has been Removed using a Femtosecond Laser [13]

2.2.3.3 Micro Fabrication

Due to its non-contact processing, and high precision material removal, femtosecond lasers have the potential to provide a simple fabrication technique. Additional post-processing or special gas environment is not required.

Some microstructures can be machined in metals using femtosecond laser, with a special geometry, superior quality, and high reproducibility [13, 25, 26]. Some samples drilled by femtosecond lasers are shown in Figure 2.7. In Figure 2.7 (a), holes were drilled in a 1mm Thick Stainless Steel Plate with 0.9 mJ, 150 fs Laser Pulses at a Wavelength of 780 nm and 1 kHz Repetition Rate. Figure 2.7 (b) shows femtosecond laser micro machining in aluminum, while Figure 2.7 (c) shows holes drilled in steel.

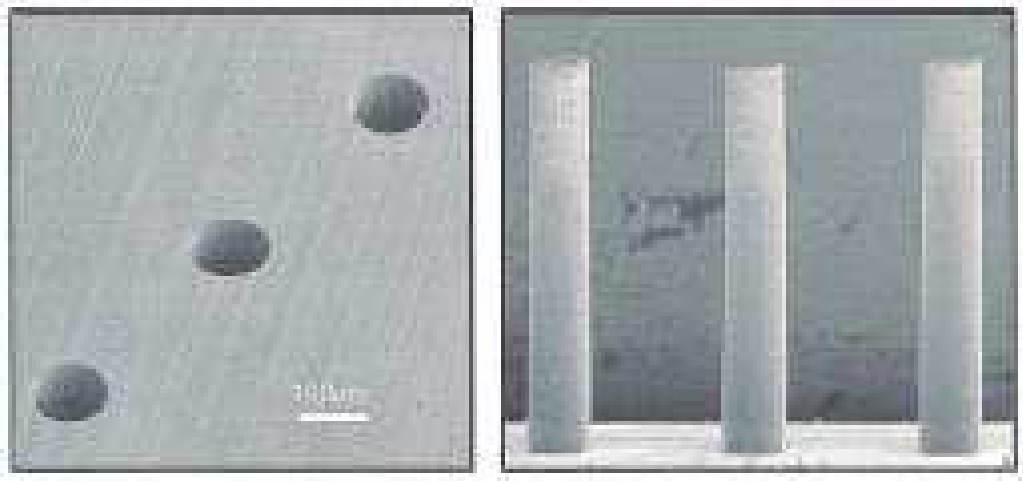

Figure 2.7 (a) Holes drilled in a 1mm Thick Stainless Steel Plate [26]

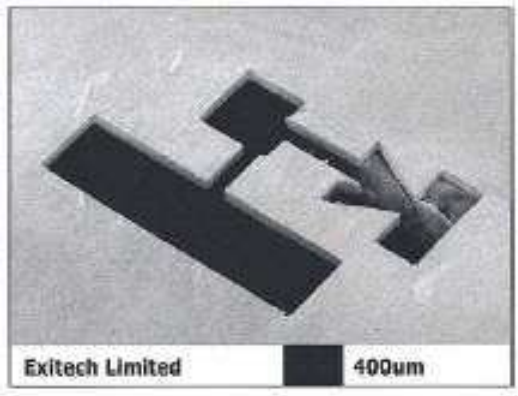

Figure 2.7 (b) Microdrilling of Aluminium [13]

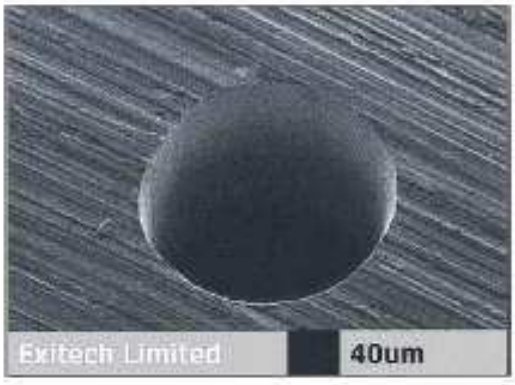

Figure 2.7 (c) Holes Drilled in Steel [13]

Figure 2.7 Femtosecond Laser Microdrilling in Metals

2.2.3.4 Biomedical Application

Laser applications in biomedical field cover many aspects, such as biomaterial thin-films [27-32], medical devices [33-35], laser surgery, etc. Generally speaking, it can be divided into two types: imaging application and therapy application (laser surgery).

In terms of femtosecond application in biomedical imaging, one example is two-photon laser scanning microscopy. Using a femtosecond laser source, the local blood volume in the cortex of the anesthetized mouse can be obtained [36]. Fluorescent dyes were infused in the circulating blood and the blood vessels were imaged. Blood volume was calculated by normalizing the total fluorescence measured at each depth. This method is rapid and only weakly sensitive to background noise; it could be extended to measure the leakiness of the blood vessels. Figure 2.8 shows the images acquired in vitro in left parietal cortex of a Nude mouse.

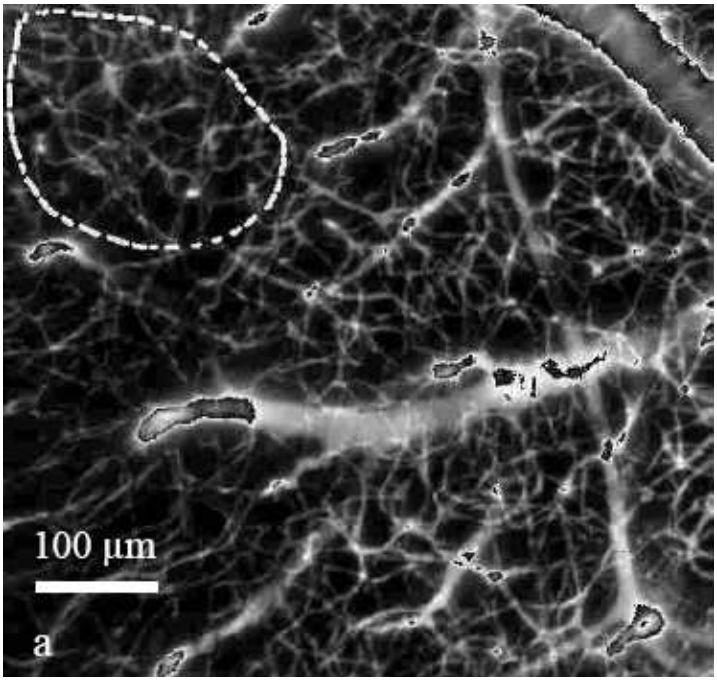

Figure 2.8 (a) Z-projection of the 101 Images of the Stack

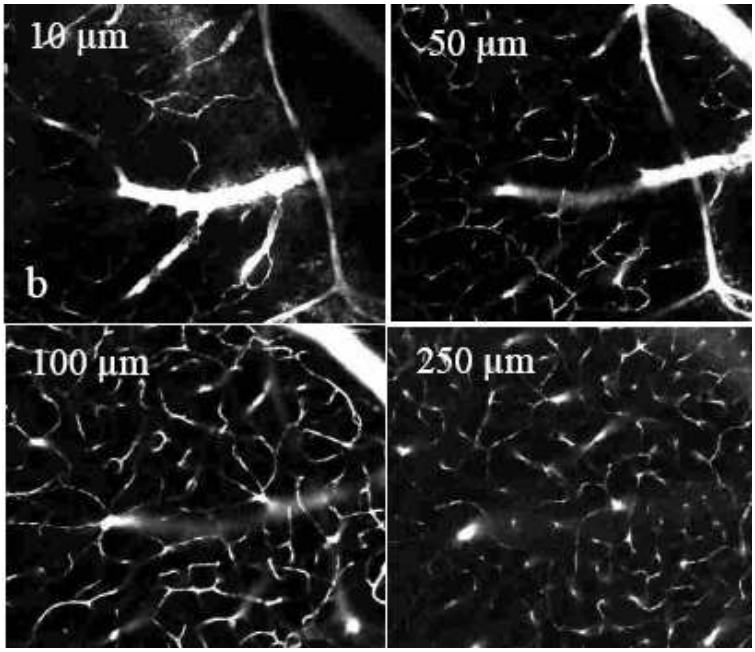

Figure 2.8 (b) Single Images at Different Depths

Figure 2.8 Images Acquired in Vitro from 0 to 300µm in Left Parietal Cortex of a Nude Mouse [36]

As for femtosecond laser surgery, it has been of growing interest since its high precision was demonstrated on a variety of different tissue types. In dentistry for example, femtosecond lasers have demonstrated their practical use to process hard tissue like enamel. Moreover, due to its sub micrometer precision, it is possible to perform surgical procedures inside the human eye. This aspect is demonstrated in details in section 2.4.

2.3 LASER-TISSUE INTERACTION MECHANISMS

In order to effectively select, and predict the result of laser energy that is to be applied to living tissue, a basic understanding of laser tissue interaction is necessary.

The tissue removal effects of laser depend on laser types (wavelength), temporal characteristics (continuous or pulsed), energy delivered (intensity), and tissue properties, etc. Generally speaking, laser tissue interaction mechanisms can be classified to photothermal, photochemical, and photomechanical [37, 38]. Photoablation is also taken as one type of photochemical interaction in this work. Figure 2.9 shows a laser photomedical classification map. In this double-logarithmic map, the ordinate expresses the applied power density in W/cm^2. The abscissa represents the exposure time in seconds. Two diagonals show constant energy fluences at 1 J/cm^2 and 1000 J/cm^2, respectively. According to this chart, the time scale can be roughly divided into five sections: continuous wave or exposure time > 1s for photochemical interactions, 1 s down to 1 μs for thermal interaction, 1 μs down to 1 ns for photoablation, and < 1 ns for plasma-induced ablation and photodisruption. [38]

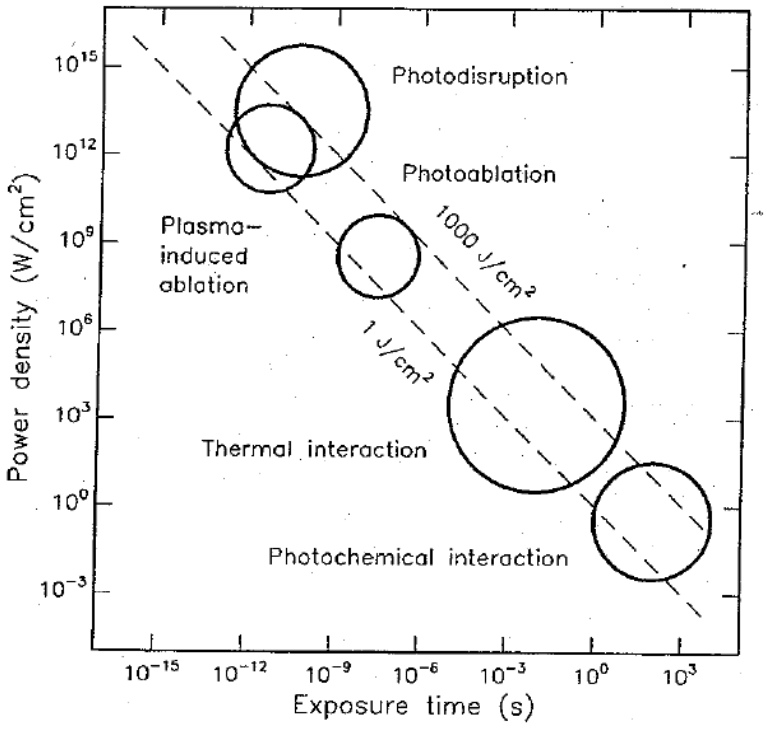

Figure 2.9 Medical Lasers Interaction Map [38]

Recently, the concept of plasma-induced ablation was proposed as one of the laser tissue interaction mechanisms. Therefore, four types of interaction mechanisms are addressed respectively in the following sections.

2.3.1 PHOTOTHERMAL

Photothermal laser-tissue interaction occurs when laser energy is absorbed by the target tissue and converted into heat [39-41]. The effect on the tissue depends on both the magnitude and rate of temperature elevation. Laser energy depositions rapidly heat the tissue above its boiling point, and cause tissue removal by explosive vaporization (photovaporization). Laser wavelength, tissue absorption coefficient, power density, and laser radiation duration determine the photothermal effect. The coincidence of several thermal processes is illustrated in Figure 2.10.

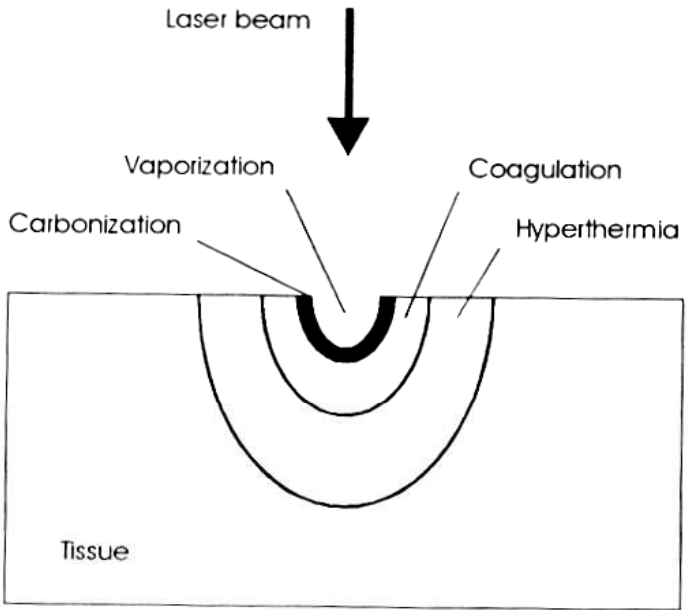

Figure 2.10 Location of Thermal Effects inside Biological Tissue [38]

To minimize unwanted thermal damage to the surrounding ocular tissue, a laser wavelength should be selected that is preferentially absorbed by the target tissue. The laser exposure duration should be shorter than the thermal relaxation time of the tissue, given by:

$$T_h = d_r^2 / 4u \qquad (2\text{-}3\text{-}1)$$

where d_r represents the absorption depth of the radiation, and u is the thermal diffusivity of the tissue.

2.3.2 PHOTOCHEMICAL

Photochemical interaction stems from empirical observations that light can induce chemical effects and reactions within macromolecules or tissues. There are two possible distinguished pathways: photoablative interaction and photoactive interaction.

2.3.2.1 Photoablative Interaction

Photoablative interaction (photoablation) occurs at the molecular level and involves the cleavage of molecular bonds. It occurs in the UV range (193 nm - Excimer laser) [42]. Large numbers of high-energy photons are absorbed in a short time over a short area, thus the treated tissue is reduced to molecular fragments, then ejected from the surface being treated (plume formation). This method can remove one molecular layer at a time, allowing for smooth refractive sculpting.

The photoablative process consists of energy absorption (5-7 eV), photodissociation, and ablation (photofragments, photoejection, desorption). Table 2.1 shows the laser photoablation reaction sequence.

Table 2.1 Photoablation Reaction Sequence

Short UV laser pulse focused on tissue
⇩
Strong absorption in the UV (5-7 eV) by protein amides, peptides
⇩
Promotion to repulsive excited state
⇩
Photodissociation
⇩
Ejection of fragments (no necrosis)

Photoablation can occur in cornea, which has an extremely high absorption coefficient at 193 nm. The photons at 193 nm are highly energetic, possessing more energy than the carbon-carbon bonds interlinking the protein molecules of the cornea. So, 193 nm laser photons can rupture intermolecular bonds resulting in a discrete volume of corneal tissue being removed.

2.3.2.2 Photoactive Interaction

During the photoactive process, molecules are involved as energy carriers or as catalytic regulators. For example, photodynamic therapy (PDT), utilizes a selective laser wavelength to activate a photosensitizing agent, which in turn causes damage or destruction to malignant or abnormal tissue. The sequence of the PDT reaction is listed as shown in Table 2.2.

Table 2.2 PDT Reaction Sequence

Administration and selective retention of photosensitizer by tumor
⇩
Laser or monochromatic light irradiation
⇩
Resonant excitation of photosensitizer
⇩
Simultaneous or sequential decays
⇩
Intramolecular energy transfer & thermal deactivation
⇩
Production of reactive species & hyperthermia
⇩
Cytotoxic action & tumor eradication

2.3.3 PLASMA-INDUCED ABLATION

When obtaining power densities exceeding 10^{11} W/cm^2 in solids and fluids, or 10^{14} W/cm^2 in air, a phenomenon called optical breakdown occurs. By means of plasma-induced ablation, very clean and well-defined removal of tissue without evidence of thermal or mechanical damage can be achieved when appropriate laser parameters are chosen.

Optical breakdown renders possible an energy deposition not only in pigmented tissue but also in nominally weakly absorbing media. This is due to the increased absorption coefficient of the induced plasma. Thereby, the field of potential medical laser applications is considerably widened. Especially in ophthalmology, transparent tissues like cornea and lens become potential targets of laser surgery.

It was observed that either Q-switched pulses in the nanosecond range or mode locked laser pulses in the picosecond or femtosecond range can induce localized microplasma. In Q-switched pulses, the initial process for the generation of free

electrons is supposed to be thermionic emission, i.e. the release of electrons due to thermal ionization. In mode locked pulses, multiphoton ionization may occur due to the high electric field induced by the intense laser pulse.. In general, multi-photon ionization denotes processes in which coherent absorption of several photons provides the energy needed for ionization. Due to the requirement of coherence, multi-photon ionization is achievable only during high peak intensities as in picosecond or femtosecond laser pulses. In addition, in the nanosecond range, because of the associated increase in threshold energy of plasma formation, plasma temperature is usually higher, and thus the optical breakdown is often accompanied by non-ionizing side effects.

2.3.4 PHOTOMECHANICAL

Photomechanical interaction describes the physical effect associated with optical breakdown. When breakdown takes place insides fluids or soft tissues, plasma formation and shock wave generation will occur, and cavitations and jet formation may additionally take place.

The mechanical effects scale linearly with the absorbed energy. At high pulse energies during plasma-induced ablation, mechanical effects become more significant and might even determine the global effect upon the tissue. Cavitation occurs when the laser beam is focused into the subsurface of the tissue. Cavitation bubbles consist of gaseous vapors, mainly water vapor and carbon oxides, which eventually diffuse again into the surrounding tissue.

Because of the mechanical impact, the term photodisruption is widely used for photomechanical interaction. It has become a well-established tool of minimal invasive surgery, such as laser-induced lithotripsy of urinary calculi, posterior capsultomy of the lens, which is frequently necessary after cataract surgery.

During photodisruption, the tissue is split by mechanical forces. Two different mechanisms are responsible for long pulses (thermal) and ultrashort pulses (nonlinear multi-photon absorption). The sequence of photomechanical interaction is shown in Table 2.3.

Table 2.3 Photomechanical Interaction Sequence

Short laser pulse focused at target tissue ns and ps pulses
⇩
High power density>1012 watts/cm2
⇩
High electric field
⇩
Dielectric breakdown (thermal and multiphoton)
⇩
Plasma formation of free electrons
⇩
Spherical shock wave propagating at sound velocity
⇩
Localized mechanical rupture for small radius

2.4 FEMTOSECOND LASER SURGERY

To be a practical alternative, clinical lasers have to be easy to control, safe, and effective in cutting and removing tissue with limited collateral damage. Compared to long pulse lasers and conventional surgery methods, femtosecond lasers provide more efficiency and safety, thus they are of significant interest to clinicians and

researchers [43-45]. The following section shows research work, which has been carried out to study the femtosecond laser potential in surgery.

2.4.1 DENTAL SURGERY

Minimal invasive treatment of carious tissues has become an increasing important aspect in modern dentistry. Figure 2.11 shows two SEM images of holes ablated with femtosecond Ti:Sapphire laser and Q-switched Er:YAG laser. Both were done next to each other in the same sample of dentine, thus the influence of different material properties was avoided. The focus diameters of both laser beams were 80 μm. The pulse energy of femtosecond laser was 400 μJ, and that of nanosecond laser was 1.6 mJ. It can be clearly seen that a precise structuring of teeth with minimal damage to the surrounding tissue is only possible using femtosecond laser, not nanosecond laser.

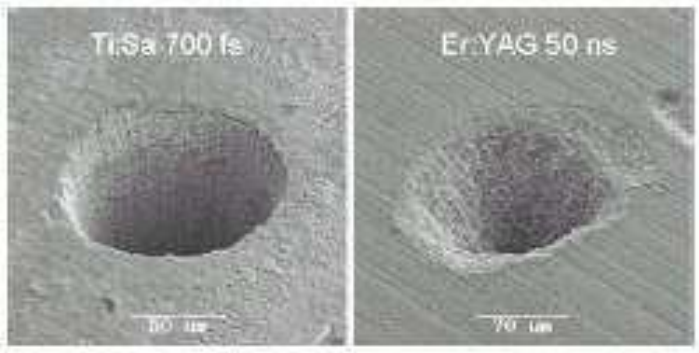

Figure 2.11 Holes Ablated with Femtosecond Ti:Sa Laser (left) and Q-Switched Er:YAG Laser (Right) [46]

Ultra fast pulses could remove bits of tooth without affecting surrounding material (see Figure 2.12). The image of the crater's cut edge in the inset shows the absence of any collateral damage in the surrounding tissue. The scale bar is 50 mm.

Together with the development of femtosecond technology, ultra-fast-laser dentistry is expected to be painless and protect nearby healthy enamel.

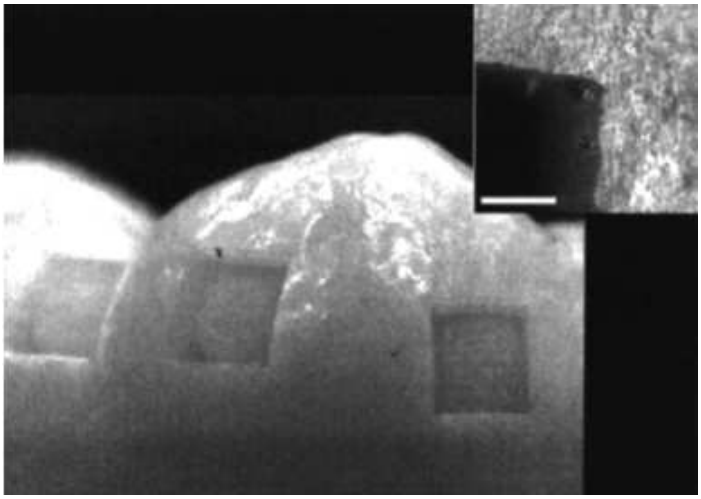

Figure 2.12 Optical Microscope Images of the Craters on the Tooth Surface Ablated with 150 fs Laser Pulses [47]

2.4.2 EAR SURGERY

Due to its high precision, low thermal damage and mechanical stress on bone and inner ear, femtosecond laser pulses are well suited for ear surgery applications. Potential applications are the reconstruction of defect auditory ossicles, perforation of stapes foot plate (stapedioplasty) and modeling of ossicles as an alternative docking methods of active middle ear implants or positioning of cochlea implants.

Figure 2.13 shows the processing of a human malleus with 130 fs laser pulses and a pulse energy of 30 μJ. Analyzing laser-generated cavities in human ossicles, the high precision can be demonstrated. Even at pulse repetition rates of 3 kHz, no thermal effects like melting zones can be found.

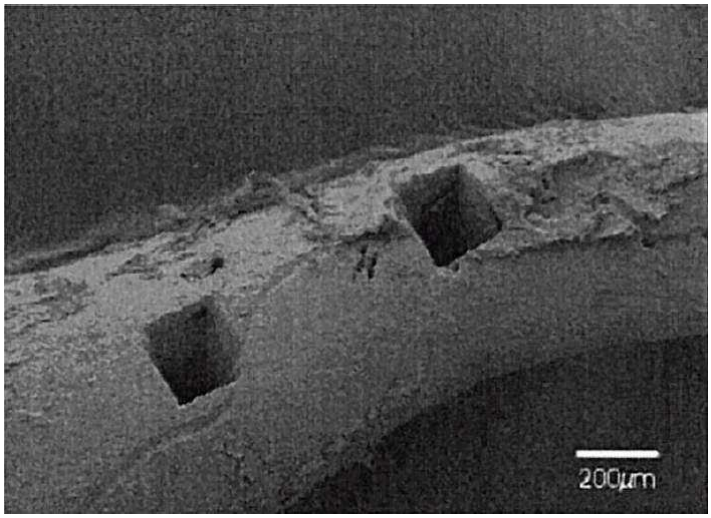

Figure 2.13 Femtosecond Laser Processing of a Human Malleus [43]

2.4.3 EXTRALUMINAL LASER ANGIOPLASTY (ELAN)

The main cause of cardiovascular disease is a process known as atherosclerosis. It decreases the elasticity of the vessel and also encroaches on the internal dimensions of the vessel. The arterial wall becomes thick, and it is caused by the formation of atheroma within the inner layers of the vascular walls. Such a blockage may result in acute myocardial infarction (heart attack) or stroke (brain attack). Traditional treatments include internal surgical procedures (CABG - Coronary Artery Bypass Grafting) and balloon angioplasty.

A recently developed procedure using femtosecond laser technology called Extraluminal Laser Angioplasty (ELAN) is used to remove tissue from the external surface of the artery wall, thus reducing the effective wall thickness and restoring arterial wall flexibility. As soon as flexibility of the arterial wall is restored, the blood pressure inside the artery ensures an increase in vessel diameter and relief of

obstruction (Figure 2.14). This is in comparison to Balloon angioplasty and Stenting methods that force the arterial wall outwards (Figure 2.15).

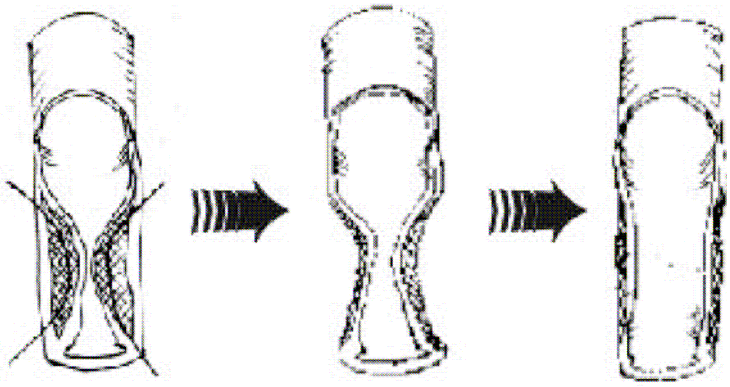

Figure 2.14 Tissue Removal from the External Surface of the Artery Wall using Femtosecond Laser [44]

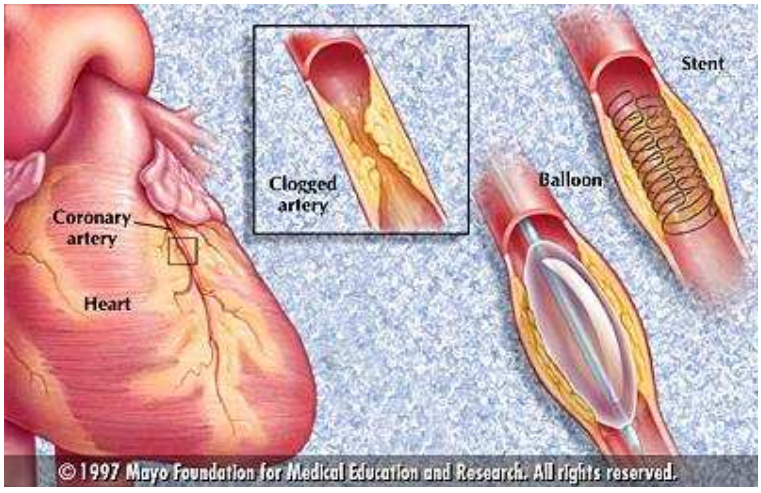

Figure 2.15 Balloon and Stent that Force the Arterial Wall Outwards [48]

2.4.4 OPHTHALMIC APPLICATIONS

2.4.4.1 Basic Ocular Physiology

The human eye structure is shown in Figure 2.16. It is a slightly ovoid organ, and composed of three distinct tunics or layers. The sclera is the tough outer coat of the eye. It is contiguous with the cornea. The middle layer of the eye is composed of a rich network of blood vessels that supplies nutrition to the eye. The posterior segment of the eye is the choroid.

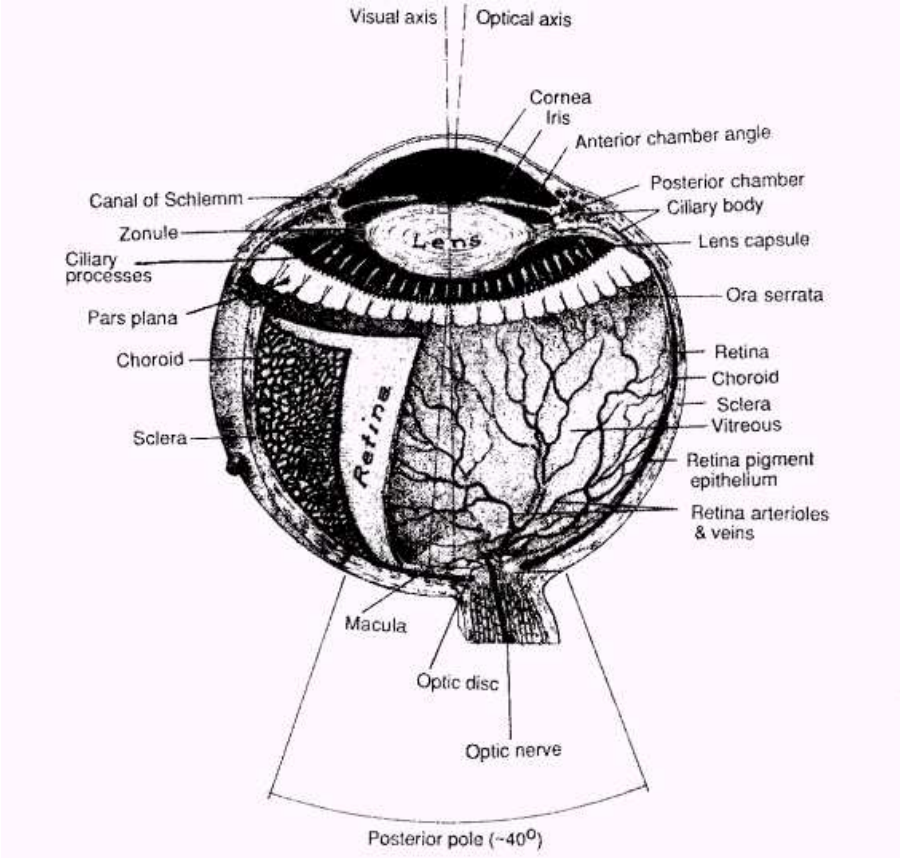

Figure 2.16 Anatomical Drawing of the Eye [49]

An eye is divided into three cavities by intraocular structures. The anterior chamber lies between the cornea and iris. It is filled with a clear water-like fluid, the aqueous humor. Behind the iris and anterior to the lens lies the posterior

chamber. The large cavity posterior to the lens is filled with a transparent jelly-like substance, the vitreous humor.

2.4.4.2 Optical Properties in the Eye

A human eye optical model is shown in Figure 2.17. In the visible and near infrared spectrum (400 nm to 1,400 nm), the absorption characteristics of ocular tissues are determined by a group of chromospheres, hemoglobin, and melanin. In the mid-infrared spectrum (1.8 μm-10.6 μm), the major molecule absorbing incident photons is water. The total transmittance at the various anterior surfaces is given in Figure 2.18.

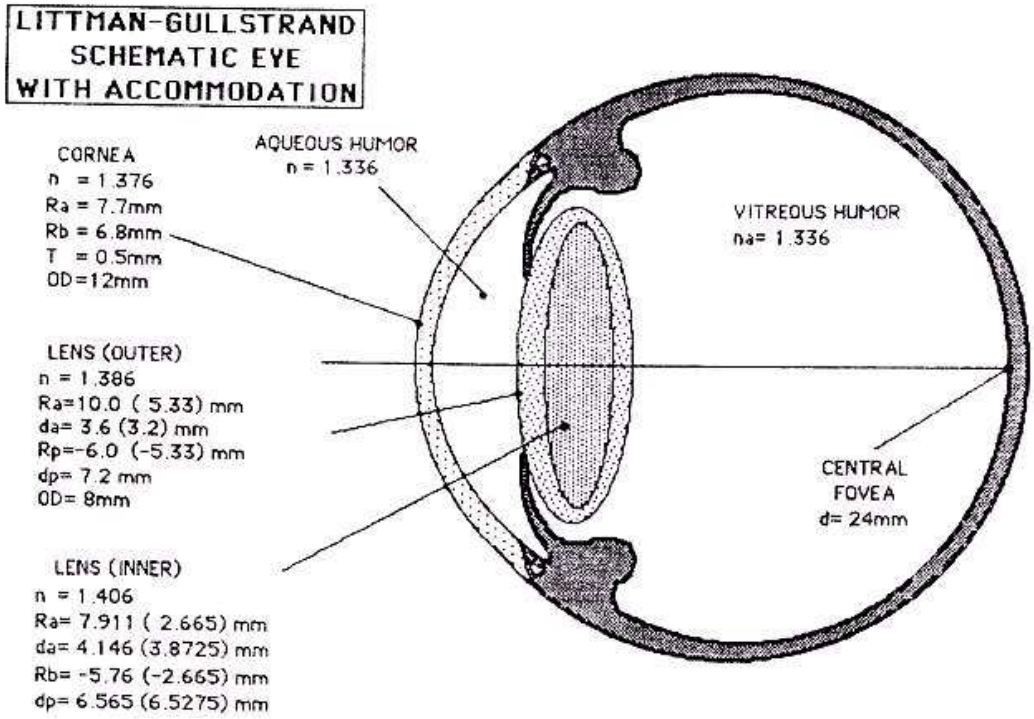

Figure 2.17 Schematic Eye with Accommodation. [49]

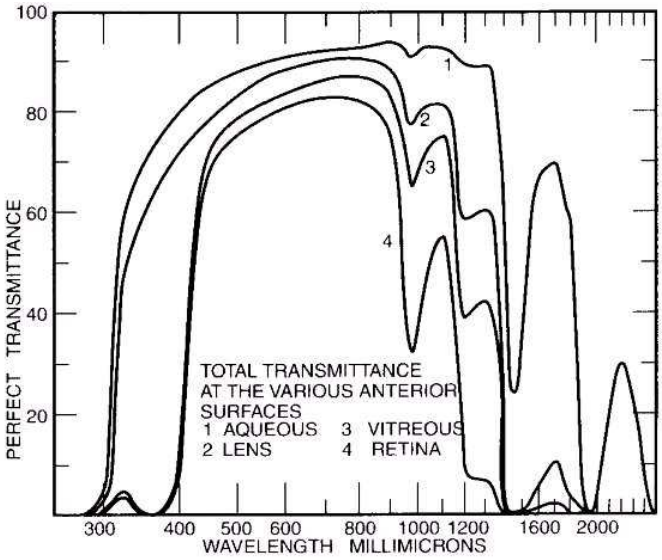

Figure 2.18 Total Transmittance of the Entire Eye [49]

2.4.4.3 FS-LASIK

Currently, excimer laser is used to correct refractive errors in clinic. Laser in situ keratomileusis (LASIK) is one method for refractive surgery [50, 51]. LASIK is usually employed for correcting higher degrees of myopia, and it requires relatively larger laser energy compared to photorefractive keratectomy (PRK). This can lead to unacceptable corneal haze, scarring and visual degradation. Complications may occur with LASIK and result in poor visual outcomes.

Femtosecond laser shows great potential to improve the LASIK surgery effect. It is named FS-LASIK. The beauty of femtosecond laser in LASIK is that surgeons can change the ablation program to alter flap diameter, flap thickness, hinge location, and hinge width. The borders of the flap are more vertically oriented compared to those created by mechanical keratomes, thereby making them more resistant to flap slippage and possibly epithelial ingrowths. In addition, as

femtosecond laser is a solid-state laser, it is more reliable and maintenance-free compared with the excimer laser.

The principle of the FS-LASIK procedure is shown in Fig. 2.19. By scanning the laser in a spiral pattern, a lamellar intrastromal cut is performed in the first step. In the second step, another cut prepares a stromal lenticule with the desired shape. In the third step, the anterior corneal flap is opened, and the prepared lenticule can be extracted. Finally, the flap will be repositioned on the cornea. The surface of the cornea follows the missing volume of the lenticule, thereby leading to a change in refractive power.

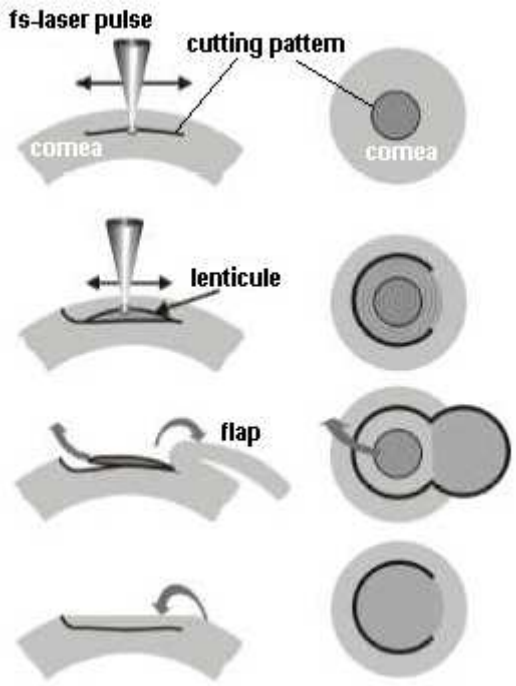

Figure 2.19 FS-LASIK Procedure [43]

Another important application of femtosecond lasers in ophthalmology is glaucoma treatment, which is our interest in this research, and is discussed in detail in the following sections.

2.5 GLAUCOMA

2.5.1 WHAT IS GLAUCOMA

Glaucoma is a major cause of world blindness in developing and developed nations. The World Health Organization Global data on blindness show that over half of the blind due to glaucoma reside in Asia, the majority being Chinese [8]. In Singapore, 40% of blindness is because of glaucoma. In the United States, glaucoma is the second leading cause of existing as well as new cases of irreversible blindness.

Basically, glaucoma results from the intraocular pressure. A normal intraocular pressure is about 13±3 mm Hg above ambient pressure [38]. It is created by aqueous humor, and produced by the ciliary body. The aqueous humor flows anteriorly to drain through the trabecular meshwork. The trabecular meshwork is a filtration structure, and is located in the angle between the cornea and iris. The flow sequence is shown in Figure 2.20. Abnormalities of the pressure regulating system in the eye can result in abnormally high intraocular pressure ($\geq$22 mm Hg), as represented in Figure 2.21, thus results in glaucoma [52]. It damages the delicate nerve fibers in the optic nerve, causing a loss of vision.

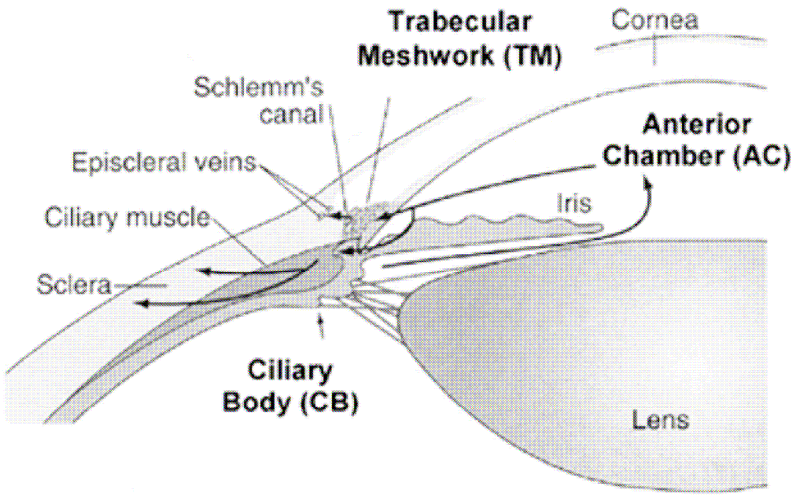

Figure 2.20 Intraocular Aqueous Humor Flow Sequence [52]

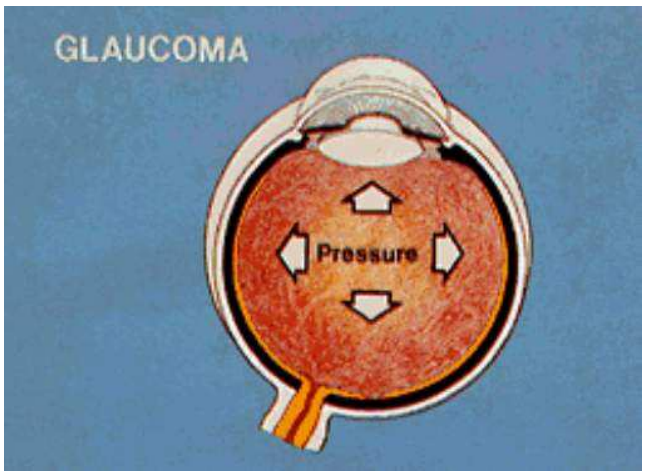

Figure 2.21 Intraocular Pressure Increase [53]

Generally speaking, there are two main types of glaucoma, open angle glaucoma and closed angle glaucoma. The difference of aqueous flow between normal eye and the eye with glaucoma is shown in Figure 2.22.

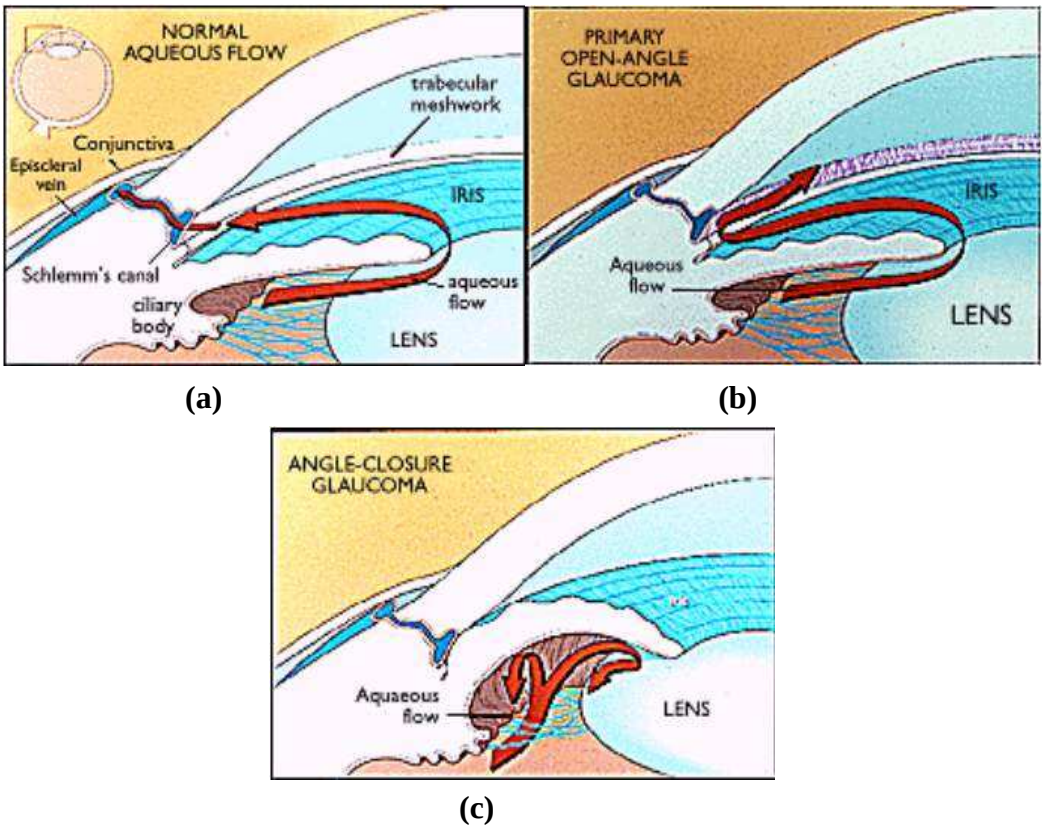

Figure 2.22 Aqueous Flow in (a) Normal Eye (b) the Eye with Open Angle Glaucoma and (c) the Eye with Closed Angle Glaucoma [53]

The corresponding mechanisms causing glaucoma are addressed in the following sections.

2.5.1.1 Open Angle Glaucoma

It is the most common glaucoma. The drainage angle of the eye can become less efficient with age, and pressure within the eye gradually increases. If this increased pressure results in optic nerve damage, it is known as chronic open-angle glaucoma (see Figure 2.22 (b)). Chronic open-angle glaucoma can damage vision gradually and painlessly. This disease is difficult to be noticed until the optic nerve is already badly damaged.

2.5.1.2 Closed Angle Glaucoma

It results when the drainage angle of the eye becomes completely blocked (see Figure 2.22 (c)). It is as though a sheet of paper floating near a drain, suddenly drops over the opening, and blocks the flow out from the sink. In the eye, the iris may act like the sheet of paper closing off the drainage angle. This results in a dangerously high eye pressure, associated with pain, redness, low vision, and nausea.

Not all the types of glaucoma are characterized by high intraocular pressure. Mechanical compression and/or decreased blood flow of the optic nerve associated with other factors can also lead to glaucoma. These are not in the range of our concern, so will not be discussed any further.

2.5.2 HOW TO DETECT GLAUCOMA

To determine the risk for developing the disease, many kinds of information need to be put together [54]. The most important risk factors include age, nearsightedness, family history of glaucoma, past injuries to the eyes, or a history of severe anemia or shock. All these factors will be weighed to decide if treatment for glaucoma is needed. Generally speaking, four tests would be done during glaucoma detection: visual acuity, visual field, pupil dilation, and tonometry.

2.5.3 HOW TO TREAT GLAUCOMA

The treatment for glaucoma is aimed at reducing the level of intraocular pressure. As a rule, glaucoma cannot be cured, but it can be controlled. Glaucoma treatment depends upon the nature and severity of each case [55]. Eye drops or pills are often used to treat glaucoma first, as they seem to be the least traumatic. However, they may not always be the best treatment. Depending on the individual, eye medication can have very significant side effects on the body as well as the eye. Therefore, if medication cannot work for the individual, surgery will then have to be performed. Surgical treatment includes conventional surgery and laser surgery. They are discussed respectively in the following sections.

2.6 GLAUCOMA SURGERY

2.6.1 CONVENTIONAL SURGERY

Filtering surgery is the most common conventional surgery in glaucoma treatment. The purpose of surgery is to make a new opening for the fluid to leave the eye.

Glaucoma filtering surgery is performed in a hospital or an outpatient surgery center, with local anesthesia, and gentle sedation. A surgeon uses very delicate instruments to remove a tiny piece of the wall of the eye (the sclera), as shown in Figure 2.23, leaving a tiny opening. The aqueous fluid can then drain through this opening, thereby reducing the intraocular pressure. The fluid is reabsorbed into the bloodstream. Surgery does not leave an open hole in the eye. The hole is covered by the conjunctiva.

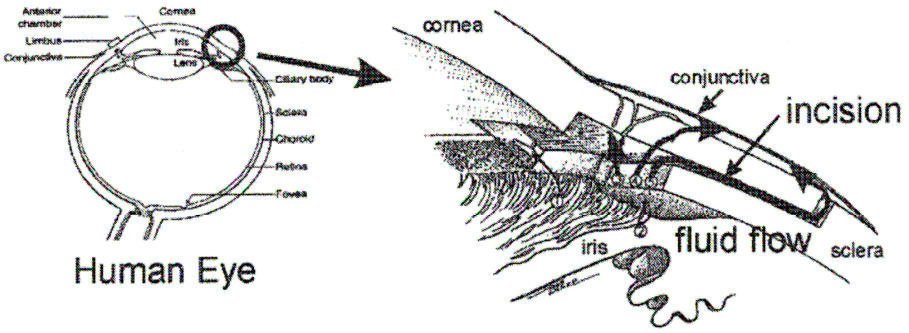

Figure 2.23 Filtering Surgery Procedure [10]

In some patients, the surgeon may place a small plastic tube or valve in the eye through a tiny incision in the sclera. The valve acts a regulator for the buildup of aqueous fluid within the eye. When the intraocular pressure reaches a certain level, the valve opens, allowing the fluid to flow out of the eye's interior, where the body can reabsorb it.

Like any operation, glaucoma surgery can cause side effects. These include cataract, problems with the cornea, inflammation or infection inside the eye, and swelling of blood vessels behind the eye.

2.6.2 LASER SURGERY

As mentioned before, although medication and traditional surgery have their respective application regions, both also experience limitations. Laser surgery has given ophthalmologists new and remarkably safe ways to control ophthalmic diseases. It is a quick and convenient procedure that can be performed on an outpatient basis. As compared to conventional surgery, there are some obvious

advantages with laser therapy such as no infection, and vision usually recovers within minutes of treatment [10].

The most common laser surgical techniques consist of laser trabeculoplasty, laser iridotomy and laser photocoagulation. They are described below in the following section.

2.6.2.1 Laser Trabeculoplasty

Argon Laser Trabeculoplasty (ALT) is used to treat glaucoma currently. Figure 2.24 shows the ALT process. During argon laser trabeculoplasty, a special mirrored contact lens is applied to the patient's cornea. This device allows direct observation of the angle of the anterior chamber of the eye. The aiming beam of the argon laser then is directed at the trabecular meshwork.

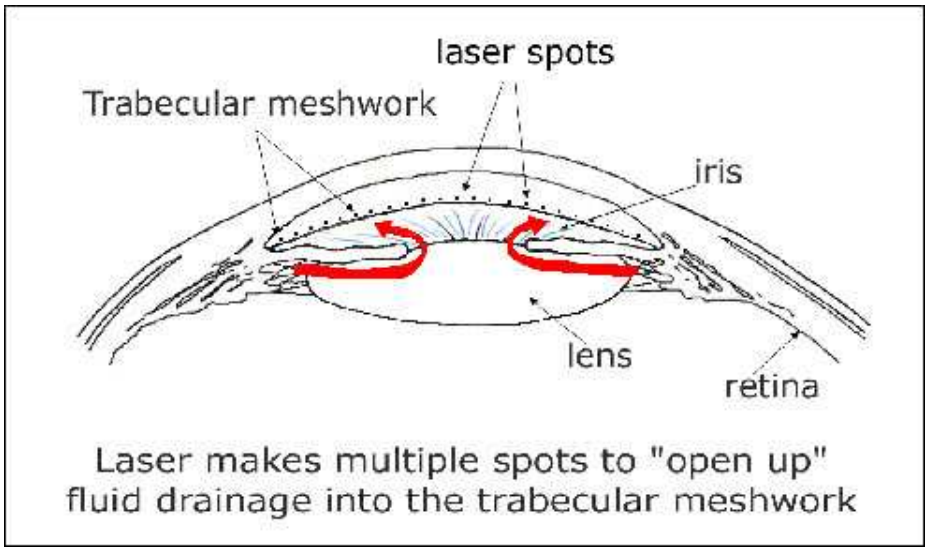

Figure 2.24 Argon Laser Trabeculoplasty Procedure [56]

Although Argon Laser Trabeculoplasty is proven to provide excellent pressure-lowering effects, its application is limited by the underlying coagulative damage

and subsequent scarring to the trabecular meshwork. Scarring of the trabecular meshwork caused by the thermal effect of ALT is its primary disadvantage and limitation.

Selective laser trabeculoplasty (SLT) is a new method for laser trabeculoplasty. It uses a combination of frequencies. Laser source is Q-switched, frequency doubled Nd:YAG. This method offers the proven advantages of ALT. It is based on selective photothermolysis confining thermally mediated damage to chosen pigmented targets, so no collateral tissue damage occurs. However, for some kind of people with light color iris, this method may not work.

2.6.2.2 Laser Iridotomy

A forwardly bowed iris may obstruct the aqueous fluid channel. This condition may predispose one to an acute episode of closed angle glaucoma. If the angles are never acutely closed, but glaucoma is still present, the patient is diagnosed with narrow angle glaucoma. Laser peripheral iridotomy is performed for closed glaucoma or narrow angle glaucoma.

Laser iridotomy involves creating a tiny opening in the iris, allowing aqueous fluid to flow from behind the iris to the anterior chamber of the eye, as shown in Figure 2.25. This typically results in resolution of the forwardly bowed iris and thereby an opening up of the angle of the eye. The narrow or closed angle thus becomes an open angle. During laser iridotomy, a special contact lens is applied to the patient's cornea, which helps to focus the laser, allowing the creation of an opening.

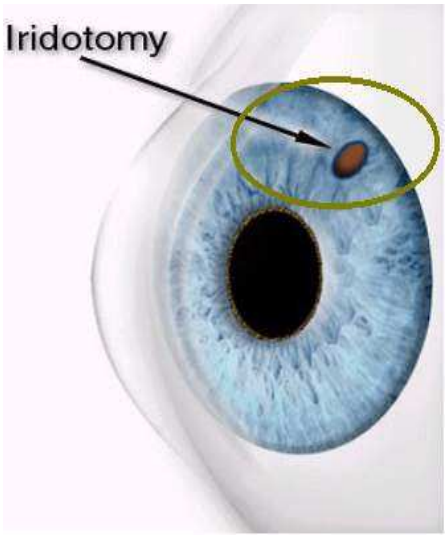

Figure 2.25 Laser Iridotomy Procedure [57]

The iris is often found in close proximity to the easily damaged corneal endothelium, or the undersurface of the cornea. Inappropriate use of the surgical laser can result in permanent damage to the cornea as well as to the lens of the eye and to an intraocular lens.

Iridotomy using nanosecond lasers is performed with mJ pulse energies, and often cause defect of the pigment epithelium surrounding the small iris defect; fibrin exudation often leads to a re-closure of the defect at a later time [58, 59]. For example, Nd:YAG laser with 3-10 ns was used as one laser source to produce a plasma for laser iridotomy. The plasma results in evaporation at the aiming site. At the same time, plasma expansion can cause emission of shock waves and formation of cavitation bubbles, therefore causing collateral damage. When optical breakdown threshold decreases, the disruptive effects can be reduced [60-62]. Some investigation has been carried out to study the surgery effect at different pulse durations. Using picosecond lasers, a more clearly defined iris canal can be created and surrounding pigment epithelium remains intact. However, some limitations exist, such as cellular debris dispersion, iris bleeding into the anterior

chamber and its accumulation in the inferior chamber angle. All these destructive effects may reduce the trabecular outflow facility and cause the intraocular pressure (IOP) to increase. Table 2.4 shows the comparison of nanosecond laser and picosecond laser iridotomy. From Table 2.4, it is shown that although the single pulse energy value was reduced in the picosecond region, more frequent minor intraoperative iris bleeding was observed following picosecond iridotomies (64%) than after nanosecond iridotomies (50%) [63]. The increasing of IOP is significant.

Table 2.4 Laser Iridotomy from Nanosecond to Picosecond Range [63]

Iridotomy / iridectomy	Nd:YAG ns laser	Nd:YLF ps laser			
		All Iridectomies	500mm	600mm	750mm
Number of cases	20	53	9	18	19
Single pulse energy (mJ)	7.9 (6.6-12.0)	0.25	0.25	0.25	0.25
Total energy (mJ)	52 (20 – 122)	4028 (316– 15 400)	1667 (316-4887)	5166 (544-10975)	4087 (468-9682)
Complications:					
Iris bleeding	10 (50%)	32 (64%)	4 (44%)	14 (75%)	14 (74%)
Increase in IOP>10mm Hg	1 (5%)	11 (22%)	0 (0%)	1 (6%)	8 (42%)
Increase in IOP>20mmHg	0 (0%)	6 (11%)	0 (0%)	0 (0%)	4 (21%)
Mean mm Hg increase in IOP	6 (0 – 21)	9 (0-29)	3 (0-6)	5 (1-14)	16 (1-29)
Exudation of fibrin	2 (10%)	1 (2%)	0 (0%)	0 (0%)	1 (5%)
Corneal lesion	1 (5%)	7 (13%)	0 (0%)	4 (22%)	3 (14%)
Repeat treatment necessary	5 (25%)	6 (11%)	2 (11%)	2 (11)	3 (14%)

2.6.2.3 Laser Cyclophotocoagulation

Nd:YAG thermal laser surgical cyclophotocoagulation (CPC) can be utilized when other surgical modalities have failed to halt the advancement of glaucoma. Surgical laser energy is applied through the sclera, or the outer layer of the eye, to the

ciliary body, as shown in Figure 2.26. The ciliary body produces aqueous fluid, which maintains the intraocular pressure. The selective destruction of the ciliary process reduces aqueous production and lowers intraocular pressure.

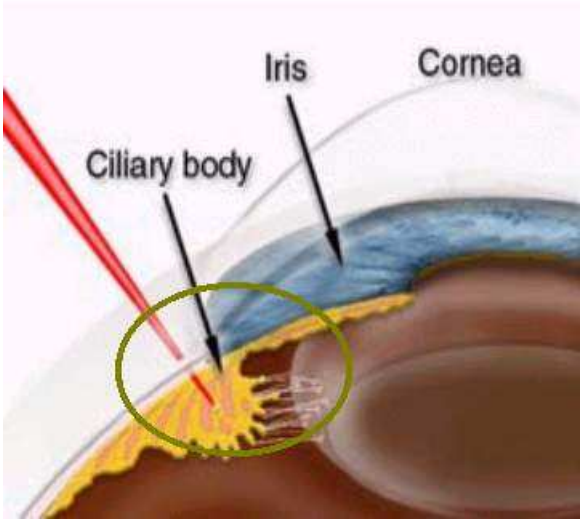

Figure 2.26 Laser Cyclophotocoagulation Procedure [57]

This procedure is considered as a last resort, as considerable inflammation can occur, it is associated with some discomfort, and it includes some risks. For example, the eye may lose critical circulation, or it may sustain too much damage to the ciliary body and not be able to make fluid at all. If this occurs it will cause the eye to involute, or shrink, resulting in a total loss of vision.

To sum up, current long pulse laser surgery is able to lower the pressure in glaucoma treatment, but there are still some problems existing as mentioned previously. In addition, in all of the present clinical laser surgery methods, the effects wear off over time. Two years after laser surgery, the pressure increases again in more than half of all patients.

2.7 FEMTOSECOND LASER POTENTIAL IN GLAUCOMA TREATMENT

Femtosecond laser shows unique advantages in glaucoma treatment [10, 11]. In-vitro experiment studies have being carried out by some researchers.

Photodisruption in translucent sclera using femtosecond pulses has been studied for glaucoma treatment [9]. In-vitro experiment results show that if the sclera's natural scattering properties are reduced by dehydration, then surgery is possible. Recently, the feasibility of using 800 nm femtosecond Ti:Sapphire laser for trabecular meshwork (TM) has been studied through in-vitro experiment. A variety of pulse energies and exposure times were used to create lesions in the TM with minimal collateral damage [64]. These results show a promising future for femtosecond laser in glaucoma treatment.

The main advantages of femtosecond pulses to perform eye surgery are addressed below.

2.7.1 NONLINEAR ABLATION PROCESS

Ablation with long pulse lasers is mainly a linear (i.e single photon) process. The penetration depth is determined by the absorption coefficient at the laser wavelength. Most of the advantages of tissue ablation with the femtosecond laser stem from its unique excitation mechanism. It relies on a nonlinear (i.e. multi-photon) mechanism. Several photons must be absorbed to overcome the water bandgap, and an additional few photons are required to initiate an electron

avalanche. This avalanche leads to optical breakdown, and the resulting plasma mediates the ablation process. Because a high intensity is required to absorb so many photons, the breakdown is confined to a small volume near the focal point [64, 65].

2.7.2 DETERMINISTIC

With longer pulses, the seed for the avalanche process exist as free carriers in the tissue. Since the equilibrium free carrier concentration fluctuates, the ablation process for longer pulses is not deterministic. For short pulses, laser-induced breakdown in biological tissue is "deterministic" [66], and therefore, it is repeatable and reproducible, since the electromagnetic fields are high enough to generate free carriers without relying on intrinsic carriers in the target tissue.

2.7.3 LOW PULSE ENERGY NEEDED

Only a small amount of the incident energy is absorbed to create the plasma. The plasma is a very hot electron-ion gas at a high pressure. It cools either by expanding, heating the surrounding material, or by emitting light. Most of the absorbed energy goes into expansion. The initial high pressure in the plasma causes a shock wave to form and propagate. At slower time scales, the hot plasma vaporized some volume of material creating a micro-bubble. The bubble expands, compressing the surrounding material, oscillates through a few cycles, finally collapses.

2.7.4 LITTLE COLLATERAL DAMAGE

A certain amount of energy is needed in the pulse to cause damage. If the energy is lower than this "threshold", the material will not be damaged [67,68]. A curve of threshold energy vs. pulse width on cornea is shown in Figure 2.27. The reduced threshold fluences for plasma-mediated ablation at shorter pulse durations were measured. Two aspects can be seen from Figure 2.27, when the pulse becomes shorter, the energy threshold decreases; the uncertainty in the threshold indicated by the error bars also decreases.

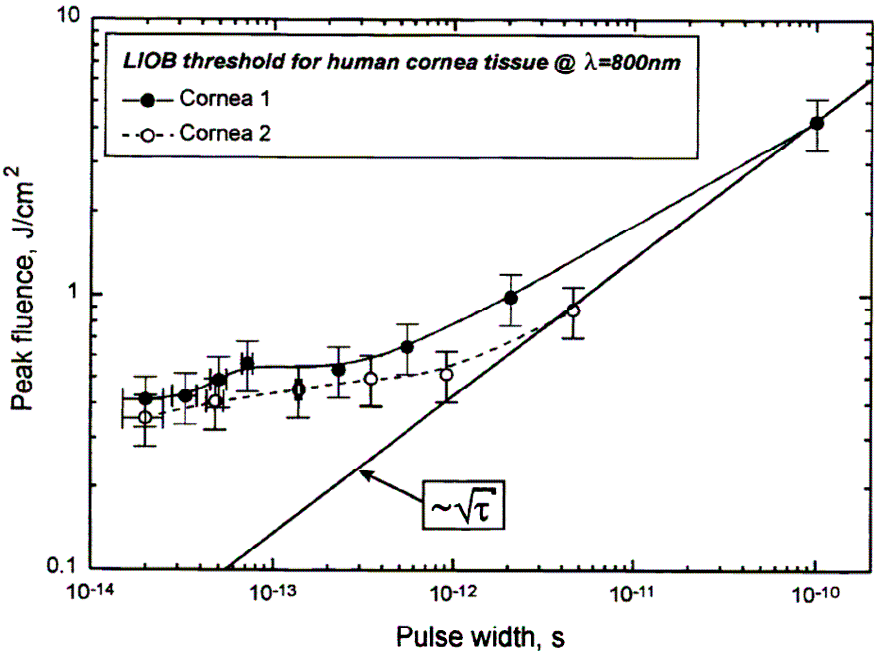

Figure 2.27 A Curve of Threshold Energy versus Pulse Width in Water [69]

Therefore, by using femtosecond lasers, a very clean tissue ablation may be produced with minimum side effects at very small pulse energies [70].

Meanwhile, laser surgery is a complex sequence of processes. It benefits from a thorough understanding of the mechanism of interaction between the laser and the tissue. The goal is to maximize the efficiency as well as minimizing the effects of

thermal damage. Although some in-vitro experiment work such as those mentioned above have been carried out, femtosecond laser application in glaucoma treatment has not been successful; in other words, it is still far from the clinic application. In addition, the theoretical studies on the interaction mechanism are quite few, and the interaction mechanism is still not fully understood. To overcome these limitations, in our research, the interaction mechanism during femtosecond ocular tissue interaction will be theoretically studied. Using both a femtosecond amplifier system and a femtosecond oscillator system, in-vitro experiments on fresh porcine ocular tissues will be performed. This research will focus on femtosecond laser application in iridotomy and photocoagulation.

2.8 SUMMARY

Femtosecond technology with its ultra short light pulses forms an innovative laser technology, which can be used for multiple technical applications, and offers completely new possibilities for minimal invasive materials processing. In the industrial fields, including microphotonics and telecommunication, microelectronics, micro fabrication, etc, many promising results have been demonstrated for micromachining with femtosecond lasers. In the biomedical field, femtosecond lasers have also found good use. They have represented superior tissue interaction characteristics compared with conventional surgical techniques or longer pulse laser systems. By producing a micro-plasma through a nonlinear absorption process, they are able to ablate hard or soft tissues very effectively, such as dental surgery, heart surgery, ophthalmic surgery etc.

Femtosecond laser pulses have been evaluated for the use in novel refractive methods in cornea surgery. Researchers are now exploring the possibility of extending this technique to other eye procedures. One of the potential applications is femtosecond laser glaucoma surgery, which is our interest in this research.

Though the current laser glaucoma surgery can be an alternative to conventional surgery, it is accompanied with some problems, such as underlying coagulative damage, hyphema and corneal burns. These existing risks limit the application of lasers in glaucoma treatment.

Due to extremely precise ablation and very low side effects, femtosecond laser makes the future of laser technology in glaucoma treatment look very bright. At the same time, although much work has been carried out, femtosecond laser has not been successful in clinic use yet. The interaction mechanism between femtosecond laser and biological tissue is not the same as that with long pulse laser, and it is more sophisticated and not yet very clear. Classical theoretical model cannot agree with experimental result very well, and it needs to be investigated deeply.

According to the above statement, a full understanding of the femtosecond laser-ocular tissue interaction process is necessary. So in this research, the study on femtosecond laser-ocular tissue interaction mechanism will be carried out, specifically focusing on energy deposition and thermal damage in ocular tissue by femtosecond laser induced optical breakdown. In-vitro experimental study on femtosecond laser processing in ocular tissue was performed. The work carried out in this research is of significance for femtosecond laser application in glaucoma treatment.

CHAPTER THREE

FEMTOSECOND LASER-OCULAR TISSUE INTERACTION ANALYSIS FOR LASER IRIDOTOMY

3.1 INTRODUCTION

Laser iridotomy is one of the main types of the laser surgery methods for glaucoma treatment in clinic. In this procedure, a canal less than 200 micrometer diameter is provided in the iris. The limitation of current laser iridotomy surgery has been addressed in the literature review. In this chapter, to improve its clinical efficiency, the feasibility of the femtosecond laser is theoretically studied. Laser induced optical theory will be addressed and the moving breakdown model from nanosecond region to the femtosecond region will be introduced and discussed. The femtosecond moving breakdown model will be used to predict the optical breakdown threshold; and the Heat Affected Zone model used to analyze temperature increases in water, cornea, aqueous, and iris.

3.2 LASER-INDUCED OPTICAL BREAKDOWN

As mentioned in Chapter 2, during laser-tissue interaction, there are four main classes: photothermal, photochemical, plasma-induced ablation, and photomechanical. The criterion used to distinguish the mechanisms is the energy transmission form in the molecule of the material, which is described as follows.

Laser light is a form of energy. When the pulse interacts with materials, the laser energy will be absorbed via several mechanisms by the material, which is composed of molecules. In general, a molecule stores energy by three mechanisms: rotation, vibration, and electron, as shown in Figure 3.1. In Figure 3.1, the solid points and hollow circles represent the electrons and associated nucleuses, respectively. Different storage mechanisms will associate with different energy levels. Molecule rotation occurs with a typical energy increment of ~0.01 eV, while molecular vibration occurs with an energy difference on the order of ~0.1 eV. Considerable more energy is required (roughly ~1 eV) for energy transfer via electron transition. .

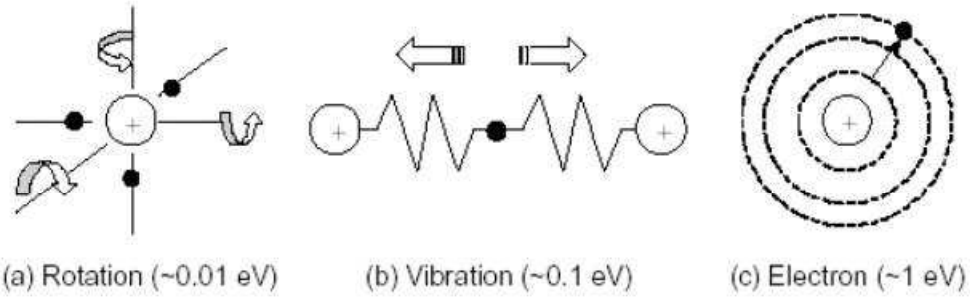

Figure 3.1 Electron States in a Molecule [71]

The transition between different energy levels is demonstrated in Figure 3.2. Thick solid lines, thin solid lines, and dash lines represent electronic states, vibration states and rotational states, respectively.

The electrons usually occupy the ground state at room temperature, where the energy is the lowest and thus the state is most stable. When a low-power radiation is incident upon a dielectric medium at room temperature, only the rotational and vibrational transitions can be induced by absorbing this electromagnetic radiation. Most of the electrons will still occupy the ground state. This leads to a slight temperature rise. The absorption mechanisms and the corresponding heating processes are independent on the intensity of incident radiation.

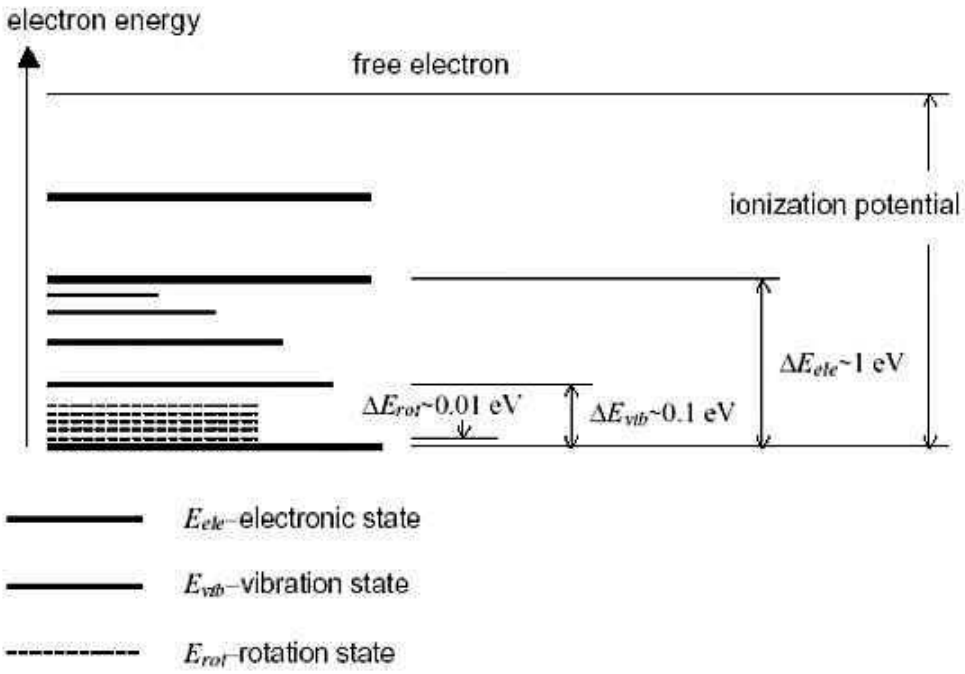

Figure 3.2 Energy Levels of an Electron [71]

However, as incident radiation becomes intensive, a molecule can absorb a sufficient amount of energy. Then one or more electrons are completely removed from the molecule. Such a molecule is ionized via a bound-free transition. Free electron energy absorption is the basis for laser material processing. It is a non-linear phenomenon and named ionization [72].

An ionization process during a laser-material process is defined as laser-induced breakdown (optical breakdown) [73]. During the optical breakdown process, sufficient energy is required to be deposited into the material. It is a complex sequence of processes, leading to the optical behavior changes of the tissue, plasma formation and heating, or even permanent damage in solid dielectrics.

Biological tissues normally exhibit minimal absorption at low laser intensities. Optical breakdown occurs during high intensity laser material interactions. A minimum threshold intensity (I_{th}) is required before breakdown occurs: for the laser intensity at the point of interest $I < I_{th}$, nothing happens, while $I > I_{th}$ results in breakdown.

Two distinct mechanisms are responsible for the optical breakdown process. They are avalanche ionization and multiphoton absorption [74].

Avalanche ionization is initiated when free electrons present in the material absorb the laser energy through inverse bremsstrahlung absorption. During inverse bremsstrahlung absorption, seed electrons absorb laser photons by favorable collisions with heavier particles, i.e., molecules and ions. If they sustain enough favorable collisions, they will eventually gain sufficient energy to impact ionize other molecules, freeing new electrons to repeat the process, thus result in a geometric increase in the free electron density.

Multiphoton absorption occurs when a molecule simultaneously absorbs enough photons to ionize the molecule, and when the incoming laser irradiance exceeds threshold intensity.

3.3 CLASSICAL MOVING BREAKDOWN MODEL

There are four main models existing to explain laser-induced optical breakdown. They are the model of laser-supported detonation waves; the model of traveling ionization waves; the model of radiation transport waves; the moving breakdown model. [73]

The laser-supported detonation model was first proposed by Ramsden and Savic [75]. It assumes that a plasma is first created at the focal plane, due to the high irradiance. As a consequence, a spherical shock wave propagates from that region, causing the laser light to be preferentially absorbed as soon as it reaches the expanding shock-wave front. This mode is not valid to explain the experimental observations of the laser-induced breakdown in water using single picosecond pulses in ocular models, which show that long, single plasmas occur dependence on irradiance similar to, and even more marked than that of nanosecond pulses.

The model of traveling ionization wave assumes that electrons are produced ahead of the breakdown wave. These electrons are responsible for the initiation of the spark at that location, at a subsequent time [76, 77]. This model has proven to be the most adequate to describe the shapes of the observed streaks in gases. In this model, it is assumed that electrons are spread out from the plasma volume to create precursors for plasma formation farther away from the focal plane. This assumption does not find great support in the case of liquids [73].

The model of radiation transport wave assumes that local heating occurs in front of the breakdown region, favoring the emission of ionizing radiation from the gas, that interacts with the laser pulse establishing a new breakdown region [78]. The

experimental findings also do not support this model for liquids. The key evidence is given by the similar plasma elongation with impurity-free and impurity-rich media. According to the model of radiation transport wave, the absorption of laser light at the level of impurities would favor the emission of radiation. This would result in large differences of the overall plasma length for impurity-rich media, contrary to the actual observations.

The model of moving breakdown in its first formulation by Raizer assumes that the breakdown occurs independently at each location on the axis provided that, at that location, the irradiance of the laser beam equals the threshold value required for breakdown. The starting instant of the plasma coincides with the time when the irradiance requirements for breakdown are matched to the threshold of the medium. [78] This model did not prove to be favorable for gases [73], since it was not able to adequately describe the observed time and space dynamics of the laser-induced plasma. However, it is valid to describe the observations in liquids. The intrinsically statistical nature of breakdown and the dynamics of the processes justify the assumption that plasmas may build up independently at each axial location along the beam waist.

Among the four models, the moving breakdown model has obvious advantages to describe the observations in liquids and solids due to its realistic formulation. So moving breakdown was used in this research to analyze the laser-induced breakdown mechanism in ocular tissue.

The classical moving breakdown model has been used to analyze long pulse laser-induced breakdown [79]. It includes the following assumptions for simplicity: (1)

Breakdown occurs independently at each location. (2) The time required for breakdown to occur is negligible. (3) The breakdown threshold is independent of the beam diameter. (4) The threshold is constant in time; i.e., plasma formed early during the laser pulse arrival does not influence the breakdown threshold at other points in the medium.

A Gaussian laser pulse is assumed in the study. The pulse power is expressed as [67]:

$$P(t) = P_{\max} \times \left\{ \exp\left[(-4\ln 2)\left(t / \tau_p \right)^2 \right] \right\} \tag{3-3-1}$$

where $P_{\max}$ is the maximum pulse power, τ_p is the full width at half-maximum pulse duration, and t is time.

The relationship of the beam waist $\omega(z)$ and the focal region z_R is shown in Figure 3.3. They can be expressed as below:

$$w(z) = w_0 \left(1 + \frac{z^2}{z_R^{\,2}} \right)^{1/2} \tag{3-3-2}$$

$$z_R = n \cdot \pi \cdot w_0^2 / \lambda_0 \tag{3-3-3}$$

where λ_0 is the laser wavelength in free space, and n is the refractive index of the medium.

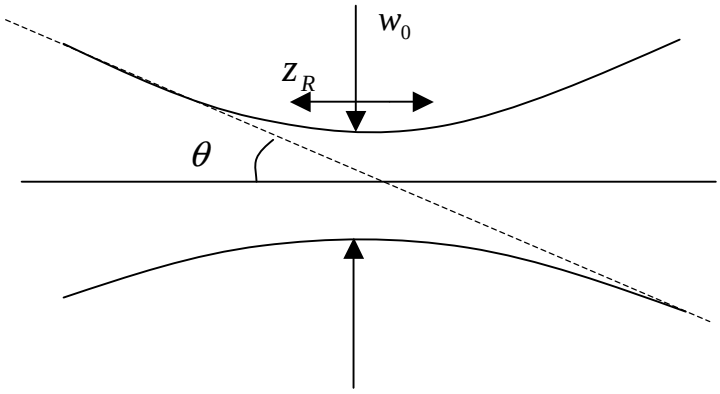

Figure 3.3 Beam Waist ω_0 versus Focal Region z_R

The laser intensity $I(t, z)$ is expressed as

$$I(z,t) = \frac{P_{\max}}{\pi \cdot \omega^2(z)} \times \left\{ \exp\left[(-4\ln 2)\left(t/\tau_p \right)^2 \right] \right\} \tag{3-3-4}$$

In equation (3-3-4), t=0 corresponding to the pulse peak intensity. The spatial propagation of the laser pulse in the classical model is neglected.

The ratio of the laser pulse intensity $I(z,t)$ and the threshold I_{th} is defined as the normalized pulse intensity β:

$$\beta = P_{\max} / P_{th} = I_{\max} / I_{th} \tag{3-3-5}$$

The time $t_B(z)$ that laser intensity reaches the breakdown threshold can be obtained by letting $I = I_{th}$ in equation (3-3-6).

$$t_B(z)_{\pm} = \pm\tau_P \left\{ \frac{1}{4\ln 2} \ln\left[\beta \left(1 + \frac{z^2}{z_R^2} \right)^{-1} \right] \right\}^{\frac{1}{2}} \tag{3-3-6}$$

Referring to the classical model [80], the variation in laser intensity around the focal region is plotted in Figure 3.4 for different times. The breakdown threshold was arbitrarily chosen ($\beta = 2,4$). For a fixed laser power, larger values of β present a lower breakdown threshold. As seen in the Figure, the breakdown region reaches a maximum z_{max}, when t=0, which corresponds to the pulse peak P_{max} arriving at the focal region. In the classical breakdown model, the plasma formation time is much shorter than the pulse duration, and is thus ignored; the plasma is assumed to form immediately once $I > I_{th}$. Since no pulse propagation in the medium is considered, the classical model always predicts an identical result, no matter how short the pulse is.

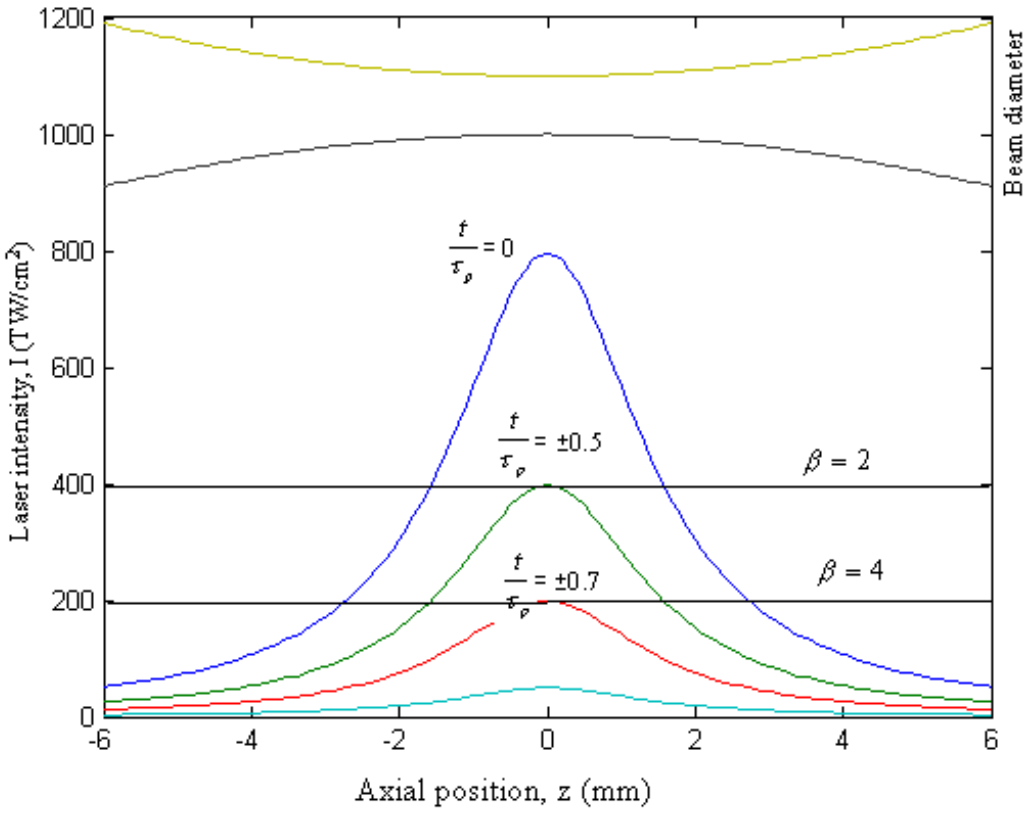

Figure 3.4 Nanosecond Laser Time Dependent Intensity in The Focal Region

3.4 FEMTOSECOND MOVING BREAKDOWN MODEL

The parameter N_z is used to characterize the ratio of the pulse length l_p to the focal region (Rayleigh Range) z_R. [59]

$$N_z = \frac{l_p}{z_R} = \frac{c\tau_p}{z_R} \tag{3-4-1}$$

If $N_z >> 1$, it means that the laser pulse is much larger than the focal region, so the spatial variation in the pulse shape can be ignored. As the pulse duration is reduced to an ultra short regime, pulse propagation time in the focal volume becomes significant, and $N_z << 1$, it implies that the pulse length is relatively small, and hence propagation of the pulse within the focal volume must be considered.

Table 3.1 provides the comparison between nanosecond and femtosecond lasers. The values of N_z in this table decrease significantly with the pulse duration becoming shorter. Thus, in the femtosecond region, the pulse propagation time should be considered.

Table 3.1 Comparison of Values of N_z from Nanosecond Region to Femtosecond Region

No.	λ	w_0	z_R	τ_p	l_p	N_z
1	800 nm	10 μm	400 μm	1 ns	~30 cm	~750
2	800 nm	10 μm	400 μm	10 ps	~3 mm	~7.5
3	800 nm	10 μm	400 μm	100 fs	~30 μm	~0.075

Therefore, accounting for the small spatial extent and propagation of ultra short pulses, a femtosecond moving breakdown model was established based on the classical model. The femtosecond laser intensity is expressed as

$$I(z,t) = \frac{P_{\max}}{\pi \cdot \omega^2(z)} \times \left\{ \exp\left[(-4\ln 2) \left(\frac{t - z/c}{\tau_p} \right)^2 \right] \right\} \qquad (3\text{-}4\text{-}2)$$

The term z/c represents the pulse propagation time in the medium. Point $z = 0$ represents the position of the peak pulse intensity when $t = 0$.

The time at which the laser intensity reaches the breakdown threshold at a given position $t_B(z)$ can be expressed as:

$$t_B(z)_{\pm} = z/c \pm \tau_P \sqrt{\frac{1}{4\ln 2} \ln\left[\beta \left(1 + \frac{z^2}{z_R^2} \right)^{-1} \right]} \qquad (3\text{-}4\text{-}3)$$

where ‘‘-’’ and ‘‘+’’ represent the times that the intensity first and last exceeds breakdown threshold.

A 100 fs pulse breakdown occurring time is calculated according to equation (3-4-3), as shown in Figure 3.5. For β =2, the breakdown starts at $z \approx -1.6$ mm with $t/\tau_p \approx -40$, while for $\beta = 4$, the breakdown starts at $z \approx -2.6$ mm with $t/\tau_p \approx -60$. The pulse length is much shorter than the focal region, which contradicts to the prediction from the classical model (see Figure 3.4), where the breakdown begins at the focus ($z = 0$) at $t/\tau_p \approx -0.5$. For $\beta = 4$, the breakdown occurs even earlier than that predicted by the classical model.

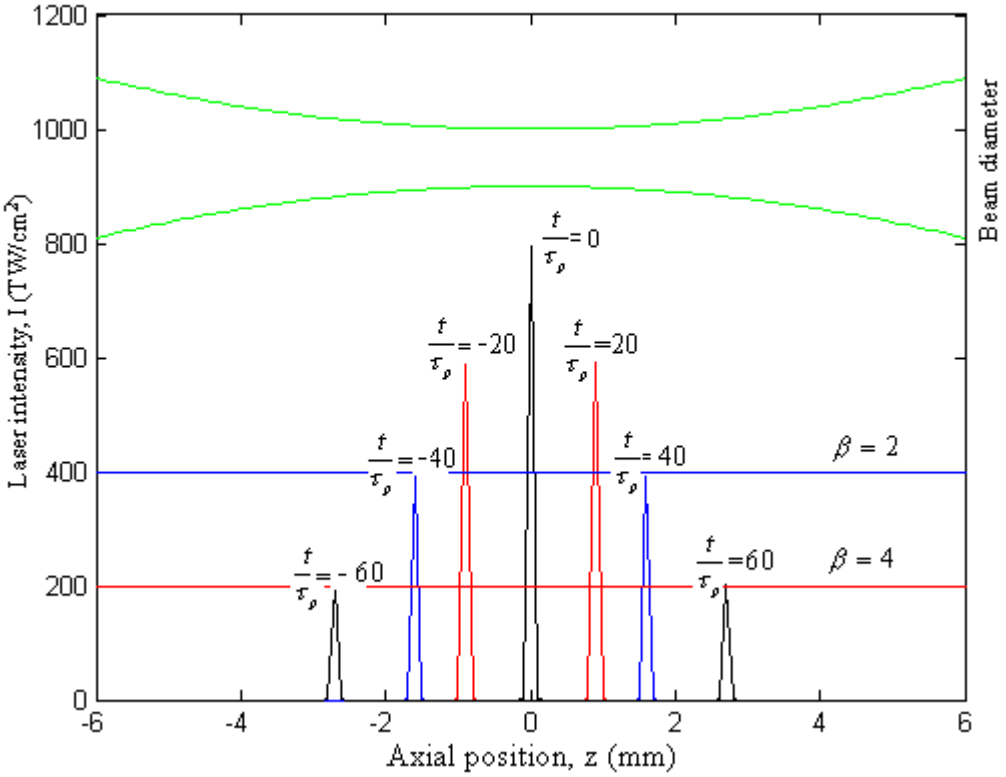

Figure 3.5 Femtosecond Laser Time Dependent Intensity in the Focal Region

By comparison the time dependent intensity in the focal region from nanosecond laser to femtosecond laser (see Figure 3.4 & 3.5), it is concluded that, for a femtosecond laser system, the pulse duration is ultra short, thus the laser pulse no longer completely fills the focal volume and the propagation of pulse must be taken into account. Therefore, to improve the accuracy of the predicted threshold value for femtosecond laser ocular tissue interaction, this modified moving breakdown model was used in this research.

3.5 BREAKDOWN THRESHOLD

3.5.1 BREAKDOWN THRESHOLD CALCULATION

The optical breakdown process normally includes four aspects: multiphoton absorption, avalanche ionization, electron diffusion and electron recombination.

For multiphoton ionization, several photons are absorbed simultaneously by a single molecule. The number of absorbed photons k depends on the ionization potential of the material ΔE and the photon energy $h\omega$:

$$k = \mathrm{Int}\left(\frac{\Delta \mathrm{E}}{h\omega} + 1\right) \tag{3-5-1}$$

$$\omega = 2\pi \cdot c/\lambda \tag{3-5-2}$$

Where function $Int(x)$ gives the integer part of x, h is the Planck's constant, and ω is the laser frequency. The calculated value of k is 3 for 400 nm, 5 for 800 nm and 6 for 1064nm for water.

The electron density produced by multiphoton absorption is below [81].

$$\left[\frac{d\rho(t,z)}{dt}\right]_{mpa} = \frac{2\omega}{9\pi}\left(\frac{m'\omega}{h}\right)^{3/2}\left[\frac{e^2}{16nc\varepsilon_0 m'\Delta \mathrm{E}\omega^2} I(t,z)\right]^k \times \exp(2k)\Phi\left(\sqrt{2\left(k - \frac{\Delta \mathrm{E}}{h\omega}\right)}\right) \tag{3-5-3}$$

where $\Phi(x)$ is the Dawson's Integral, $\Phi(x) = 0.54$ in this work.

In Equation (3-5-3), ρ is the free-electron density as a function of time t and axial position z, I the laser intensity, n the refractive index, c the velocity of light in free space, ε_0 the permittivity of free space, and m' the reduced electron mass, which is approximately half of the electron mass, respectively.

The avalanche ionization rate η_{ava} can be expressed as [81]

$$\eta_{ava} = \frac{1}{\omega^2\tau^2 + 1}\left(\frac{\tau e^2}{nc\varepsilon_0 m\Delta \mathrm{E}} I(t-\tau_{ion}, z) - \frac{m\tau\omega^2}{M}\right) \tag{3-5-4}$$

where m is the rest mass of an electron and M is the mass of the material molecule. In equation (3-5-4), τ_{ion} is the finite time required for momentum transfer to electrons via collisions, $\tau_{ion} = k\tau^2$. Where τ is an estimated value of 1 fs.

The electron diffusion rate η_{diff} is given by

$$\eta_{diff} = \frac{\tau\Delta \mathrm{E}}{3m}\left[\left(\frac{2.4}{w_0}\right)^2 + \left(\frac{1}{z_R}\right)^2\right] \tag{3-5-5}$$

Electron recombination is another process, which reduces the electron population. An empirical value $\eta_{rec} = 2\times10^{-9}\ cm^3/s$ is used for the electron recombination rate.

The electron density ρ is time and position dependent, and it is determined by the multiphoton absorption, avalanche ionization, and electron diffusion and recombination, as shown in equation (3-5-6):

$$\frac{d\rho}{dt} = \left.\frac{d\rho}{dt}\right|_{mpa} + \eta_{ava}\rho - \eta_{diff}\rho - \eta_{rec}\rho^2 \tag{3-5-6}$$

Due to beam focusing, the highest pulse intensity occurs at the focal point $z = 0$, resulting in a corresponding maximum in electron density. When the electron density reaches the critical value,

$$\rho = \rho_{cr} \tag{3-5-7}$$

The corresponding peak intensity is named as the breakdown threshold I_{th}

$$I(z,t) = I_{th} = P_{th} \Big/ \pi \cdot w_0^2 \tag{3-5-8}$$

The parameters used for the threshold calculation are listed in Table 3.2.

Table 3.2 The Constants used in the Simulation

Parameters /constants	Symbol	Value
Laser wavelength	λ	488 nm, 800 nm, 1064 nm
Refractive index	n	1
Vacuum speed of light	c	$3\times10^8 m/s$
Radius of beam waist	w_0	$2.5\mu m$
Band gap of water	ΔE	6.5 eV
Mass of a water molecule	M	$3\times10^{-26} Kg$
Electron mass	m	$9.1\times10^{-31} Kg$
Electron Charge	e	$1.6022\times10^{-19} C$
Time between electron-heavy particle collisions	τ	$1 fs$
Laser pulse duration	τ_p	10 ns, 40 ps, 150 fs

Laser pulse intensity can be used to indirectly determine the critical electron density for optical breakdown. Although this aspect has been investigated by some researchers [81], the accuracy of the results was limited by some factors.

In Noack's work, the breakdown threshold was calculated using the classical Moving Breakdown model [81]. The results are shown in Table 3.3.

Table 3.3 Simulation Result Based on the Classical Moving Breakdown Model. [81] (I_{th} is the measured breakdown threshold. I_{rate} is predicted by rate equation model. I_{rate26} is calculated assuming a critical electron density of 10^{26} m^{-3}, and I_{rate27} refers to a critical electron density of 10^{27} m^{-3}.)

τ_p	λ (nm)	$2w_0$ (μm)	I_{th} $(10^{15} W/m^2)$	I_{rate26} $(10^{15} W/m^2)$	I_{rate27} $(10^{15} W/m^2)$
76 *ns*	750	20.0	0.2	0.4	1.9
6 *ns*	1064	7.7	0.5	0.5	4.0
30 *ps*	1064	4.7	4.5	1.0	4.4
3 *ps*	580	5.0	8.5	7.1	9.0
300 *fs*	580	5.0	47.6	39.0	48
100 *fs*	580	4.4	111	84.0	98

Since the effect of pulse propagation in the focal region was ignored, it was only time dependent. From the comparison between measured and predicted intensity threshold in Table 3.3, it is clear that, the measured intensity data were close to the predicted data in nanosecond pulse duration range when $\rho_{cr} = 10^{26} m^{-3}$; while far from the predicted data when $\rho_{cr} = 10^{27} m^{-3}$; with the pulse duration decreasing into picosecond

and femtosecond ranges, the measured intensity data are close to the predicted data when $\rho_{cr} = 10^{27} m^{-3}$, while far from the predicted data when $\rho_{cr} = 10^{26} m^{-3}$.

In Fan's work [66,67, 80], although pulse propagation in the focal region has been considered, $\rho_{cr} = 10^{26} m^{-3}$ was used as the critical electron density from the nanosecond region to the femtosecond region. While from Noack's result, it is known that $\rho_{cr} = 10^{26} m^{-3}$ is not suitable for the pulse intensity threshold prediction in the femtosecond region.

To improve the accuracy of the modeling result, $\rho_{cr} = 10^{26} m^{-3}$ for the nanosecond range, and $\rho_{cr} = 10^{27} m^{-3}$ for both picosecond and femtosecond ranges were used in our simulation work, as expressed below.

$$\rho cr = f(\tau_p) = \begin{cases} 10^{26} m^{-3} & \tau_p \geq 10^{-9} s \\ 10^{27} m^{-3} & \tau_p < 10^{-9} s \end{cases} \quad (3\text{-}5\text{-}9)$$

Using equation (3-5-10), the pulse energy threshold was calculated.

$$E_{th} = I_{th} \cdot \pi \omega_0^2 \cdot \tau_p \quad (3\text{-}5\text{-}10)$$

3.5.2 RESULTS AND ANALYSIS

Figure 3.6 shows the free electron density evolution in water from the nanosecond pulse duration to the femtosecond pulse duration at different wavelengths. Beam Radius equals $w_0 = 2.5 \mu m$. From Figure 3.6 (a) to Figure 3.6 (i), Curve A is the trend

of electron density evolution at $z = -z_0$, Curve B is the trend of electron density evolution at $z = 0$, and Curve C is the trend of electron density evolution at $z = z_0$. For nanosecond and picosecond pulses, the pulse length l_p is much larger than the focal region z_R, and the spatial variation in the pulse shape is very small. Thus at $-z_0$ (curve A) and z_0 (curve C), the trend of electron density evolution has the same profile. For femtosecond pulses, the pulse length l_p is much smaller than the focal region z_R, the propagation of the pulse within the focal volume is both time and spatial dependent. Thus a difference between curves A and C is clearly observed in the femtosecond region.

In the nanosecond range, when the electron density reaches $\rho_{\max}$, due to plasma resonance with the incident laser light, the plasma becomes highly reflective, and it blocks further incoming laser light. In this case, the electron density begins decreasing because there is no more energy contributing to plasma formation. Here the critical electron density $\rho_{cr} = 10^{26} m^{-3}$ does not exceed this limit. The amount of free electrons is mainly produced by cascade ionization rather than multiphoton ionization. Interaction with long pulses is a single photon process, and the penetration depth of laser light is determined by the absorption coefficient at the laser wavelength. Because of the long pulse duration, typically around 10 ns to 20 ns, thermal and mechanical relaxation competes with tissue evaporation. At 488 nm, 800 nm, and 1064 nm (See Figures 3.6 (a), (d) & (g)), the corresponding laser pulse intensity thresholds are $0.26 \times 10^{15} W/m^2$, $0.15 \times 10^{15} W/m^2$, $0.12 \times 10^{15} W/m^2$ respectively.

Below the nanosecond range, because of the decreasing pulse duration, the pulse energy may not be used to form the plasma and then block the laser light, in stead it may be deposited to the molecules. . This means there is a possibility for the electron density to exceed their limitation, and therefore a higher critical electron density $\rho_{cr} = 10^{27} m^{-3}$ is reasonable in the picosecond region and the femtosecond region.

In the picosecond region, the pulse duration is below the rise time of the electron cascade. In order to meet the critical electron density, a higher ionization rate is needed, thus a higher irradiance threshold is required when the laser pulse duration decreases. In this condition, multiphoton ionization replaces the role of cascade ionization and becomes the main factor in electron evolution, it is because that multiphoton ionization is more dependent on laser irradiance ($\propto I^k$) than cascade ionization ($\propto I$), where k is the number of photons involved in multiphoton ionization. It means that with the pulse duration decreasing, the importance of multiphoton ionization is increasing. In the picosecond range (See Figures 3.6 (b), (e) & (h)), the intensity threshold at wavelengths 488 nm, 800 nm, and 1064 nm are $2.5\times10^{15} W/m^2$, $1.2\times10^{15} W/m^2$, $0.9\times10^{15} W/m^2$, respectively.

In the femtosecond region, the optical breakdown is dominated by multiphoton ionization. Electron recombination is negligible because the recombination process is much slower than the pulse duration. Femtosecond lasers rely on a nonlinear (i.e. multi-photon) mechanism. For example, at wavelength 800 nm, five photons must be absorbed to overcome the water bandgap, and an additional five photons are required to initiate an electron avalanche. This avalanche leads to optical breakdown, and the resulting plasma mediates the ablation process [66, 77]. Because a high intensity

required to absorb these photons, a higher value of critical electron density is necessary to create the plasma energy density. At wavelengths 488 nm, 800 nm, and 1064 nm (See Figures 3.6 (c), (f) & (i)), the intensity thresholds are $60\times10^{15} W/m^2$, $48\times10^{15} W/m^2$ and $35\times10^{15} W/m^2$, respectively.

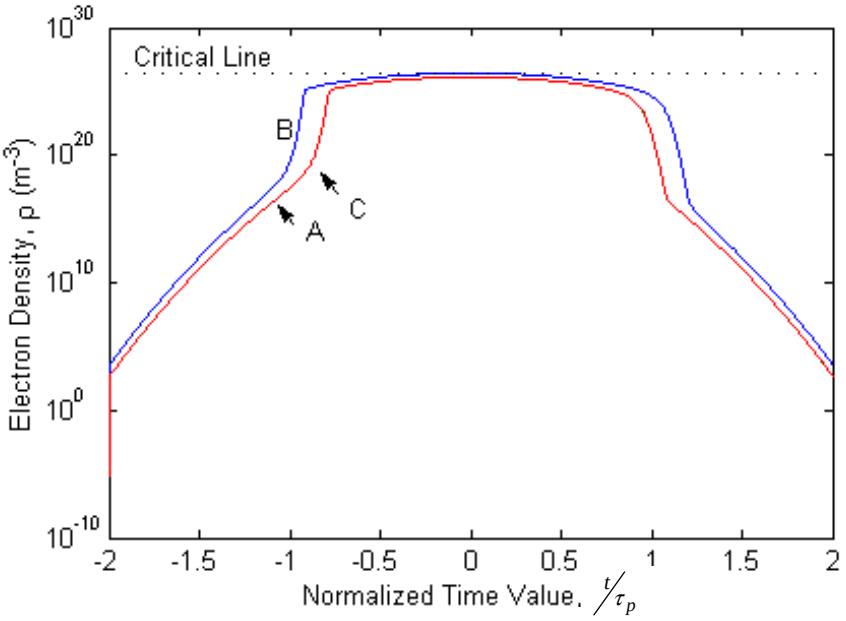

Figure 3.6 (a) Argon laser, λ = 488 nm, τ_p = 10 ns, I_{th} = 0.26 x 10^{15} W/m^2, ρ_{cr} = 10^{26} m^{-3}

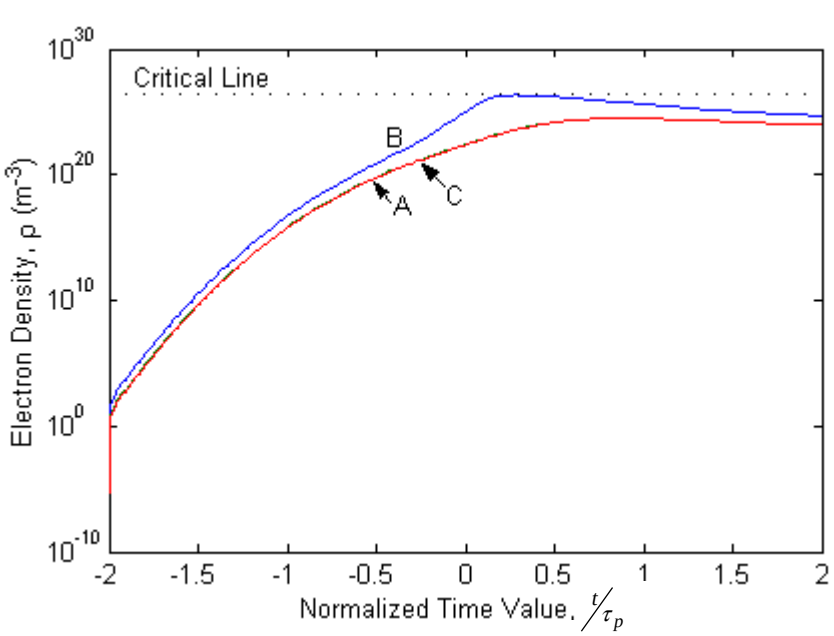

Figure 3.6 (b) Argon laser, λ = 488 nm, τ_p = 40 ps, I_{th} = 2.5 x 10^{15} W/m^2, ρ_{cr} = 10^{27} m^{-3}

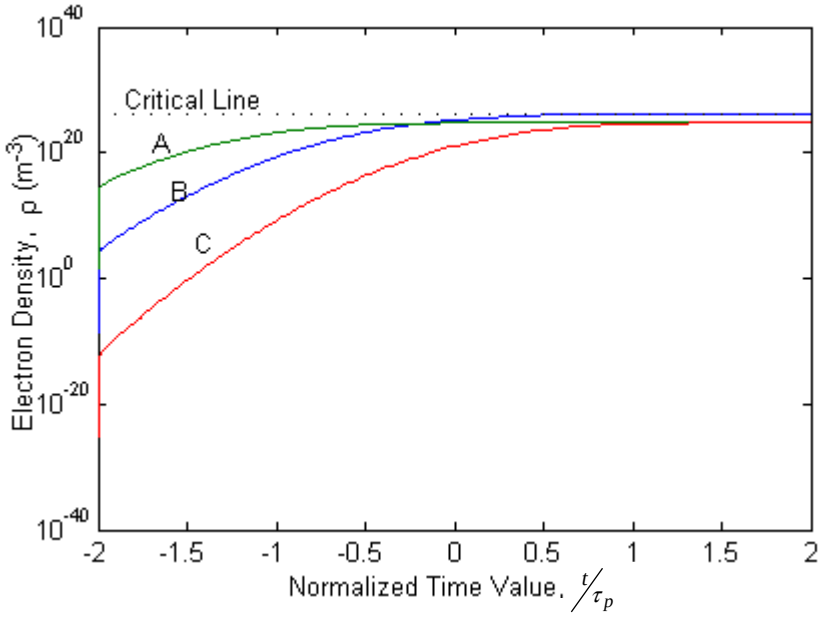

Figure 3.6 (c) Argon laser, λ = 488 nm, τ_p = 150 fs, I_{th} = 60 x 10^{15} W/m^2, ρ_{cr} = 10^{27} m^{-3}

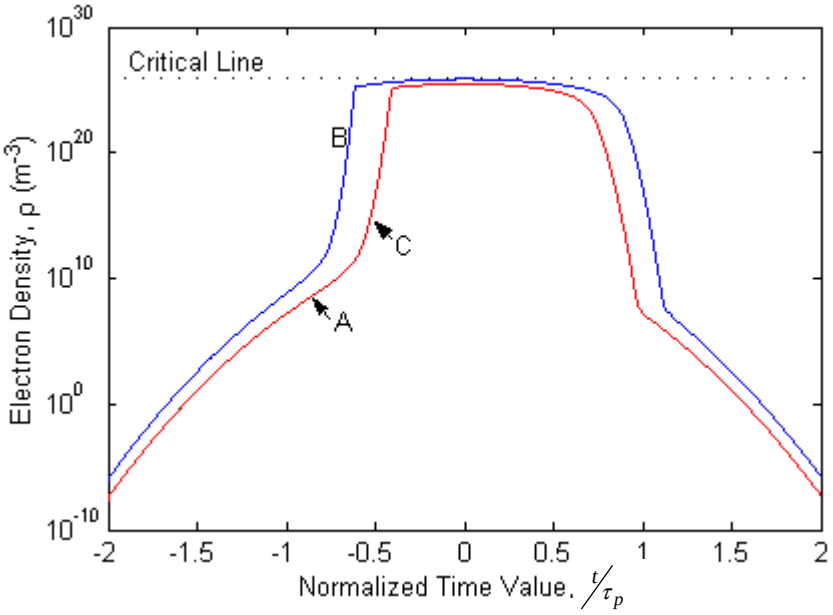

Figure 3.6 (d) Ti:Sapphire laser, λ = 800 nm, τ_p = 10 ns, I_{th} = 0.15 x 10^{15} W/m^2, ρ_{cr} = 10^{26} m^{-3}

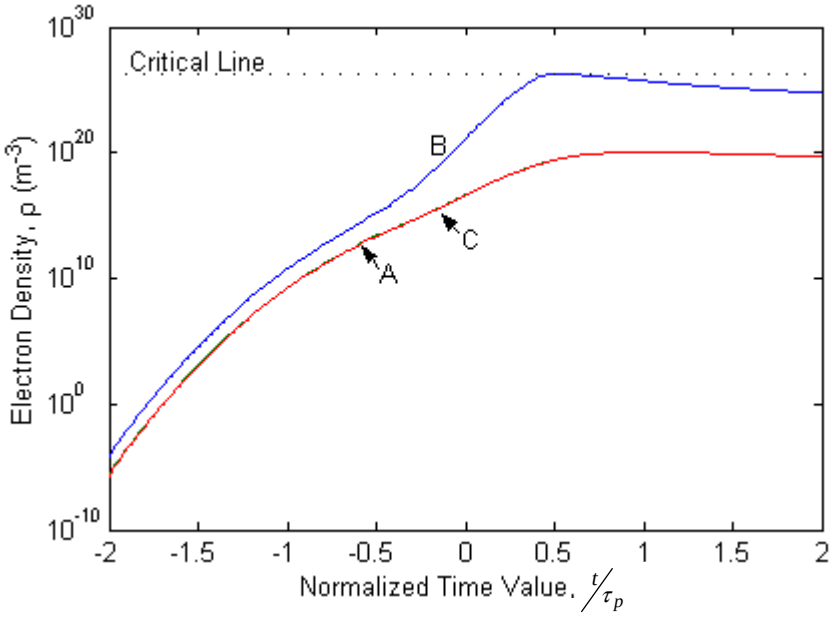

Figure 3.6 (e) Ti:Sapphire laser, λ = 800 nm, τ_p = 40 ps, I_{th} = 1.2 x 10^{15} W/m^2, ρ_{cr} = 10^{27} m^{-3}

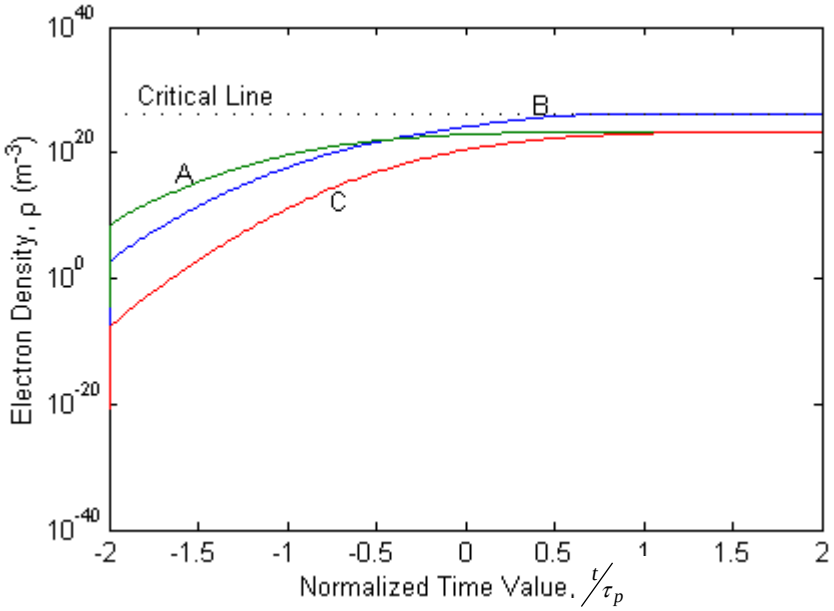

Figure 3.6 (f) Ti:Sapphire laser, λ = 800 nm, τ_p = 150 fs, I_{th} = 48 x 10^{15} W/m^2, ρ_{cr} = 10^{27} m^{-3}

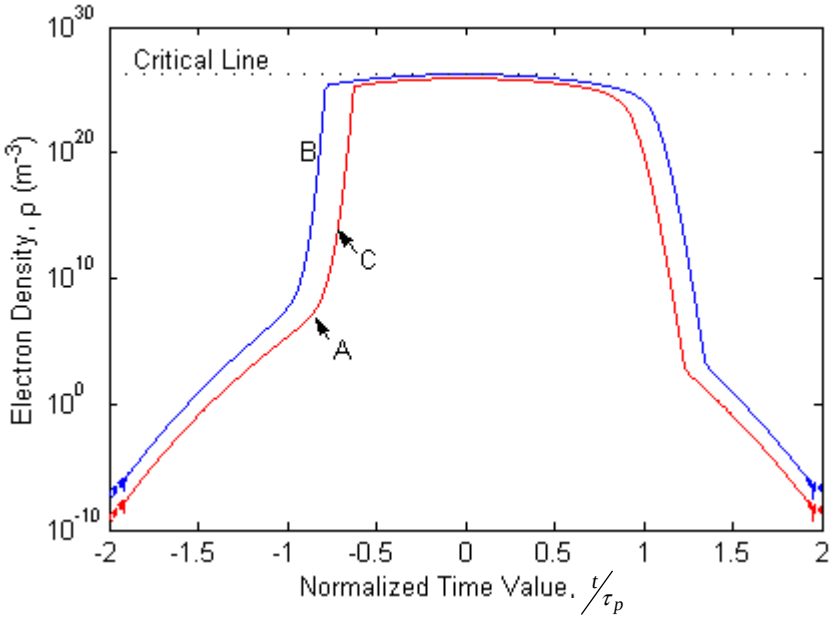

Figure 3.6 (g) YAG laser, λ = 1064 nm, τ_p = 10 ns, I_{th} = 0.12 x 10^{15} W/m^2, ρ_{cr} = 10^{26} m^{-3}

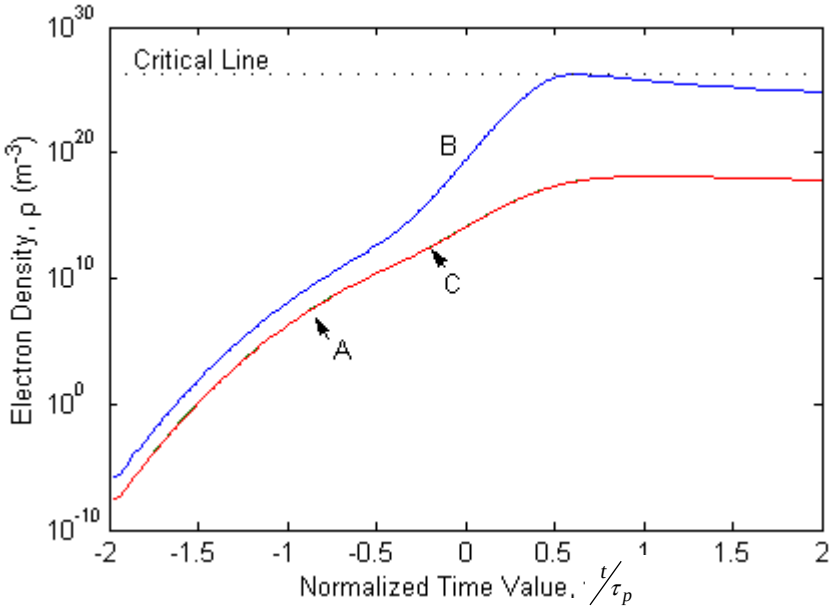

Figure 3.6 (h) YAG laser, λ = 1064 nm, τ_p = 40 ps, I_{th} = 0.9 x 10^{15} W/m^2, ρ_{cr} = 10^{27} m^{-3}

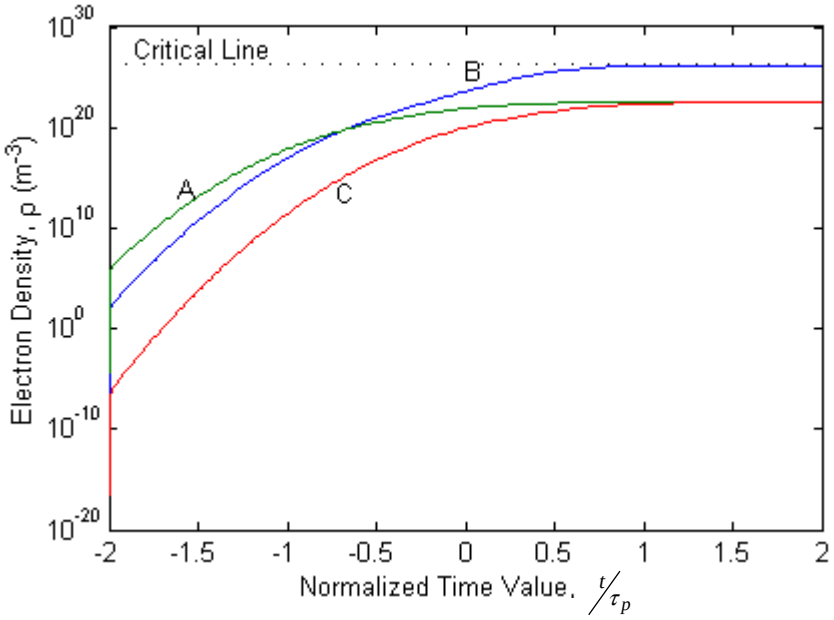

Figure 3.6 (i) YAG laser, λ = 1064 nm, τ_p = 150 fs, I_{th} = 35 x 10^{15} W/m^2, ρ_{cr} = 10^{27} m^{-3}

Figure 3.6 Free Electron Density Evolution in Pure Water at Different Wavelengths and Different Pulse Durations

The energy thresholds corresponding to different wavelengths and pulse durations are shown in Table 3.4. The relationship between intensity threshold and pulse duration is shown in Figure 3.7 (a), and the relationship between the pulse energy threshold and the pulse duration is shown in Figure 3.7 (b).

Table 3.4 Energy Thresholds Corresponding to Different Wavelengths and Pulse Durations

τ_p	10 ns			40 ps			150 fs		
$\lambda(nm)$	488	800	1064	488	800	1064	488	800	1064
$I_{th}(10^{15}W/m^2)$	0.26	0.15	0.12	2.5	1.2	0.9	60	48	35
$E_{th}(\mu J)$	51.025	29.44	23.55	1.9625	0.942	0.7065	0.1766	0.1413	0.103

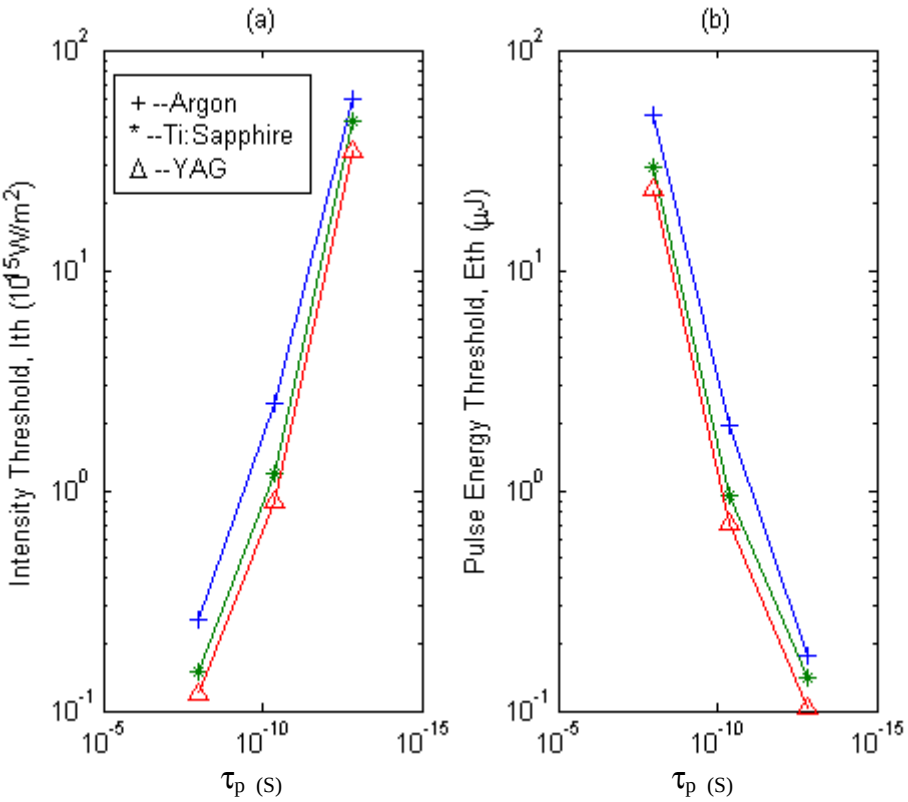

Figure 3.7 (a) Intensity Threshold vs. Pulse Duration;
(b) Pulse Energy Threshold vs. Pulse Duration

From Table 3.4 and Figure 3.7 (a), it can be seen that the pulse intensity threshold increases around 3 orders of magnification from the nanosecond region to the femtosecond region. Interaction with long pulses is a single photon process, thus the amount of free electrons is mainly produced by cascade ionization in the nanosecond range. With the pulse duration decreasing, the importance of multiphoton ionization is increasing. In the picosecond range, the pulse duration is below the rise time of the electron cascade. In order to meet the critical electron density, a higher ionization rate is needed, thus a higher intensity threshold is required when the laser pulse duration decreases. In the femtosecond region, because the recombination process is much slower than the pulse duration, electron recombination is negligible. The optical breakdown is dominated by multiphoton ionization. An even higher value of critical

electron density is necessary to create the plasma energy density. Thus the corresponding pulse intensity threshold is also higher. As expressed in Equation (3-5-9), the pulse energy depends on both intensity threshold and pulse duration. The decrease of pulse duration is larger than the increase of intensity threshold, thus the pulse energy has an opposite dependence on the pulse duration compared to intensity threshold. It can be seen from Figure 3.7 (b), the pulse energy threshold decreases near to 3 orders of magnification. Therefore it yields a potential that with decreasing pulse duration from the nanosecond region to the femtosecond region, the collateral damage may be significantly reduced.

3.6 THERMAL INCREASE

3.6.1 THERMAL INCREASE DERIVATION

During optical breakdown, the energy delivered to the tissue is transmitted, reflected, scattered, or absorbed [83]. Laser energy absorbed by the excited electrons can be released in radiative and nonradiative fashions. The nonradiative fashion includes convective and conductive (diffusive) transport, as seen in Figure 3.8. For those transited in nonradiative fashion, the energy can be stored in the bulk material as thermal energy, which gives rise to a sharp temperature increase within the breakdown region.

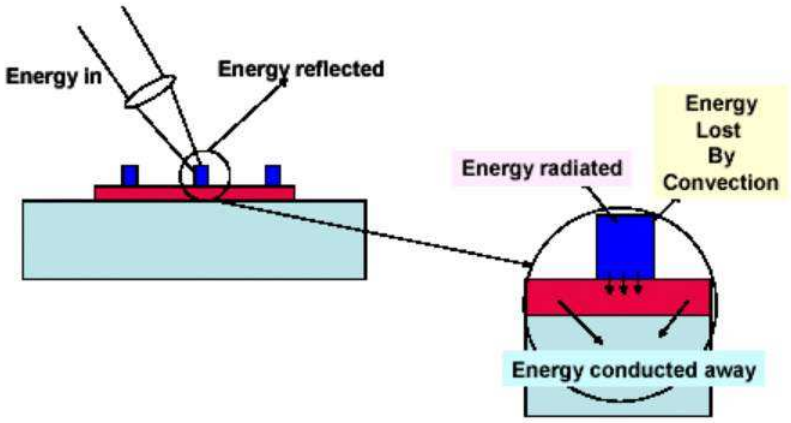

Figure 3.8 Schematic of Energy Absorption Consequence [84]

By far the most important heat transport factor is the heat diffusion from the higher temperature irradiated region into the cooler surrounding tissue. The rates and dimensions involved determine the spatial region that reaches high temperatures, and this region is so-called Heat Affected Zone (HAZ) [84]. The time and space dependent heat equation T(*x*,*z*,*t*) is expressed as below:

$$\frac{\partial T(x,z,t)}{\partial t} = \frac{S(x,z,t)}{C_p} + \frac{K\nabla^2 T(x,z,t)}{\rho_m C_p} \qquad (3\text{-}6\text{-}1)$$

where K is the thermal conductivity with units of $J/\sec \cdot m \cdot K$, and ρ_m is the material density (kg/m^3), C_p is specific heat ($J/kg \cdot K$). $S(x,z,t)$ is the heat source, which is the pulse energy in our work. Using equation (3-6-1), temperature increase in the breakdown region is evaluated. The material property values of water and ocular tissues are listed in Table 3.5.

Table 3.5 Material Properties of Water and the Concerned Eye Tissues [85]

Material	Thermal conductivity K J/sec.m.K	Specific heat *Cp* J/kg.K	Density ρ_m Kg/m^3
Water	0.61593	4.19×10^3	1.0×10^3
Cornea	0.3503	3.645×10^3	1.062×10^2
Aqueous	0.5784	4.1833×10^3	9.96×10^2
Iris	1.0056	3.1844×10^3	1.1×10^3

3.6.2 RESULTS AND ANALYSIS

Figure 3.9 (a-i) shows the temperature increase in water by the given source irradiance from the nanosecond pulse duration to the femtosecond pulse duration with different wavelengths.

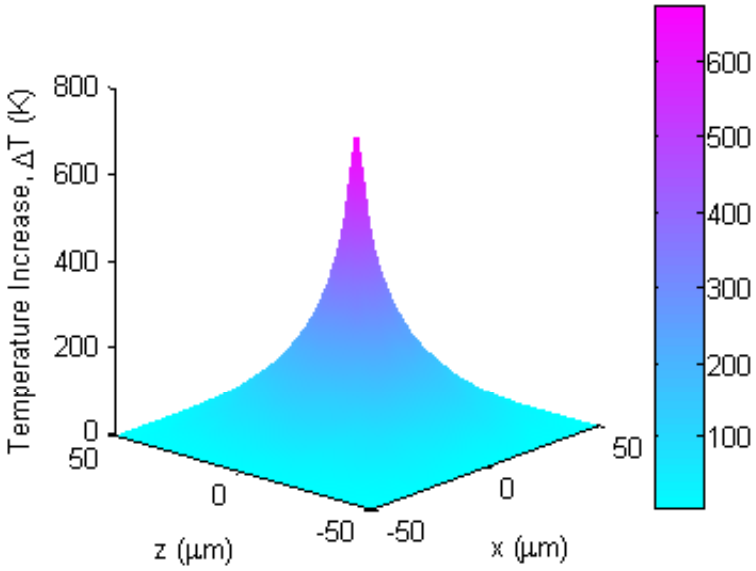

Figure 3.9 (a) Argon laser, λ = 488 nm, τ_p = 10 ns, E_{th} = 51.025 μJ, ΔT= 660 K

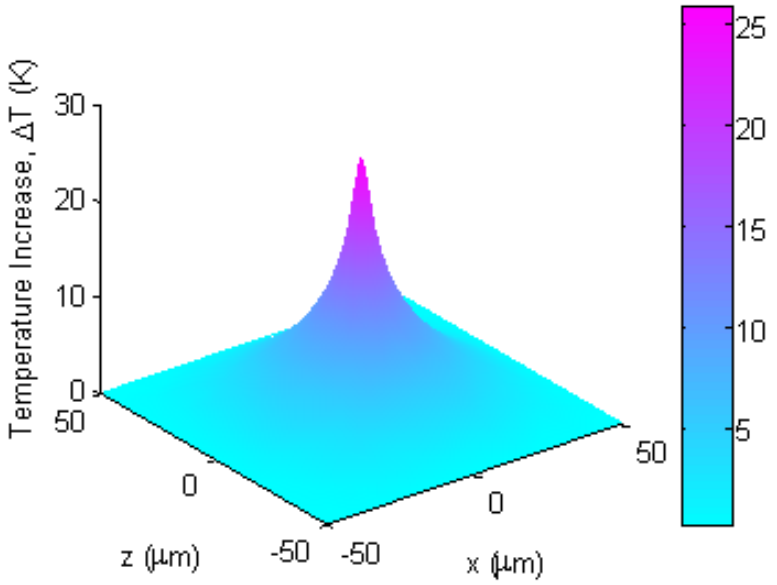

Figure 3.9 (b) Argon laser, λ = 488 nm, τ_p = 40 ps, E_{th} = 1.963 μJ, ΔT= 26 K

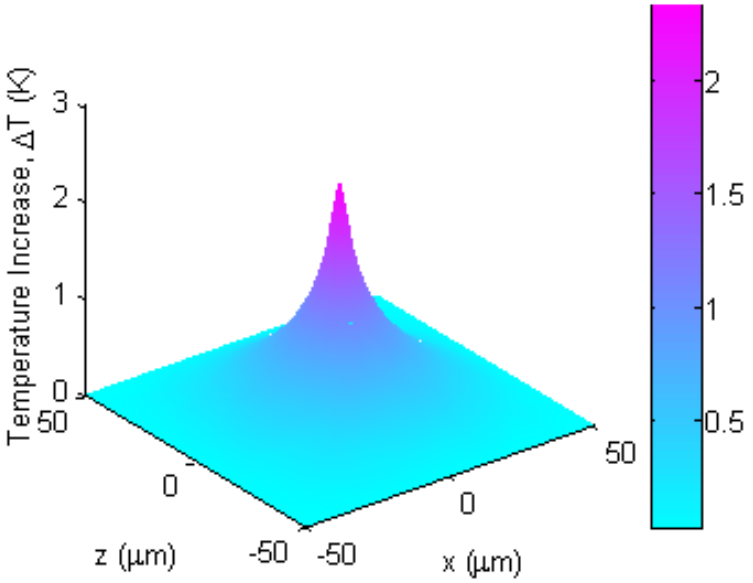

Figure 3.9 (c) Argon laser, λ = 488 nm, τ_p = 150 fs, E_{th} = 0.1766 μJ, ΔT= 2.3 K

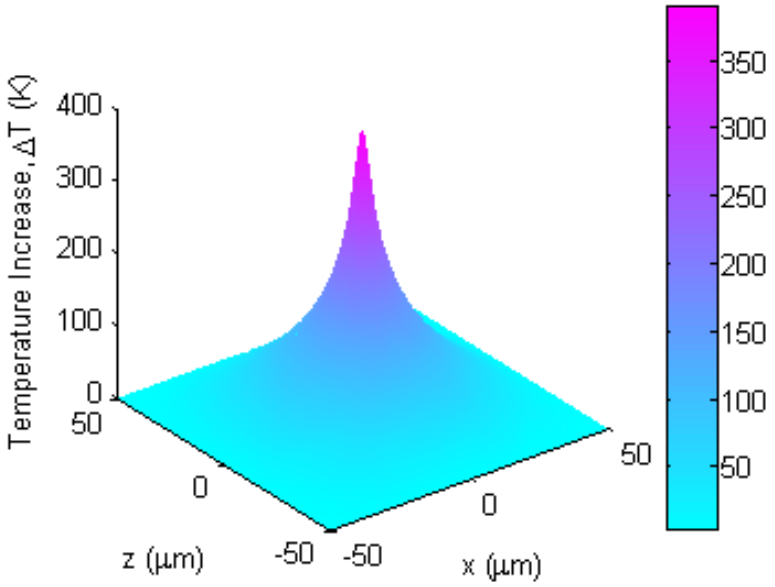

Figure 3.9 (d) Ti:Sapphire laser, λ = 800 nm, τ_p = 10 ns, E_{th} = 29.438 μJ, ΔT= 370 K

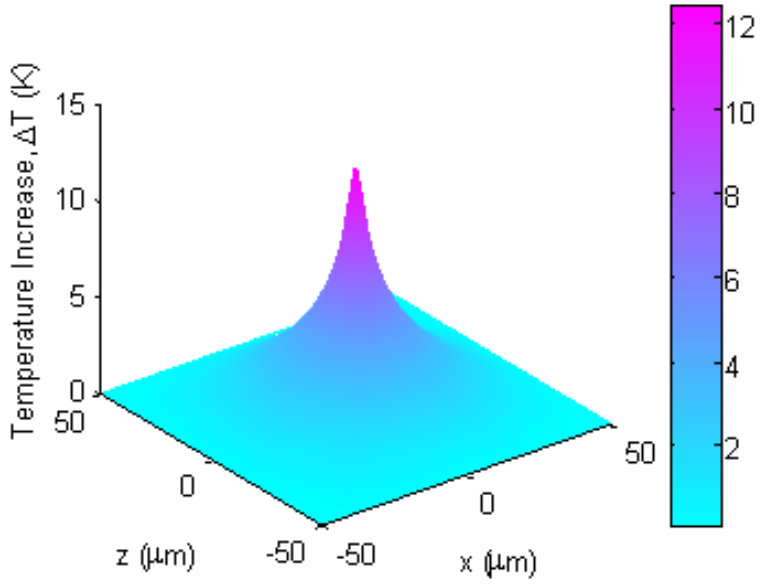

Figure 3.9 (e) Ti:Sapphire laser, λ = 800 nm, τ_p = 40 ps, E_{th} = 0.942 μJ, ΔT= 12.2 K

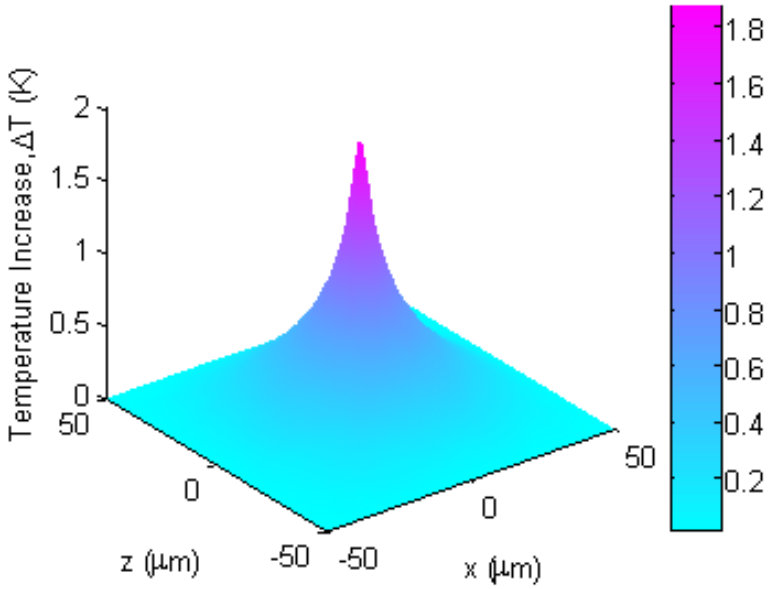

Figure 3.9 (f) Ti:Sapphire laser, λ = 800 nm, τ_p = 150 fs, E_{th} = 0.1413 μJ, ΔT= 1.85 K

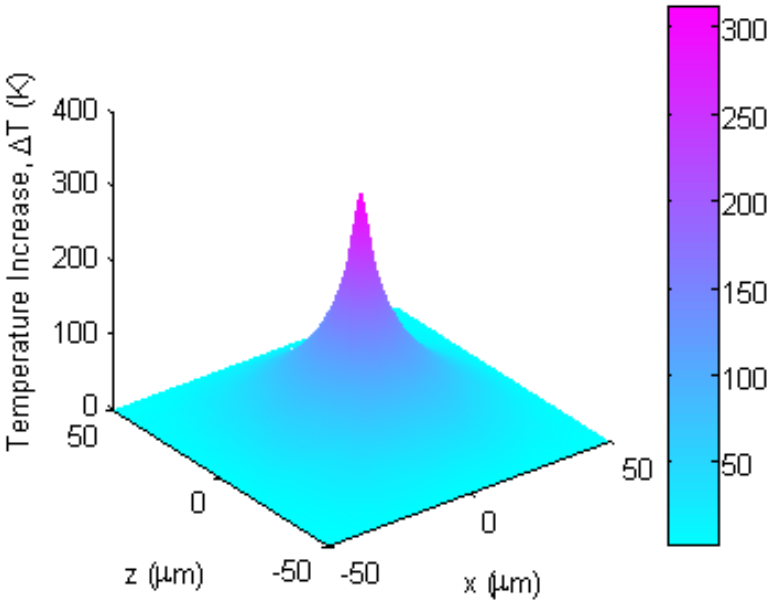

Figure 3.9 (g) YAG laser, λ = 1064 nm, τ_p = 10 ns, E_{th} = 23.55 μJ, ΔT= 310 K

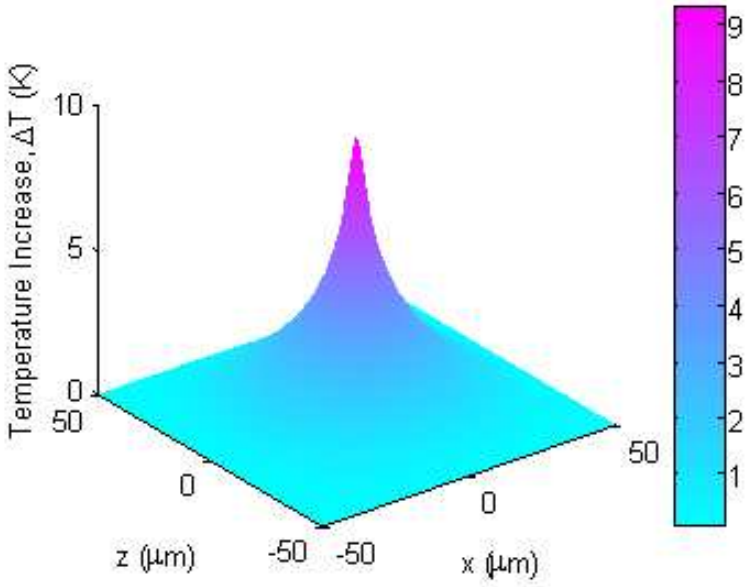

Figure 3.9 (h) YAG laser, λ = 1064 nm, τ_p = 40 ps, E_{th} = 0.7065 μJ, ΔT= 9.2 K

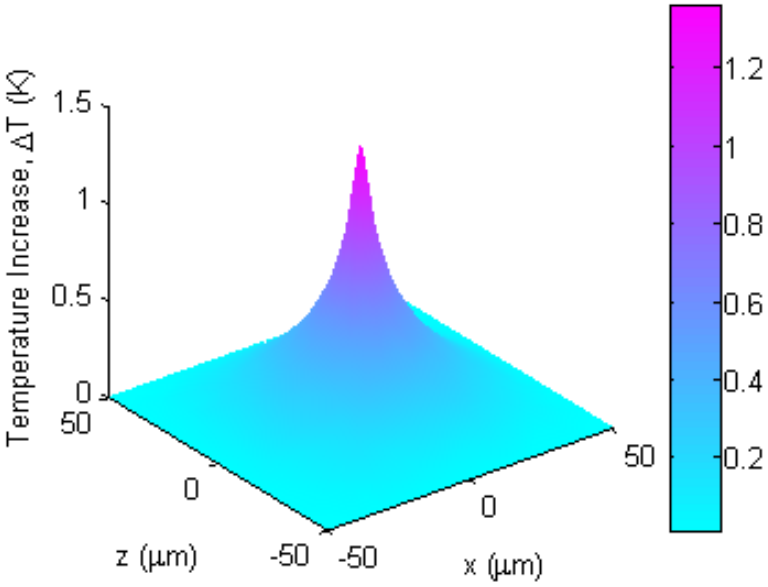

Figure 3.9 (i) YAG laser, λ = 1064 nm, τ_p = 150 fs, E_{th} = 0.103 μJ, ΔT= 1.3 K

Figure 3.9 Temperature Increase Profile in Water by A Given Heat Source from the Nanosecond Pulse Duration to the Femtosecond Pulse Duration with Different Wavelengths

The normal temperature of the eye tissue is about $37^{\circ}C$. In the nanosecond region, the temperature increase is more than 100 $^{\circ}$C (ΔT >100 K), so the temperature may reach $137^{\circ}C$ or even higher with nanosecond pulse irradiance in a very short time, and it may cause significant thermal damage (see Table 3.6 [36]). With reduced pulse duration, the temperature increase decreases rapidly. In the femtosecond region, the temperature increase is less than 5 $^{\circ}$C (ΔT <5 K) for all the wavelengths studied, and there will be no obvious thermal damage beyond the target. In addition, for all the three types of lasers, the temperature increase in the femtosecond region is very close, thus it can be concluded that the wavelength will no longer make a big difference for the thermal effect when the pulse duration decreases into the femtosecond region. Figure 3.10 gives the comparison of the temperature increase of each case shown in Figure 3.9.

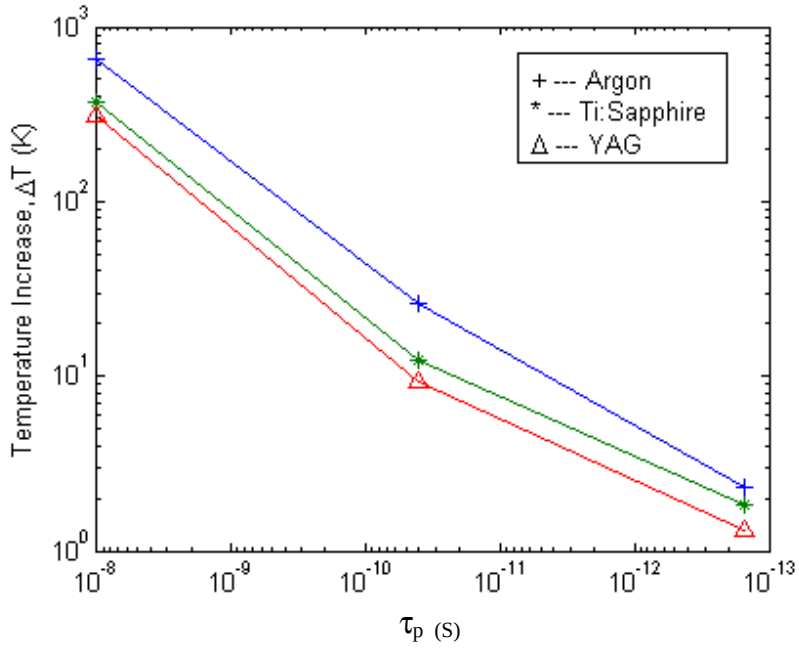

Figure 3.10 Comparison of Temperature Increase in Water from the Nanosecond Pulse Duration to the Femtosecond Pulse Duration with Different Wavelengths

Table 3.6 Thermal Effect of Laser Radiation [38]

Temperature, ^{o}C	Biological Effect
37	Normal
45	Hyperthermia
50	Reduction in Enzyme Activity, Cell Immobility
60	Denaturation of Proteins and Collagen, Coagulation
80	Permeabilization of Membranes
100	Vaporization, Thermal Decomposition
>150	Carbonization
>300	Melting

Based on thermal increase study in water, the temperature increases in the eye tissues were investigated and the results are listed in Table 3.7. The threshold pulse irradiance at the corresponding pulse duration was used as the heat source. Because of the decreasing pulse energy threshold, the temperature increase reduces from the nanosecond region to the femtosecond region. Due to the differing material properties (Table 3.5), the temperature increase varies in different tissues. These provide a source of valuable information for the study on femtosecond application in ophthalmology, especially in glaucoma surgery.

Table 3.7 Temperature Increases in Ocular Tissues

Material	Temperature increase, ΔT (K)								
	Argon / Pulse duration			Ti:Sapphire /Pulse duration			YAG / Pulse duration		
	10 ns	40 ps	150 fs	10 ns	40 ps	150 fs	10 ns	40 ps	150 fs
Water	660	26	2.3	370	12.2	1.85	310	9.2	1.3
Cornea	1150	46	4.2	690	21	3.2	540	16.5	2.3
Aqueous	710	28	2.4	410	13	1.9	330	9.6	1.45
Iris	410	15.6	1.42	230	7.5	1.12	186	5.6	0.83

Figure 3.11 shows the comparison of temperature increase in water and ocular tissues at different wavelengths. Figure 3.11 (a) is at wavelength 488 nm, the samples compared together are water, cornea, aqueous, and iris. With the same heat input, the highest temperature increase response occurs in the cornea, the lowest in iris. In the middle are aqueous and water, and the temperature increase responses in both of them are quite close. Figure 3.11 (b) & (c) are the responses at wavelengths 800 nm and 1064 nm, respectively.

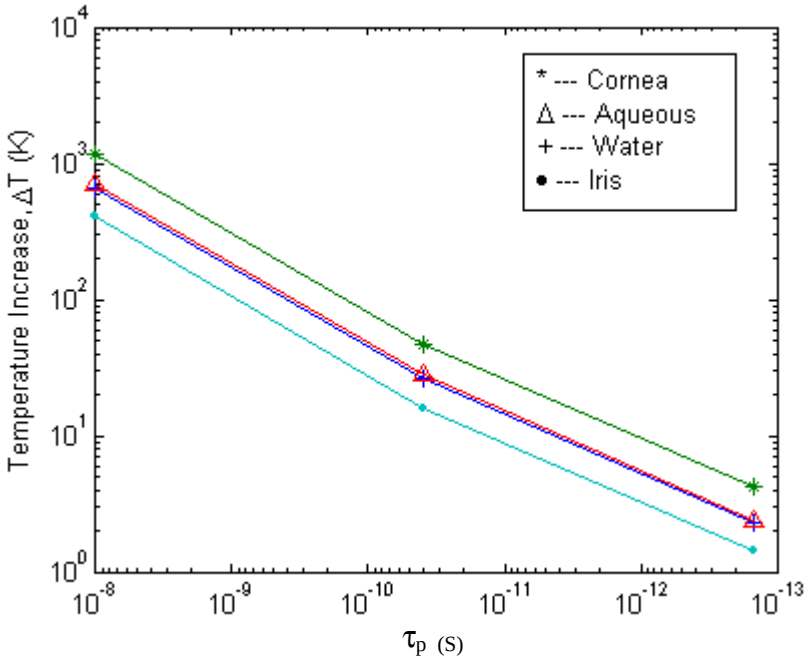

Figure 3.11 (a) Laser source: Argon, λ = 488 nm

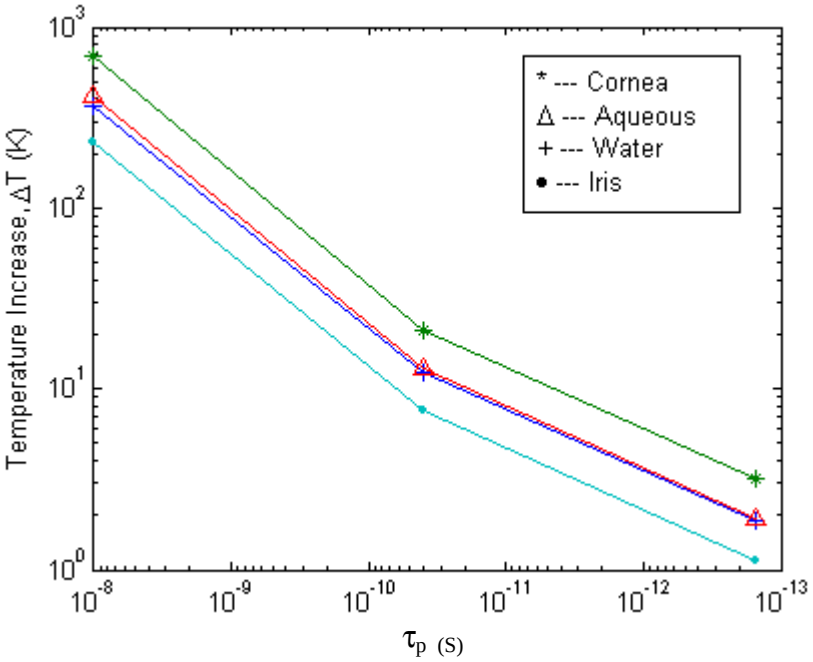

Figure 3.11 (b) Laser source: Ti:Sapphire, λ = 800 nm

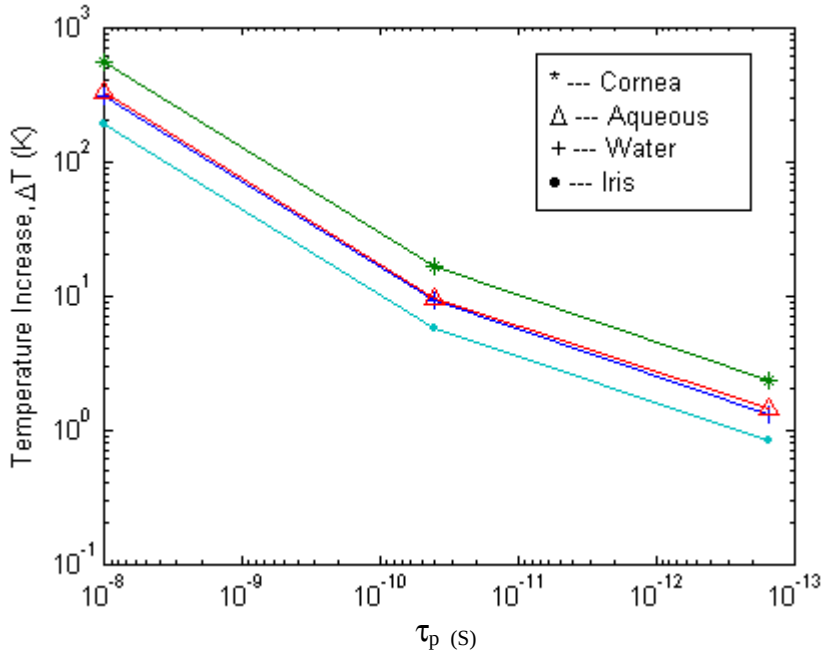

Figure 3.11 (c) Laser source: YAG, λ = 1064 nm

Figure 3.11 Comparison of Temperature Increase in Water and Ocular Tissues at Different Wavelengths

From Figure 3.11, it can be seen that the thermal responses follow the same trend with different laser sources. In addition, referring to Table 3.6, the results illuminated in Figure 3.11 shows the safety of femtosecond pulses for laser-ocular tissue interaction.

3.7 SUMMARY

In this chapter, based on the femtosecond moving breakdown theory, the optical breakdown threshold in water was studied. The thermal increases by the irradiance of pulse energy were calculated both in water and ocular tissues.

The comparison of the time dependent intensity in the focal region from nanosecond laser to femtosecond laser shows the laser pulse no longer completely fills the focal volume for a femtosecond laser system, and the propagation of pulse must be taken into account.

For the laser-induced optical breakdown in water, in the nanosecond pulse region, the laser pulse intensity thresholds at 488 nm, 800 nm, and 1064 nm are $0.26\times10^{15}W/m^2$, $0.15\times10^{15}W/m^2$, $0.12\times10^{15}W/m^2$, respectively. A higher irradiance threshold is required when the laser pulse duration decreases. Multiphoton ionization replaces the role of cascade ionization and becomes important in electron revolution. In the picosecond range, the intensity threshold at wavelengths 488 nm, 800 nm, and 1064 nm are $2.5\times10^{15}W/m^2$, $1.2\times10^{15}W/m^2$, $0.9\times10^{15}W/m^2$ respectively. In the femtosecond region, the optical breakdown is dominated by multiphoton ionization. Electron recombination is negligible. The pulse intensity thresholds at wavelengths 488nm, 800nm, and 1064nm are increasing to $60\times10^{15}W/m^2$, $48\times10^{15}W/m^2$ and $35\times10^{15}W/m^2$, respectively.

From the nanosecond region to the femtosecond region, the intensity threshold for optical breakdown in water increases around 3 orders of magnification, and the pulse energy threshold necessary for optical breakdown decreases near to 3 orders of magnification. Therefore it yields a potential to reducing the collateral damage.

In the nanosecond region, the temperature increase is more than 100K. While with pulse duration decreasing, the temperature increase decreases rapidly. In the femtosecond region, the temperature increase is below $5K$ for all the wavelengths studied. The results of thermal increase in femtosecond range show the safety of

femtosecond pulses during laser-ocular tissue interaction. These provide a source of valuable information for femtosecond application in laser iridotomy.

CHAPTER FOUR

MONTE CARLO SIMULATION ON LIGHT PROPAGATION IN TURBID OCULAR TISSUE DURING CYCLOPHOTOCOAGULATION

4.1 INTRODUCTION

The Cyclophotocoagulation (CPC) procedure delivers the laser light through conjunctiva and sclera to the ciliary body. YAG, Argon, and Diode lasers in the nanosecond range are currently in clinical use. While some limitations still exist, for example, the risk of thermal damage in the surgery, or the requirement for complex laser delivery systems. In this chapter, to improve the efficiency of laser cyclophotocoagulation surgery, light propagation in ocular tissue was studied. Two main aspects were carried out: the optical properties measurement of ocular tissues; Monte Carlo simulation of energy transmission, absorption and reflection.

4.2 OPTICAL PROPERTIES MEASUREMENT

4.2.1 TISSUE OPTICAL PROPERTIES

The most important physical phenomena affecting light propagation in biological tissue are absorption and scattering [86]. They are wavelength dependent (see Figure 4.1). The refractive index varies very little on a macroscopic scale and is typically around 1.40 for most tissue types.

The absorption coefficient μ_a can be defined as [86]

$$dI = -\mu_a I dx_m \tag{4-2-1}$$

Where *dI* is the differential change of the intensity *I* of a collimated light beam traversing an infinitesimal path dx_m through a homogeneous medium with absorption coefficient μ_a.

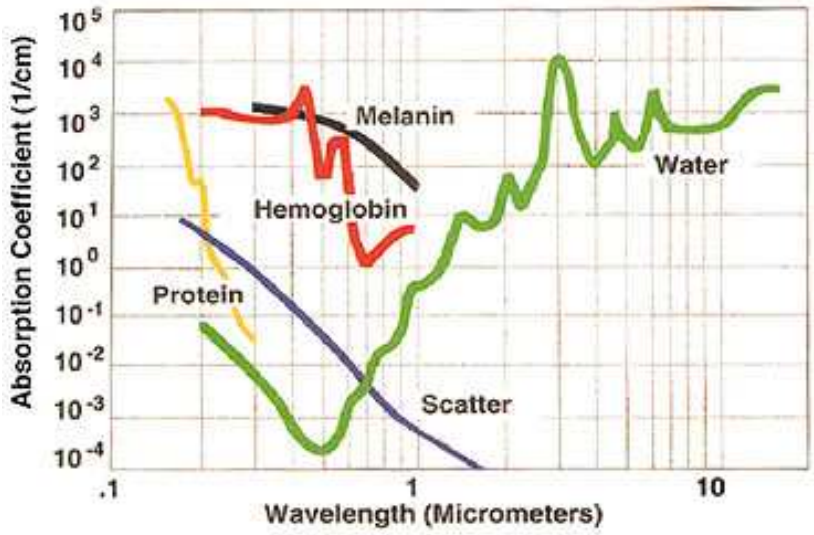

Figure 4.1 Tissue Absorption Coefficients for Various Wavelengths [87]

Integration over a thickness x_m yields

$$I = I_0 e^{-\rho \mu_a x_m} \tag{4-2-2}$$

The absorption coefficient can also be expressed in terms of particle density ρ_m and absorption cross section σ_a as

$$\mu_a = \rho_m \sigma_a \tag{4-2-3}$$

giving the *Beer-Lambert* law

$$I = I_0 e^{-\rho \sigma_a x_m} \tag{4-2-4}$$

The reciprocal $1/\mu_a$ is called the absorption path length and equals the mean free path a photon travels between consecutive absorption events.

The transmission T_t is defined as the ratio of transmitted to incident intensity

$$T_t = \frac{I}{I_0} \tag{4-2-5}$$

Scattering of light in biological tissue is caused by refractive index mismatches at microscopic boundaries such as cell membranes, organelles, etc. In the same manner as for absorption, one can define a scattering coefficient, μ_s (mm^{-1}), for a collimated source, such that

$$I = I_0 e^{-\mu_s x_m} \tag{4-2-6}$$

where I is the non-scattered component of light after traversing a non-absorbing sample of thickness x. In terms of particle density ρ_m and scattering cross section σ_s, the scattering coefficient is

$$\mu_s = \rho_m \sigma_s \tag{4-2-7}$$

The scattering path length $1/\mu_s$ is the average distance a photon travels between consecutive scattering events.

When a photon experiences a scattering event along a direction $\mathbf{e}_s$, the angular probability of it being scattered into direction $\mathbf{e}_s'$ is given by the normalised phase

function f ($\mathbf{e}_s$, $\mathbf{e}_s'$). For random soft tissues, it can be assumed that the probability distribution is a function of the angle between the incident and scattered photon only, and does not depend on the angle of incidence relative to the scatterer. Hence the phase function can be expressed as [88]

$$f\left(\mathbf{e}_s, \mathbf{e}_s'\right) = f\left(\cos\theta\right) \tag{4-2-8}$$

The anisotropy can be characterized in terms of the mean cosine of the scattering angle, called the anisotropy factor g:

$$g = \int_{-1}^{1} \cos\theta \cdot f\left(\cos\theta\right) d\cos\theta \tag{4-2-9}$$

The limiting cases are $g = 0$ for perfectly isotropic scattering, and $g = 1$ for complete forward scattering of the incident wave. Biological tissues in the NIR wavelength range are strongly forward scattering, and their anisotropy factors are typically in the range $0.69 \le g \le 0.99$. The transport (or reduced) scattering coefficient μ_s' is defined as

$$\mu_s' = \mu_s\left(1-g\right) \tag{4-2-10}$$

This quantity represents the equivalent isotropic scattering coefficient. A total attenuation coefficient can be defined as

$$\mu_t = \mu_s + \mu_a \tag{4-2-11}$$

Where $1/\mu_t$ is referred to as the mean free path between either a scattering or absorption event.

The optical property parameters explained above are the fundamentals for Monte Carlo simulation [36].

4.2.2 EXPERIMENT SAMPLES AND THE MEASUREMENT OF THEIR OPTICAL PROPERTIES

The samples used were porcine conjunctiva, sclera, ciliary muscle and ciliary P.E..

Conjunctiva is the thin, transparent tissue that covers the outer surface of the eye. It begins at the outer edge of the cornea, covering the visible part of the sclera, and lining the inside of the eyelids. It is nourished by tiny blood vessels that are nearly invisible to the naked eye.

Sclera is tough and opaque, serving as the eye's protective outer coat. In children, the sclera is thinner and more translucent, allowing the underlying tissue to show through and giving it a bluish cast. As we age, the sclera tends to become more yellow.

Ciliary body is the tissue for aqueous humor production. It consists of ciliary muscle and ciliary epithelium, lying behind the iris. Ciliary muscle is responsible for lens accommodation by changing the shape of the crystalline lens; ciliary epithelium is a secretion of aqueous humor, secretion and anchoring of the zonular fiber that form the suspensory ligament of the lens. Nourishment for the ciliary body comes from blood vessels.

The samples were extracted from fresh pig eyes. They were kept in the refrigerator at 4 ^{o}C before measurement. The sizes of the sample are 10 *mm*×10 *mm* for conjunctiva, 10 *mm*×10 *mm* for sclera, and 5 *mm*×4 *mm* for ciliary body. For the thickness

measurement, the samples were sandwiched between two microscope slides with minimal compression; otherwise, the absorption and scattering coefficients of the tissue will change. The thickness was measured using a micrometer. Five points in one sample were measured and the average was used.

The radiative transfer theory was applied in this work to describe the light propagation. It directly deals with power transport through the turbid medium. In this theory, the parameters for tissue optics description are absorption coefficient, scattering coefficient, and the average cosine of the scattering angle associated with single scattering phase function g. The measurement of these parameters was carried out within 48 hours postmortem. During experiment, the prepared sample was placed between the microscope slide glass and the cover slide. A UV-VIS-NIR spectrophotometer was used to measure the transmission and absorption value. The wavelengths of Argon laser (480 nm), Ti:Sapphire laser (800 nm), and YAG laser (1064 nm) were our concern in this study.

An inverse adding-doubling algorithm [89, 90] is then used to calculate the absorption coefficient and scattering coefficient. It has a high speed of numerical algorithm and has a good flexibility in anisotropic scattering and internal reflection at the boundaries. Several steps are involved in this method: (1) obtaining the reflection from the measured transmission and absorption, and take it as the measured reflection data; (1) estimating a set of optical properties of interest; (2) using the adding-doubling interactive program to calculate the reflection and transmission; (3) comparing the measured and calculated data of the reflection and transmission; (4) repeating the above steps until a match within a specified acceptance margin is reached. The optical data set, which yields a close match to the measured values of reflection and

transmission, are assumed as the optical properties of the tissue. Table 4.1 and Table 4.2 give the measured data except for the refractive index and the anisotropy factor, which were referred from reference [91]. For the ciliary P.E., because the absorption is the dominant attenuation process in the pigmented epithelium, the scattering effect was negligible and thus the scattering coefficient assumed to be zero.

Table 4.1 Thickness, Refractive Index and Anisotropy Factor of the Measured Tissue Samples

Samples	Thickness $d\ (mm)$	Refractive index n	Anisotropy factor, g
Conjunctiva	0.3	1.38	0.9
Sclera	0.72	1.41	
Ciliary Muscle	0.41	1.38	
Ciliary P.E.	0.02	1.38	

Table 4.2 Absorption Coefficient and Scattering Coefficient of the Measured Tissue Samples

Samples	Absorption coefficient $\mu_a\ (cm^{-1})$			Scattering coefficient $\mu_s\ (cm^{-1})$		
	Argon	Ti:Sapphire	YAG	Argon	Ti:Sapphire	YAG
Conjunctiva	2.0	1.1	0.72	153	92.5	73.4
Sclera	3.5	1.7	2.3	515	297	187.5
Ciliary muscle	40	21	8.15	420	501.5	573.2
Ciliary P.E	399.3	192.9	63.9	0	0	0

4.3 MONTE CARLO SIMULATION

4.3.1 MONTE CARLO INTRODUCTION

The Monte Carlo method is widely used for light transport simulation by researchers [92-96]. It was used to analyze the femtosecond laser-ocular tissue interaction process in this chapter. Generally speaking, it can be introduced as the definition in [97]: in all applications of the Monte Carlo method, a stochastic model is constructed in which the expected value of a certain random variable (or of a combination of several variables) is equivalent to the value of a physical quantity to be determined. This expected value is then estimated by the average of multiple independent samples representing the random variable introduced above. For the construction of the series of independent samples, random numbers following the distribution of the variable to be estimated are used.

Monte Carlo light propagation is rigorous yet very descriptive. At the core of Monte Carlo simulations lies a random number generator routine that forms the basis for the 'rolling the dice' probability approach in the Monte Carlo simulation. The simulation keeps track of the fraction of the total number of photons that is absorbed in each grid element, thus providing a map of spatial energy distribution. The number of photons required in a simulation depends largely on the question being asked, the precision needed, and the spatial or temporal resolution desired [98]. In this work, the simulation lends itself to investigation of optical properties of the various layers in the eye, the energy deposition will be dictated which is directly responsible for the femtosecond laser-ocular tissue interaction effect.

4.3.2 ALGORITHM

In the Monte Carlo model, photons are continuously scattered when they propagate in the tissue, until they are transmitted, absorbed, or reflected. Some assumptions were made in the simulation: firstly, the tissue is homogeneous and infinitely wide; secondly, each scattering element pattern is independent of others; thirdly, light propagation does not induce fluorescence or phosphorescence; fourthly, polarization effects are negligible.

The tissues were characterized by the parameters shown in Table 4.1 and Table 4.2. A multi-layered, cylindrically symmetric tissue model was developed to simulate transscleral irradiation of the ciliary body. The structure of the model is shown in Figure.4.2. It consists of conjunctiva, sclera, ciliary muscle and ciliary pigment epithelium (CPE). The medium at the top interface is air, and the medium on the bottom interface is vitreous humor. The vitreous humor is a thick, transparent substance that fills the centre of the eye. It is composed mainly of water. A focused laser beam was incident on the tissue from air. The light source was a Gaussian beam, with radius 0.3 mm. The photon number was 10^6 for each run. The physical quantities of interest were reflection, transmission, and absorption.

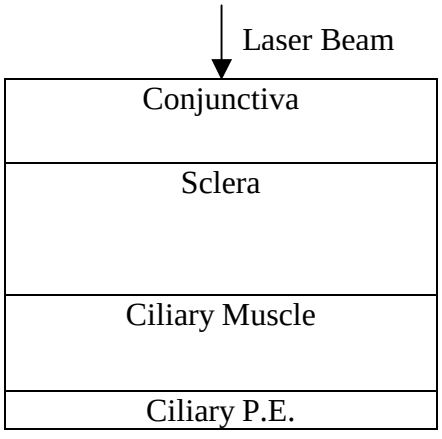

Figure 4.2 The Scheme of Multilayered Ocular Tissue Structure

A Cartesian coordinate system is used for tracing photon packets in the program. A random variable value ξ is chosen for random sampling. It has a uniform distribution over the interval (0, 1). Its cumulative distribution is

$$F_{\xi}(\xi) = \begin{cases} 0 & if \quad \xi \le 0 \\ \xi & if \quad 0 < \xi \le 1 \\ 1 & if \quad \xi > 1 \end{cases} \tag{4-3-1}$$

The photon packet is initially launched with a weight *W*. The Cartesian coordinates are used to specify the photon position:

$$\begin{aligned} \mu_x &= r \bullet x_r \\ \mu_y &= r \bullet y_r \\ \mu_z &= r \bullet z_r \end{aligned} \tag{4-3-2}$$

where, μ_x, μ_y, μ_z are the directional cosines, r is the unit vector, and x_r, y_r, z_r are unit vectors along corresponding axis.

The Monte Carlo method simulates the 'random walk' of photons in a medium that contains absorption and scattering. The method is based on a set of rules that govern the movement of a photon in tissue. The two key decisions are (1) the mean free path for a scattering or absorption event (i.e. how far does the photon travel before scattering or absorption occurs), and (2) the scattering angle (i.e. in which direction does the photon continue after the scattering event).

The mean free path is related to the step size of the photon packet. With the step size being calculated, the photon packet position can be updated:

$$\mu_t = \frac{-dP\{s \ge s'\}}{P\{s \ge s'\}ds'} \tag{4-3-3}$$

$$s_1 = \frac{-\ln(\xi)}{\mu_t} \tag{4-3-4}$$

$$\begin{aligned} xx' &= xx + \mu_x s \\ yy' &= yy + \mu_y s \\ zz' &= zz + \mu_z s \end{aligned} \tag{4-3-5}$$

Where s is the photon's free path, and s_1 is a mean free path, xx, yy, zz are the photon's Cartesian coordinates, and xx', yy', zz' are its new ones.

The scattering angle is calculated using a deflection angle $\theta \in [0, \pi)$ and an azimuthal angle $\psi \in [0, 2\pi)$. [98]

$$p(\cos\theta) = \frac{1-g^2}{2\left(1+g^2-2g\cos\theta\right)^{3/2}} \tag{4-3-6}$$

$$\cos\theta = \begin{cases} \frac{1}{2g}\left\{1+g^2-\left[\frac{1-g^2}{1-g+2g\xi}\right]^2\right\} & if \quad g > 0 \\ 2\xi - 1 & if \quad g = 0 \end{cases} \tag{4-3-7}$$

For the anisotropy factor g, a value of zero means the isotropic scattering; while a value close to 1 means a much forwarded scattering. The azimuthal angle ψ is expressed as below

$$\psi = 2\pi\xi \tag{4-3-8}$$

When the cosine of z-axis angle of the photon propagation is below 0.9999, the new direction of the propagation is:

$$\mu'_x = \frac{\sin\theta}{\sqrt{1-\mu_z^2}}\left(\mu_x\mu_z\cos\psi - \mu_y\sin\psi\right) + \mu_x\cos\theta$$
$$\mu'_y = \frac{\sin\theta}{\sqrt{1-\mu_z^2}}\left(\mu_y\mu_z\cos\psi - \mu_x\sin\psi\right) + \mu_y\cos\theta$$
$$\mu'_z = -\sin\theta\cos\psi\sqrt{1-\mu_z^2} + \mu_z\cos\theta \qquad (4\text{-}3\text{-}9)$$

When the cosine of z-axis angle of the photon propagation is above 0.9999, the new direction of the propagation is:

$$\mu'_x = \sin\theta\cos\psi$$
$$\mu'_y = \sin\theta\sin\psi$$
$$\mu'_z = \begin{cases} \cos\theta & if \quad \mu_z > 0 \\ -\cos\theta & if \quad \mu_z < 0 \end{cases} \qquad (4\text{-}3\text{-}10)$$

At a tissue boundary (where the index of refraction n changes), the photon is either reflected or it moves across the boundary in a new direction as depicted by Snell's law. Regarding reflection or transmission, the decision is made by comparing a new random variable value ζ to the reflection coefficient μ_r. if $\zeta<\mu_r$, then this particular photon reflected from the surface; otherwise the photon must have transmitted through the boundary. For the boundary at the air-tissue interface, if the photon reflects back into air, the computer is finished with this photon and a new photon is initialised.

After the photon propagates in the tissue for some time, it will be terminated by reflection, transmission, or absorption. To ensure an acceptable distribution of photon deposition and conservation of energy, a roulette technique is used. It is a random termination technique, giving the photon one chance in q of survival, with a weight of qW . When the photon weight is reduced below a threshold value W_{th}, the photon will be terminated. The roulette can be described as:

$$W = \begin{cases} qW & if \quad \xi \le 1/q \\ 0 & if \quad \xi > 1/q \end{cases} \tag{4-3-11}$$

Once the photon propagation is terminated, a new packet is launched into the tissue, and follows the same procedure. The program frame is shown in Figure 4.3.

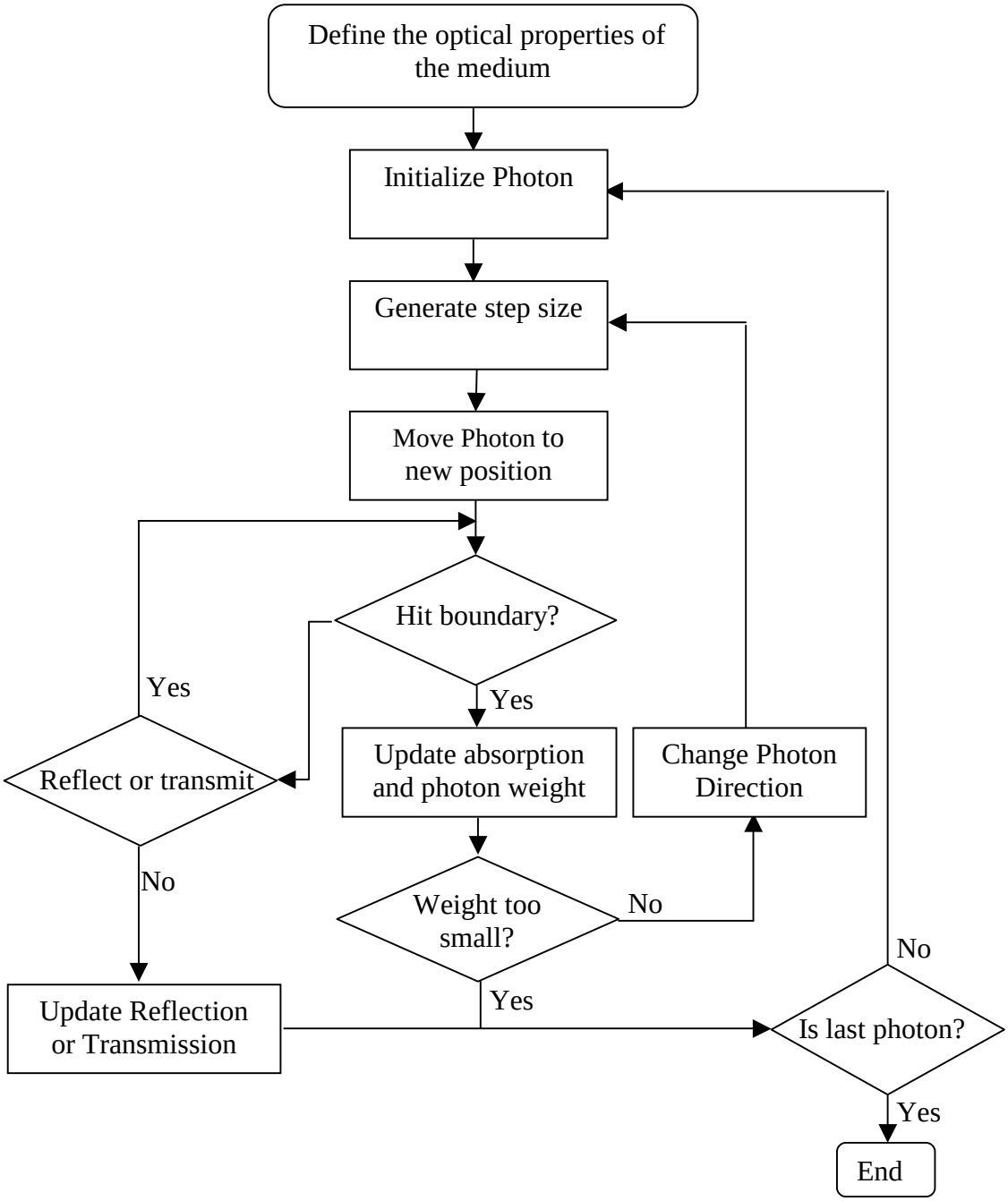

Figure 4.3 Monte Carlo Simulation Program Flow Chart

4.3.3 SIMULATION RESULT AND ANALYSIS

Figure 4.4 shows the contour plot of the fluence rate. Figure 4.4 (a) is for Argon, Figure 4.4 (b) is for Ti:Sapphire, and Figure 4.4 (c) is for YAG. Five levels of fluence rate were illuminated, and they were 5 W/mm^2, 4 W/mm^2, 3 W/mm^2, 2 W/mm^2, 1 W/mm^2, and 0.5 W/mm^2 from high to low. The comparison of the three contour plots shows that YAG laser has a lower radial spread and has a higher penetration in z direction.

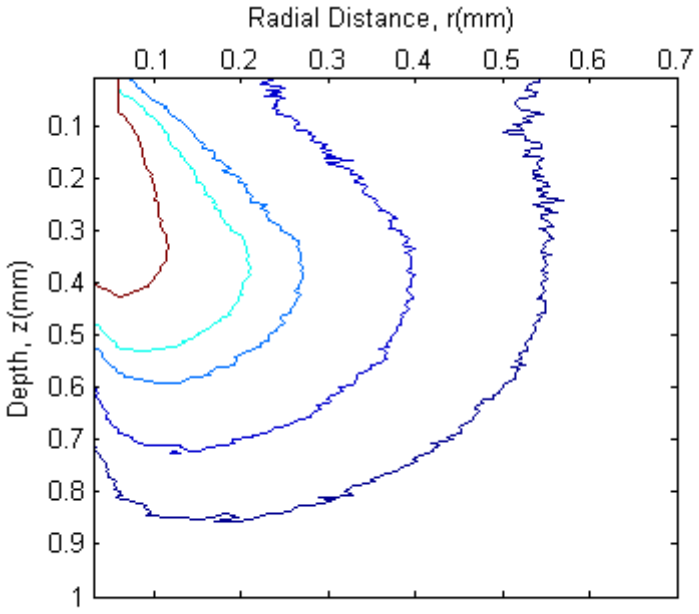

Figure 4.4 (a) Fluence Rate Contour Plot with Argon Laser Propagation

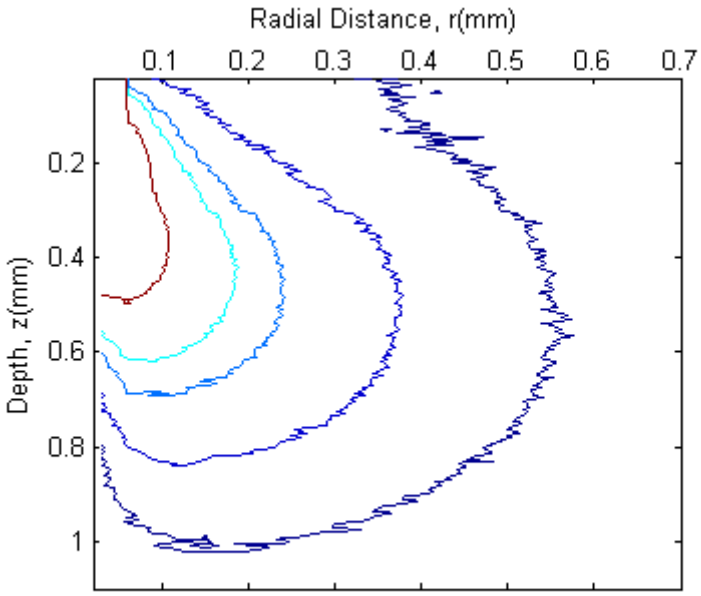

Figure 4.4 (b) Fluence Rate Contour Plot With Ti:Sapphire Laser Propagation

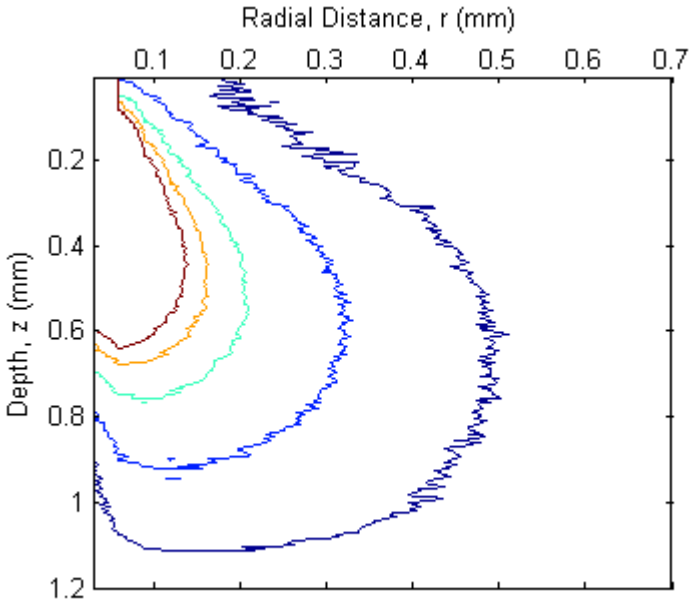

Figure 4.4 (c) Fluence Rate Contour Plot with YAG Laser Propagation

Figure 4.4 Fluence Rate Contour Plot During Light Propagation at Different Wavelengths

Figure 4.5 shows the comparison of the fluence rate changes in the *z* direction with radius r = 0.05 mm. Due to back scattering, the internal fluence rate within the tissue is slightly higher than that at the conjunctiva surface. The fluence decreases evidently

with the light propagation in the depth (in the z direction). It can be seen that the fluence rate of Argon laser decreases quickly, while the Ti:Sapphire has a closer trend with YAG laser. These results can be expected from Table 4.2, in which the optical coefficients show a more penetrating character of the NIR wavelengths (Ti:Sapphire and Nd:YAG) than that of the Argon wavelength. In addition, it can be seen that the Fluence Rate of Ti:Sapphire was higher than that of Argon and YAG. It means that there will be no much photon density loss by scattering at 800nm. It shows the advantage of Ti:Sapphire laser during propagation in Conjunctiva and Sclera.

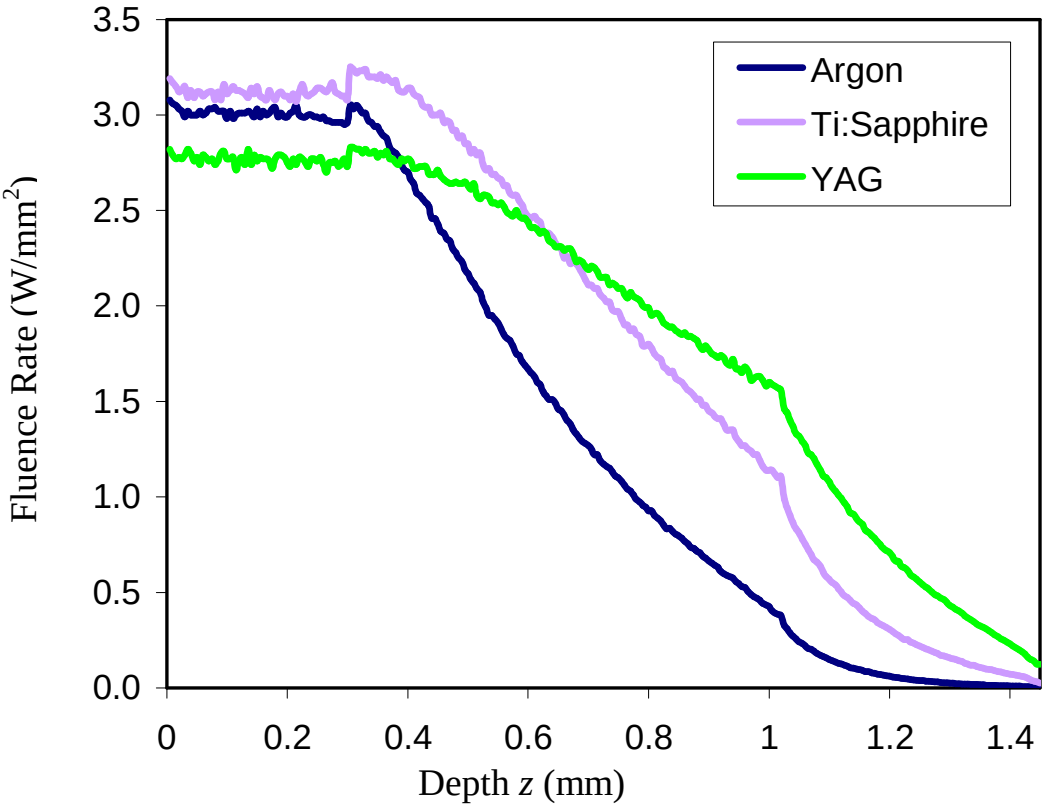

Figure 4.5 Fluence Rate Along z Direction at *r* = 0.05mm

The comparison of total reflection by Argon, Ti:Sapphire and YAG is shown in Figure 4.6. From this Figure, it is clear that during light propagation in the multi-layer turbid ocular tissue, the reflection at 488 nm is the largest, and that at 1064 nm is the

smallest. The reflection value by Ti:Sapphire is higher but close to YAG. Lower reflection value will be helpful during laser surgery.

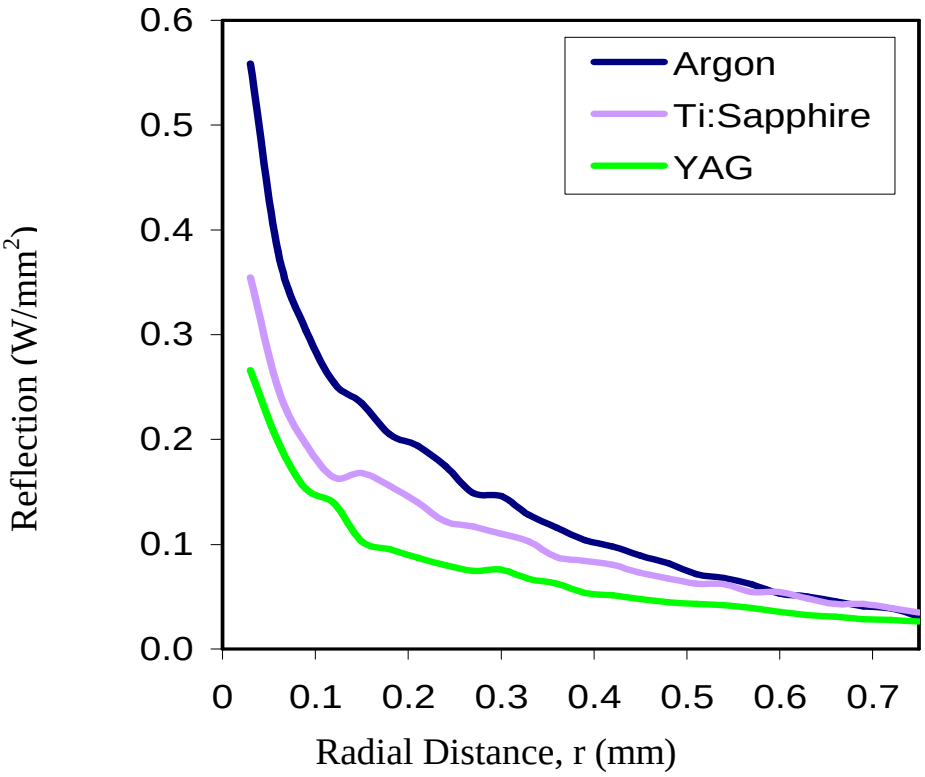

Figure 4.6 Reflection as a Function of Radial Distance

The fractions of absorption, reflection and transmission were calculated in the simulation program, and the data are listed in Table 4.3.

Table 4.3 Calculated Fractions of Absorption, Reflection and Transmission for the Multilayered Ocular Tissue Structure

Laser	Wavelength (nm)	Absorption	Reflection	Transmission
Argon	488	0.705754	0.327362	0.001282
Ti:Sapphire	800	0.677095	0.280998	0.016305
YAG	1064	0.609311	0.234131	0.070955

From this Table, the effect of different wavelengths on the light propagation in ocular tissue can be compared. The absorption fraction of Ti:Sapphire is 0.677099, and that of YAG is 0.609311. It means that Ti:Sapphire has a higher probability of photon absorption, although it has a lower penetrating nature compared to YAG laser. Therefore it is has an advantage over YAG laser during laser-ocular tissue interaction.

4.4 SUMMARY

To verify the feasibility of Ti:Sapphire femtosecond laser in glaucoma treatment, light propagation in a multilayered ocular tissue structure was studied through Monte Carlo simulation.

The optical properties of porcine ocular tissues were measured, including conjunctiva, sclera, ciliary muscle, and ciliary P.E.. A multilayered model was established and the light propagation was investigated at three different lasers (Argon, Ti:Sapphire, and YAG). The contour of fluence rate, the fluence rate change in the z direction, and the reflection in the radial direction were investigated. The fractions of absorption, reflection, and transmission were calculated. The results show that among these three lasers, Argon laser has the largest radial expansion and has the smallest penetration depth. Inversely, YAG laser has a smallest radial expansion and has a largest penetrating nature, which can limit the collateral damage to the adjacent tissue, and is helpful for subsurface surgery. Compared to YAG laser, Ti:Sapphire shows a higher possibility of photon absorption, thus it is easier for the optical breakdown occurring in the femtosecond region. The results in this chapter are essential for further study on femtosecond laser application in cyclophotocoagulation.

CHAPTER FIVE

IN-VITRO EXPERIMENTATION ON FEMTOSECOND LASER OCULAR TISSUE INTERACTION

5.1 INTRODUCTION

Besides theoretical study and numerical simulation, experimental investigation is essential for a novel setup development in laser glaucoma surgery. There are a wide range of variables that affect the laser-tissue interaction process, including wavelength, pulse duration, numerical aperture, pulse intensity, and pulse numbers. In this chapter, the laser parameters and their effects on the ablation process in tissue are addressed. The optical breakdown threshold and the steady state ablation are studied through in-vitro experiment.

5.2 EXPERIMENT SETUP AND TISSUE SAMPLES

The in-vitro experiment setup is shown in Figure 5.1. The laser system consists of an oscillator and an amplifier. The pulses from the amplifier are at a central wavelength of 800 nm, and at a repetition rate of 1000 Hz. These pulses are amplified by means of chirped pulse amplification in a Ti:Sapphire regenerative amplifier, which is pumped by an Nd:YLF laser. The measured pulse duration of the system is 150 fs.

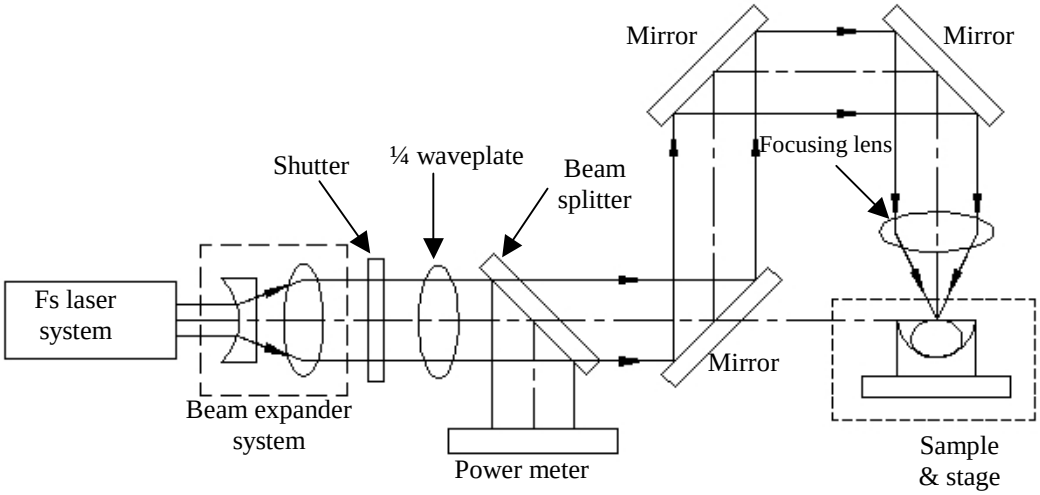

Figure 5.1 In-Vitro Experiment Setup with a Femtosecond Laser System

The optical setup included a beam expander, quarter waveplate, shutter, beam splitter, mirrors, and objective lens. The beam expander was used to obtain a smaller spot size. The shutter was used to determine the exposure time of the pulses, mirrors were used to change the laser direction, and the focusing lens (objective) was utilized to focus the collimated beam into the sample. To keep pig eyes in a fixed position, a holder unit, which consisted of a half-spherical-space vessel, was used, and integrated into the 3-axis stage. During the experiment, the sample was put in the vessel, and was covered by a piece of cotton gauze. An elastic ring then bound around the cotton gauze to keep the sample in position and to prevent displacement of the sample during the experiment. An opening was then made on the cotton gauze to expose the anterior segment of the eye. As the iris area spanned over a working area of 10 mm in diameter, 3D translation of the laser focus could be performed within a 4 mm depth and over the working field of 10 mm diameter. In the experiment, the computer-controlled system guided the amplified pulses towards the treated pig eyes, and pre-set the output power and exposure time during processing as shown in Figure 5.2.

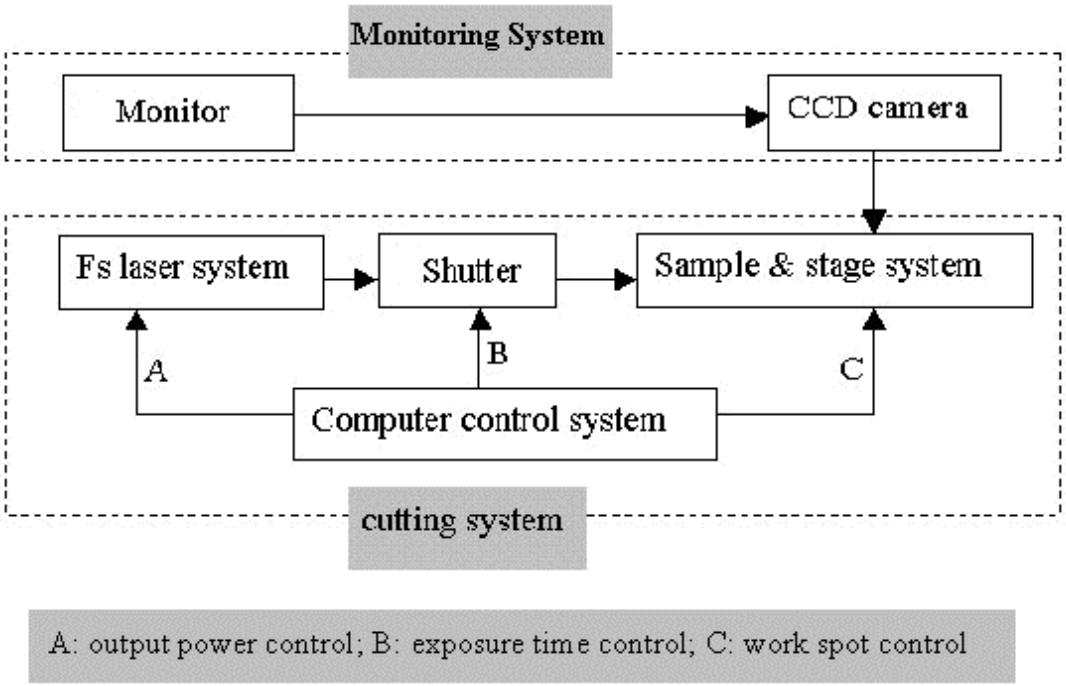

Figure 5.2 In-Vitro Experiment Control System

The pig eyes used in this study were brown in color. They were obtained from pigs slaughtered at a local abattoir. The eyes would otherwise have normally been discarded. The post-mortem eyes were stored in a refrigerator at 4^0 C, and they were used for in-vitro experiments within one week after enuclation. Following the experiments, the results were analyzed using an optical microscope and a scanning electronic microscope (SEM).

5.3 LASER PARAMETERS

5.3.1 WAVE LENGTH

The wavelength affects the scattering of the light during its propagation in the tissue. When the wavelength is much larger than the particles' size, it is named Rayleigh scattering, and it is backscattering. When the wavelength is much less than the particle's size, it is named Mie scattering, and it is forward scattering. Generally

speaking, the amount of scattering will decrease with increasing wavelength. However, the absorption of the laser light will not always have a linear relationship with the wavelength (see Table 4.2 in Chapter 4). As for the femtosecond laser system in our experiment, the wavelength was fixed at 800 nm.

5.3.2 PULSE DURATION

In laser surgery, strong mechanical side effects such as considerable bubble formation inside the tissue are not acceptable. With pulse duration decreasing, pulse energy will decrease, and therefore the extent of side effects will be reduced as well. The effect of pulse duration on the laser tissue interaction has been theoretically studied in chapter 3. Some experimental results by other researchers are shown in Table 5.1. The experiment was performed in distilled water. It gives us the effect of pulse duration on threshold intensity.

Table 5.1 Laser Parameters and Corresponding Pulse Energy Thresholds from the Nanosecond Region to the Femtosecond Region [83]

Pulse duration	Wavelength nm	Focusing angle ^{o}C	Measured spot diameter/μm	I_{th} x10^{11} W cm^{-2}	E_{th} J cm^{-2}
76 ns	750	19	20	0.23	1750
6 ns	1064	32	5.5	0.66	398
6 ns	1064	22	7.6	0.47	284
6 ns	1064	8	11.5	0.79	472
6 ns	1064	5.4	14.6	1.10	648
30 ns	1064	28	4.6	4.6	13.8
30 ns	1064	22	4.7	4.5	13.6
30 ns	1064	14	5.8	3.0	9.0
30 ns	1064	8.5	9.6	4.5	13.6
30 ns	1064	4	19.5	3.7	11.1
60 ns	532	13	5.6	2.8	16.8
3 ps	580	16	5.0	8.5	2.6
300 fs	580	16	5.0	47.6	1.4
100 fs	580	16	4.4	111.0	1.1

From both our simulation result in Chapter 3 and that in Table 5.1, it can be concluded that with pulse duration decreases, pulse energy threshold for optical breakdown can be evidently reduced. Therefore the side effect during the laser tissue interaction may be limited within an acceptable extent.

5.3.3 NUMERICAL APERTURE

The term used commonly in defining a focusing angle θ_f is numerical aperture NA. Numerical aperture is the sine of the angle made by the marginal ray with the optical axis (see Figure 5.3).

$$NA = i \sin \theta_f = i \frac{\phi}{2f} \qquad (5\text{-}3\text{-}1)$$

Where $i = \frac{n_2}{n_1}$, n_1, n_2 are air index and work medium index respectively. f is the focal length of the lens, and ϕ is the lens' effective diameter.

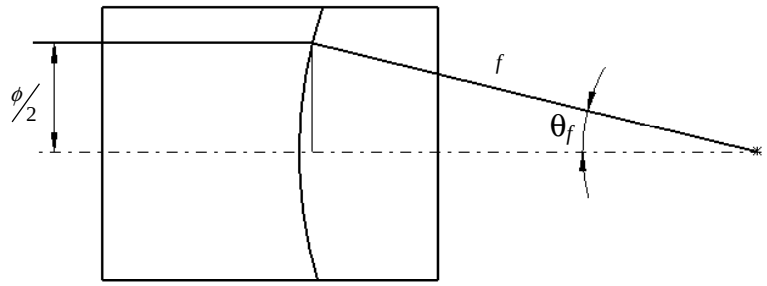

Figure 5.3 Focusing Angle Illumination

At certain energy, the plasma can grow into the cone of the laser beam until it reaches the cross section for which $I = I_{th}$. This cross section is the same regardless of the

focusing angle but the distance between the laser focus and the cross section is larger for smaller angles. Therefore, for smaller angles, the volume of the cone is larger, and the energy density less. This results in a smaller rate for multiphoton absorption, and thus a smaller ablation rate. At large focusing angles, short and highly absorbing plasmas are achieved. It allows well-localized energy deposition at a low breakdown threshold. However, in the medium, the rays which transverse the cone edges go a longer way (ray *a* in Figure 5.4) than the central ones (ray *b* in Figure 5.4). For a focused laser beam with large focusing angle, the rays along the cone edges are scattered to a large extent, and few of them reach the laser focusing point. In addition, large focusing angles are also associated with conversion efficiency into mechanical energy, which has a large potential for mechanically induced side effects. Thus the numerical aperture should be an optimized value rather an extreme one.

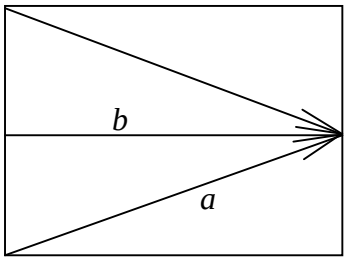

Figure 5.4 Focused Rays Traveling Distance

The relationship between focusing angle and pulse energy was studied using five different numerical aperture parameters, namely 0.16, 0.25, 0.5, 0.65, and 0.85. The beam was focused onto the fresh cornea. The interaction result was observed by OMIS optical microscope. The assessment criterion of this experiment is the observable vaporization on the cornea using the same laser parameters except different Numerical Aperture (NA). Figure 5.5 shows the vaporization occurring in cornea observed during

the experiment with $NA = 0.65$. By recording the output power for each processing, the corresponding pulse energy can be calculated.

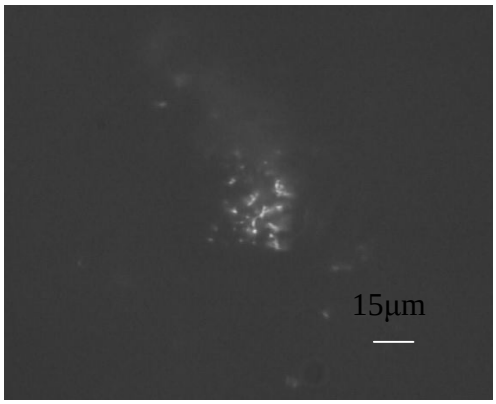

Figure 5.5 The Optical Breakdown in Cornea, *NA* = 0.65

Figure 5.6 shows the relationship between the pulse energy needed for optical breakdown and numerical aperture. From Figure 5.6, we know that the pulse energy needed for optical breakdown decreases with increasing numerical aperture value. For example, when NA was 0.16, the pulse energy to produce visible breakdown is about 750 μJ. When NA increased to 0.85, the pulse energy needed is reduced (165 μJ). Since a high NA value means high focusing angle, it also results in a high laser pulse density. Thus, according to the experimental results shown in Figure 5.6, it can be concluded that the higher NA objective has an advantage to produce optical breakdown compared to lower NA objective. However, with reference to the literature, it should also be clear that too high a NA objective results in significant side effects. In the experiment setup design, an appropriate NA objective is very important for obtaining good experimental results. NA=0.65 and NA=0.85 were used in this work.

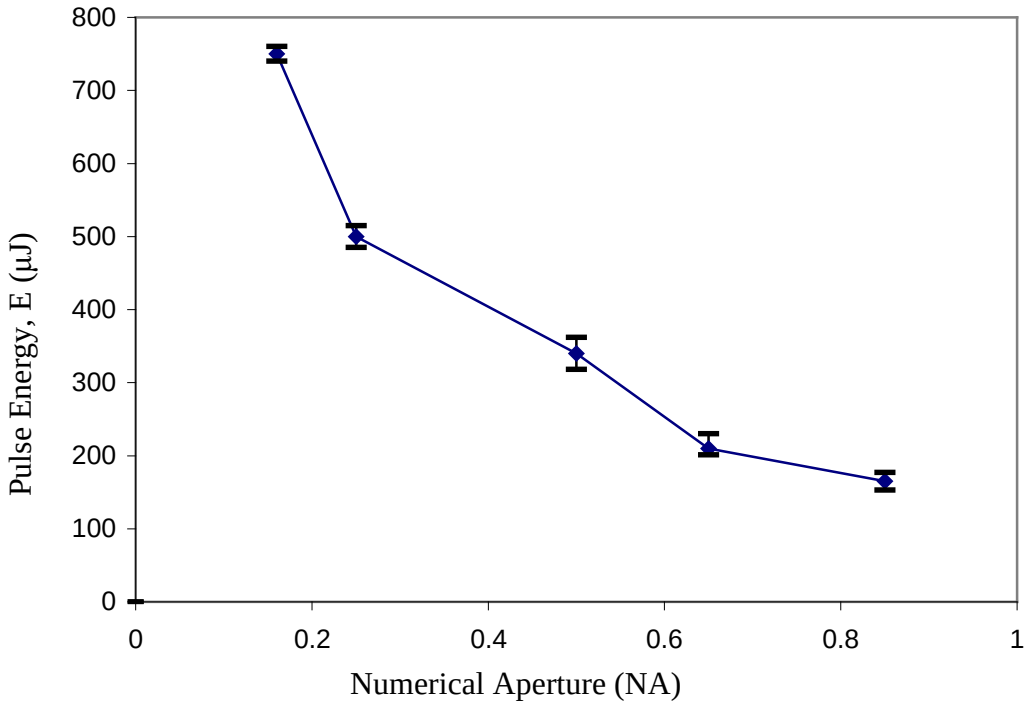

Figure 5.6 Numerical Aperture & Pulse Energy Needed for Optical Breakdown

5.3.4 PULSE INTENSITY

Light propagation in a material is described by Maxwell's equation. When the electric field strength is small, the polarization vector P is a linear function of electric field strength E. At high electric field strengths, the linear relationship between P and E is no long valid. The dependence of the polarization on the field becomes nonlinear. The polarization is generally described as a power series of the electric field as below. [99]

$$P_p = P_p^{(1)} + P_p^{(2)} + P_p^{(3)} + \ldots = \varepsilon_0\left(\tilde{\chi}^{(1)}E + \tilde{\chi}^{(2)}EE + \tilde{\chi}^{(3)}EEE + \ldots\right) \qquad (5\text{-}3\text{-}2)$$

For the ocular tissue, the polarization vectors that are even powers of E have to vanish in order to satisfy symmetry requirements. The above equation reduces to

$$P_p = P_p^{(1)} + P_p^{(2)} + P_p^{(3)} + \ldots = \varepsilon_0\left(\tilde{\chi}^{(1)}E + \tilde{\chi}^{(3)}EEE + \ldots\right) \qquad (5\text{-}3\text{-}3)$$

Where, ε_0 is the permittivity of free space; $\tilde{\chi}^{(1)}$ is a material dependent parameter. In general, $\tilde{\chi}^{(1)}$ is nonlinear, and relates the complex amplitudes of the electric field and polarization. The electric field strength is decided by the laser pulse intensity. The nonlinear effect can easily occur due to the high pulse intensity in the femtosecond region. When the pulse intensity is higher than the optical breakdown threshold, the material will be modified or even effectively ablated.

The laser pulse intensity depends on the pulse duration, repetition rate, and output power. Since the repetition rate and the pulse duration were fixed in our laser system, laser pulse intensity was directly related to the output power value in our experiment.

In the experiments, the spot size was 15 μm, the Numerical Aperture was 0.65, and the output power was varied from 0 to 150 mW. The sample was fresh pig eye, and the beam was focused into the iris. The results were observed by SEM.

The ablation results by different output power values are shown in Figure 5.7. The statistical analysis of the result is shown in Figure 5.8. From Figures 5.7 and 5.8, it is known that a certain output power is needed for ablation. The power 100 mW is able to create a hole without side effects. The power 140 mW is more effective than 100 mW, while there is a risk to damage the adjacent tissue. When the output power is larger than 140 mW, the thermal damage can be clearly seen.

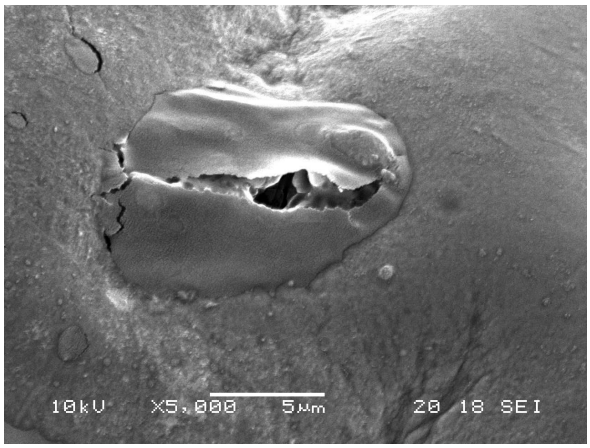

Figure 5.7 (a) P = 80 mW, t = 0.1 s, d ≈10 μm

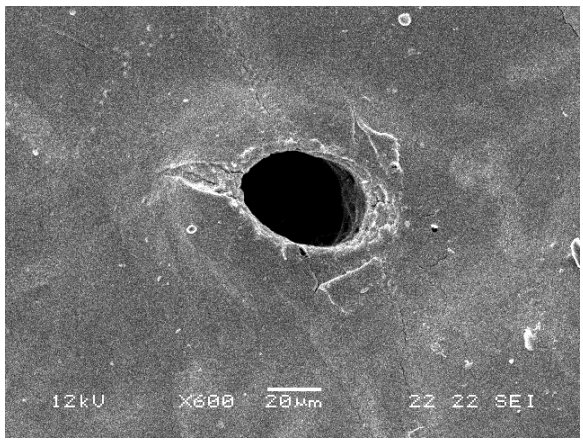

Figure 5.7 (b) P = 100 mW, t = 0.1 s, d ≈ 50 μm

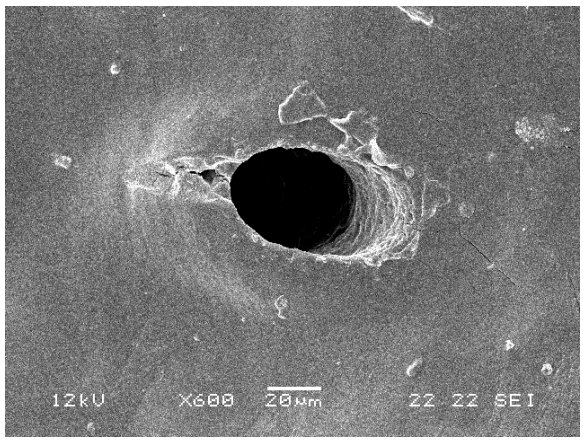

Figure 5.7 (c) P = 120 mW, t = 0.1 s, d ≈ 55 μm

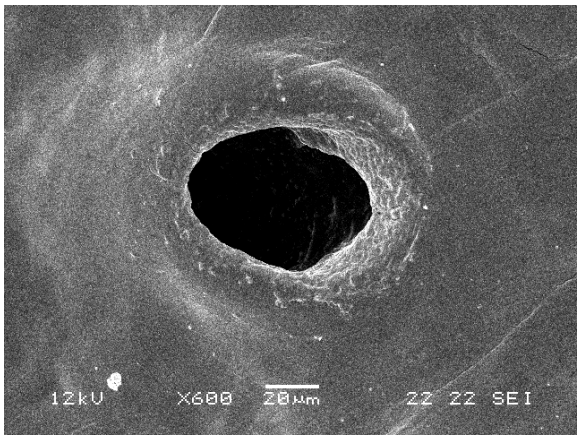

Figure 5.7 (d) P = 140 mW, t = 0.1 s, d ≈ 60 µm

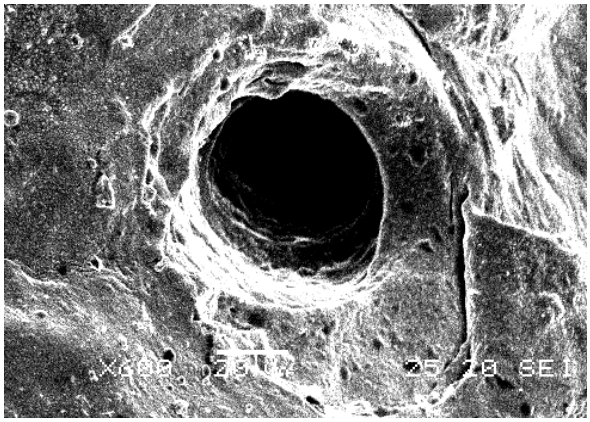

Figure 5.7 (e) P=160 mW, t=0.1 s, d ≈ 90 µm

Figure 5.7 Output Power & Cutting Effect Relationship Experiment Result

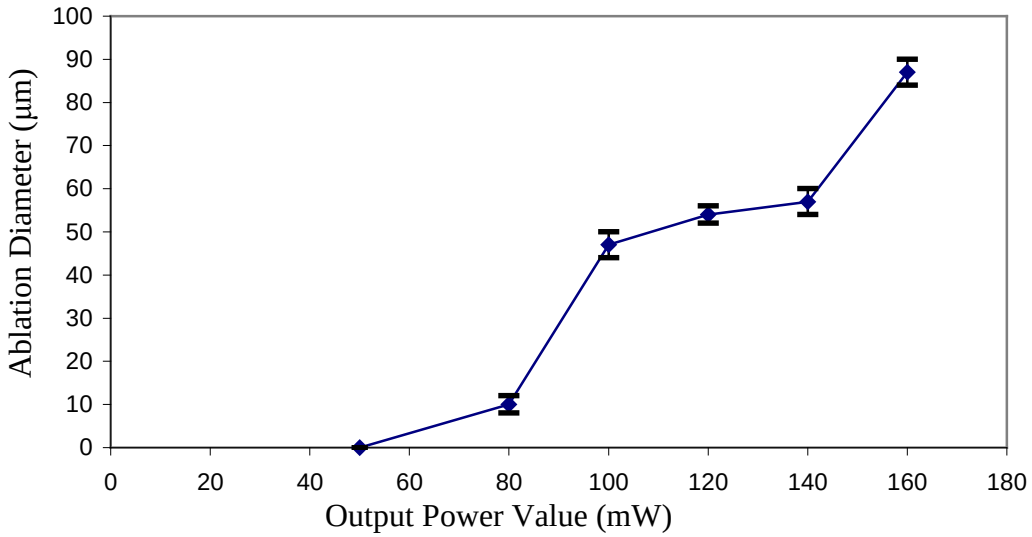

Figure 5.8 The Effect of Output Power on Ablation Diameter

5.3.5 PULSE NUMBERS

Laser irradiance duration is also an important parameter in ophthalmic microsurgery. It should be appropriately decided. Here, it is studied by investigating the relationship between ablation width and scanning speed. High scanning speed means a shorter exposure time for given processing parameters. In other words, higher scanning speed results in less laser pulse spots depositing at one position. Thus, the scanning speed can be used to study the relationship between exposure time and ablation result. Figure 5.9 shows the treated experiment sample measured by SEM.

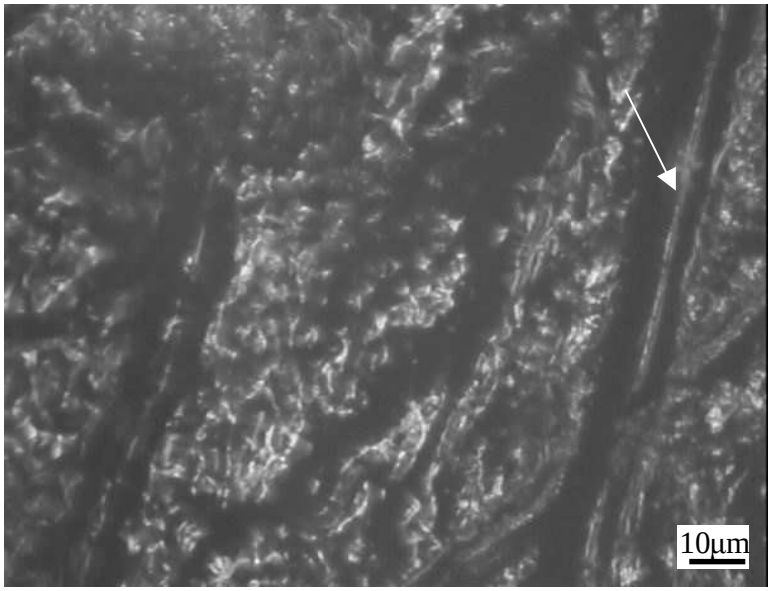

Figure 5.9 Ablation on Iris with Scanning Speed at 0.3 mm/s

Figure 5.10 shows the statistical analysis of the experiment result. From Figure 5.10, it is clear that higher scanning speed can obtain better localized processing. If the laser exposure time at one specific spot is too long, the deposited energy will result in temperature increase, subsequently decreasing the processing accuracy, and the damage will extend beyond the expected region.

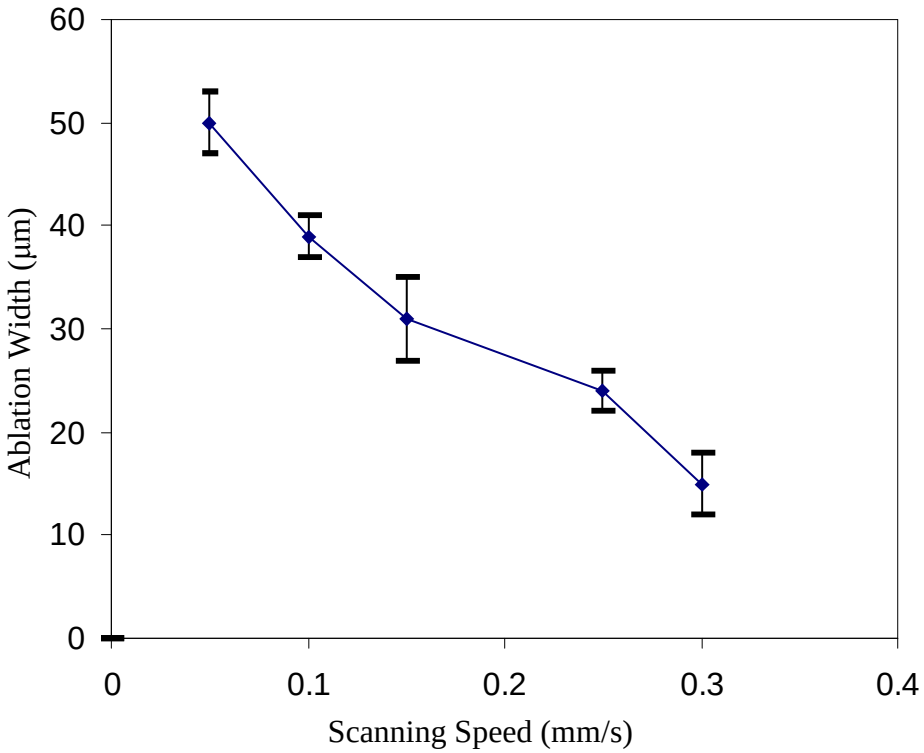

Figure 5.10 The Effect of Scanning Speed on Ablation Width

5.4 IN-VITRO EXPERIMENTATION FOR FEMTOSECOND LASER IRIDOTOMY

Currently the Q-switched Nd:YAG laser and the Argon laser are mostly used for glaucoma treatment. In Europe, the Nd:YAG laser is much more often used than the Argon laser and this is because of the pigmentation of the iris. Europeans have blue and green eyes. In Asia, such as Singapore, people normally have brown eyes, which absorb the Argon laser quite well because of the presence of melanin. In other words, a brown iris can take a considerable laser power and produce a hole [100]. So the Argon laser is normally used in the laser iridotomy for brown iris. In this chapter, the study focused on the potential of femtosecond laser in laser iridotomy. The pig eyes used in

this study were brown in color. The laser beam was focused inside the pig eye. The desired target was the pig iris. The experiment setup shown in Figure 5.1 was used for this experiment. The Numerical Aperture of the focusing lens was 0.65, and the scanning speed was 0.3 mm/s.

5.4.1 ABLATION THRESHOLD INVESTIGATION

The occurrence of optical breakdown can be confirmed through observing a visible vaporization signature on the tissue. When the laser pulse begins to produce optical breakdown and the material is ablated from the tissue, the corresponding laser pulse intensity is defined as the ablation threshold. The pulse intensity is calculated using the corresponding measured output power.

$$I_{th} = \frac{P}{f \cdot \tau_p \cdot A} \qquad (5\text{-}4\text{-}1)$$

Where P is the measured output power, f is the repetition rate, τ_p is the pulse duration of the laser system, and A is the beam spot area at the focal point.

To determine the ablation threshold, a probability plotting method was used. The experiment was repeated for n=10 runs at each power value near the optical breakdown, and after one set of measurement (10-runs measurement at one point) was finished, the power value was increased, and a new run was carried out. In each run, the frequency that the optical breakdown observed was recorded as r. The probability P is expressed as p=r/n. The experiment was stopped when r=n. Each data point is an average of N=4 times of experiment.

For a certain probability, the upper and lower limits show the measurement error. The corresponding laser pulse intensity at 50% probability of ablation point is defined as the ablation threshold. From Figure 5.11, it is known that the threshold intensity of iris ablation is about 1.7×10^{14} W/cm^2. The corresponding output power is about 90 mW; this result is much lower than the output power in the current Argon laser iridoplasty surgery setup, the minimal output power value of which for laser surgery is about 200 mW [101]. When the power value decreases, there is a possibility to reduce the pulse energy. This result agrees with the theoretical prediction in Chapter 3, that when the pulse duration decreases, the pulse energy needed for optical breakdown will decrease, and the thermal damage will also be reduced. At the same time, the experiment result could vary with water evaporation from the iris tissue during the ablation process.

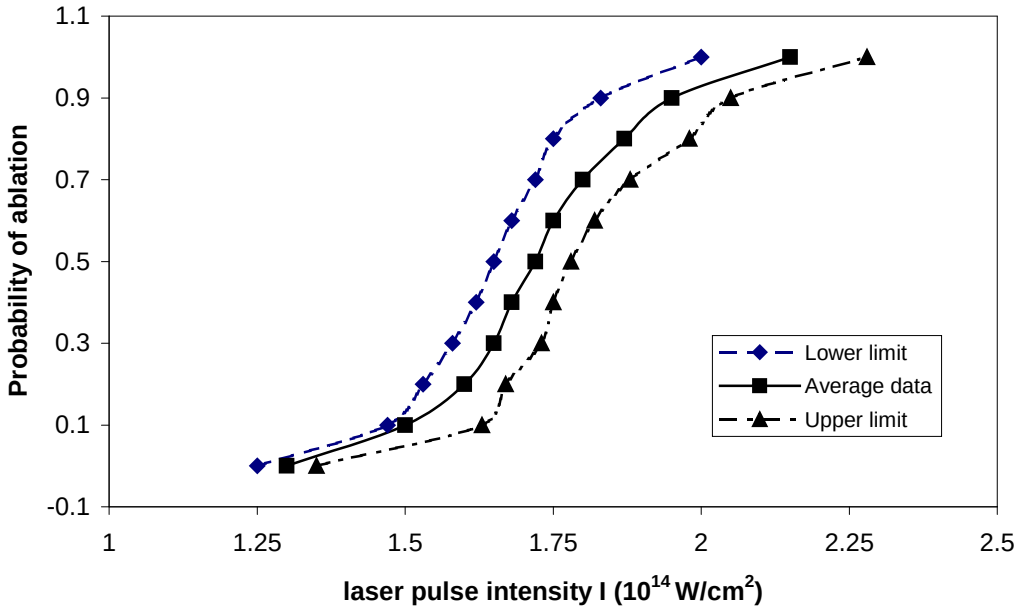

Figure 5.11 Probability Measurement of Pulse Intensity Threshold during Femtosecond Processing in Iris

5.4.2 STEADY STATE ABLATION

During the steady-state ablation, a specific amount of energy must be supplied to the tissue to obtain the incision. Since the optical coefficients of the tissue determines the spatial distribution of the energy, a certain exposure time is needed to get a desired size and depth, and a minimal laser pulse intensity is necessary for a given ablation threshold to be reached.

In this experiment, 50 μm to 90 μm diameter holes were drilled on in-vitro iris. This was to investigate the total energy needed for a certain ablation. A computer program was developed using Labview™ to obtain a circular ablation shape. The diameter of each set was 50, 60, 70, 80, and 90 μm respectively. For each set, five holes were drilled for statistical analysis on the ablation results. Figure 5.12 represents a hole drilled on iris. It is similar to the clinic-ablated hole during laser iridotomy surgery.

Figure 5.12 A Hole Drilled on In-vitro Pig Iris

In Figure 5.13, it can be seen that the relationship between the ablation diameters and deposited energy was almost linear. The larger the ablation area, the more energy was needed. For example, to ablate a 50 μm-diameter hole, 4.1 mJ energy was needed, while for a 90 μm-diameter hole, the energy of 8.4 mJ was needed.

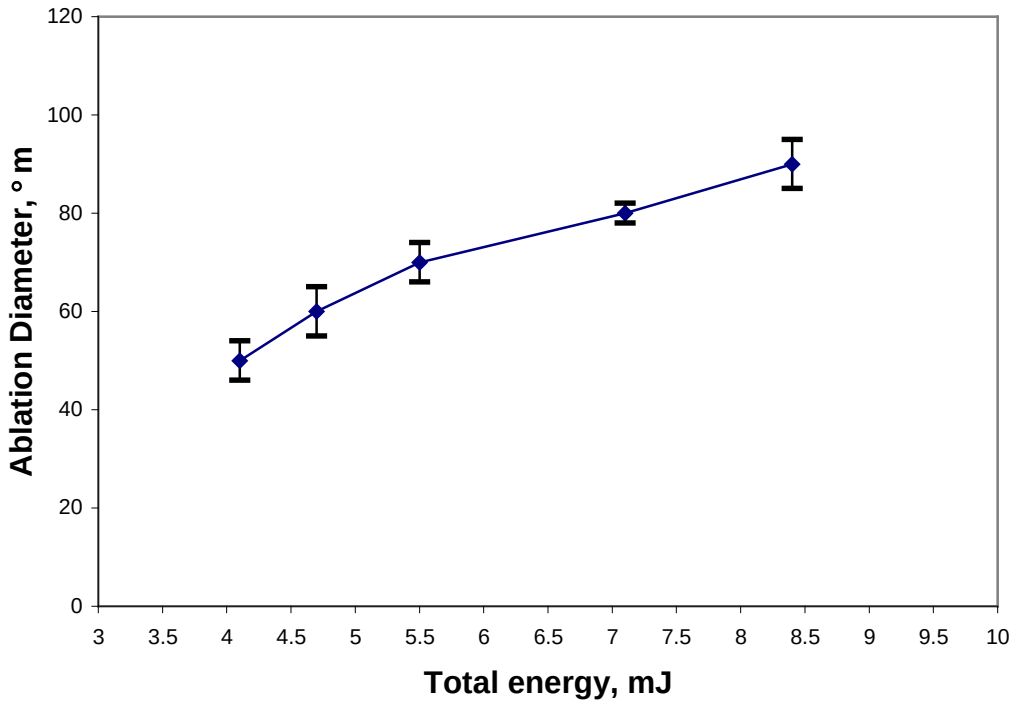

Figure 5.13 Steady State Ablation Diameters vs. Laser Total Energy

5.5 SUMMARY

In order to validate the feasibility of femtosecond laser application in glaucoma treatment, the key laser parameters for tissue ablation were investigated, and an in-vitro experiment study on ablation threshold and steady state ablation was carried out.

The wavelength affects the scattering of the light during its propagation in the tissue. With wavelength increasing, the amount of scattering decreases. The absorption of the laser light does not always have a linear relationship with the wavelength.

Pulse duration has a significant effect on the optical breakdown threshold. With pulse duration decreasing, pulse energy threshold for optical breakdown can be reduced. Therefore the side effects during the laser tissue interaction may be limited to within an acceptable range.

Numerical aperture (NA) directly affects the energy density during laser processing. A smaller NA results in a smaller rate of multiphoton absorption, and thus a smaller ablation rate. A larger NA allows well-localized energy deposition at a low breakdown threshold. Meanwhile, large NA is also associated with conversion efficiency into mechanical energy, which has a potential for mechanically induced side effects.

The laser pulse intensity determines the electric field strength. The nonlinear effect can easily occur due to the high pulse intensity in the femtosecond region. When the pulse intensity is higher than the optical breakdown threshold I_{th}, selected tissue can be removed. The laser pulse intensity depends on the output power since the pulse duration and the repetition rate of our laser system are pre-set. The effect of output power on the tissue processing result was investigated.

As for pulse numbers, it was observed that a higher scanning speed could obtain better localized processing. Low scanning speed may result in thermal damage beyond the expected region. The scanning speed of 0.3 mm/s was suitable in the in-vitro experiment study.

The ablation threshold in pig iris was studied. Using a probability plotting method, the laser pulse intensity at 50% probability of ablation point was defined as the ablation threshold. From our experimental data, it is known that the threshold intensity of iris ablation was about 1.7×10^{14} W/cm^2. The result shows advantages over the current Argon Laser Iridoplasty surgery setup.

For steady-state ablation, certain amounts of energy and exposure time are needed. Minimal laser pulse intensity is necessary to reach the ablation threshold. In our in-vitro experimentation, a 50 μm-diameter hole could be obtained with 4.1 mJ energy, and for a 90 μm-diameter hole, the energy of 8.4 mJ was needed.

CHAPTER SIX

NANO JOULE PULSE ENERGY PROCESSING WITH A FEMTOSECOND OSCILLATOR

6.1 INTRODUCTION

To date, most studies on femtosecond laser application in ophthalmology have used a femtosecond laser system with amplifier equipment (named as femtosecond amplifier in this chapter). Although this type of the femtosecond laser system shows great advantages over long pulse lasers, due to the complicated construction of its amplifier, the cost of the femtosecond laser source is high. In addition, since micro Joule pulses are used in these procedures, bubble formation and self focusing during optical breakdown may cause certain intra tissue damage. An alternative configuration of the femtosecond laser without the amplifier equipment (named as femtosecond oscillator in this chapter) has attracted researchers' interest and has been studied in the field of ophthalmology application [102]. In this chapter, a femtosecond oscillator was used to investigate the nano Joule processing in ocular tissues. Firstly, the pulse intensity thresholds of these two laser sources were investigated and the results were compared. Then the nonlinear propagation of the femtosecond pulses in the ocular tissues was studied. The results show a promising potential of femtosecond oscillator application in ophthalmology.

6.2 PULSE INTENSITY THRESHOLD VALIDATION WITH AND WITHOUT CHIRPED PULSE AMPLIFIER

6.2.1 LASER SOURCES

Two laser sources were used for the measurement of femtosecond pulse intensity threshold in water. They were the femtosecond amplifier and the femtosecond oscillator.

The amplifier used in this experiment is CPA-2001 (Clark-MXR, Inc). It is designed to amplify short pulses by a factor of about 10^5 with high repetition rate. It consists of a pulse stretcher, a regenerative amplifier pumped by a Nd:YLF laser and a compressor. This system is based on the so-called "Chirped Pulse Amplification" (CPA), which is shown in Figure 6.1.

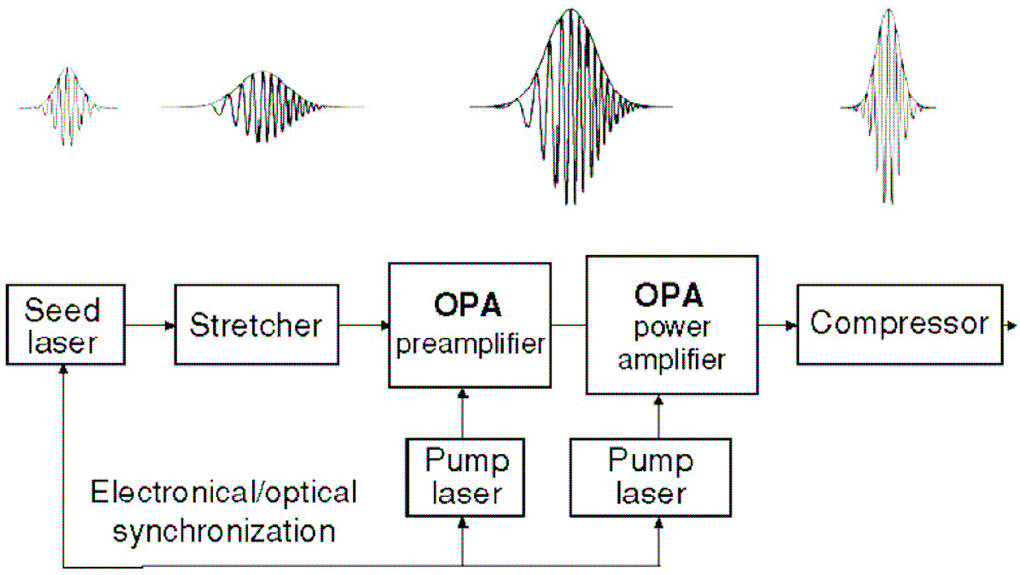

Figure 6.1 Chirped Pulse Amplification Principle [103]

CPA is the technique to amplify short pulses in solid state materials. A pulse stretcher is to stretch the pulse by a factor 1000-5000 (depending on the stretcher configuration and the spectrum of the pulses at the output of the oscillator) in order to reduce its peak power. The pulse can then be amplified safely in one or a series of amplifiers. It is finally compressed back to duration as close as possible to its initial value. Due to its complicated construction, its cost is very high.

The other laser source is a femtosecond oscillator (model 900-B Mira). Ti:Sapphire is used as the gain medium. Kerr Lens Modelocking (KLM) technique is used to modelock the Mira laser. The optical cavity is specifically designed to utilize changes in the spatial profile of the beam produced by self-focusing from the optical Kerr effect. This self-focusing results in higher round trip gain in the modelocked versus CW operation due to an increased overlap between the pumped gain profile and the circulating cavity mode. An aperture is placed at a position within the cavity to produce lower round trip loss in the mode-locked versus CW operation. Group velocity dispersion compensation is used to produce a 200 fs pulse duration. The wavelength used in this experiment is 800 nm. The repetition rate is 76 MHz [104].

6.2.2 EXPERIMENTAL SETUP

The optical setup designed to measure laser-induced breakdown threshold is shown in Figure 6.2. It was used to investigate the advantage of a femtosecond oscillator over a femtosecond amplifier in biological applications. In addition, the measured pulse energy threshold results were used to validate the predicted value by simulation in chapter 3. The filter was used to adjust the output power; therefore the power into the

beam splitter could continuously change. Detector A was used to record the power into the sample which was contained in a cuvette. Water was used as the sample to model ocular media in this experiment. Pulses were focused into the cuvette by lens 1 (an objective Lens, NA=0.85). Power out of the cuvette was re-collimated by Lens 2 ($f = 50\ mm$), and then monitored by detector B. The values in detectors A and B were simultaneously recorded in the computer. Laser-induced optical breakdown was observed by imaging the minimal observable vaporization with a long working distance objective and CCD camera. The Mirror in front of the CCD was used to reflect the light which was at 800 nm wavelength.

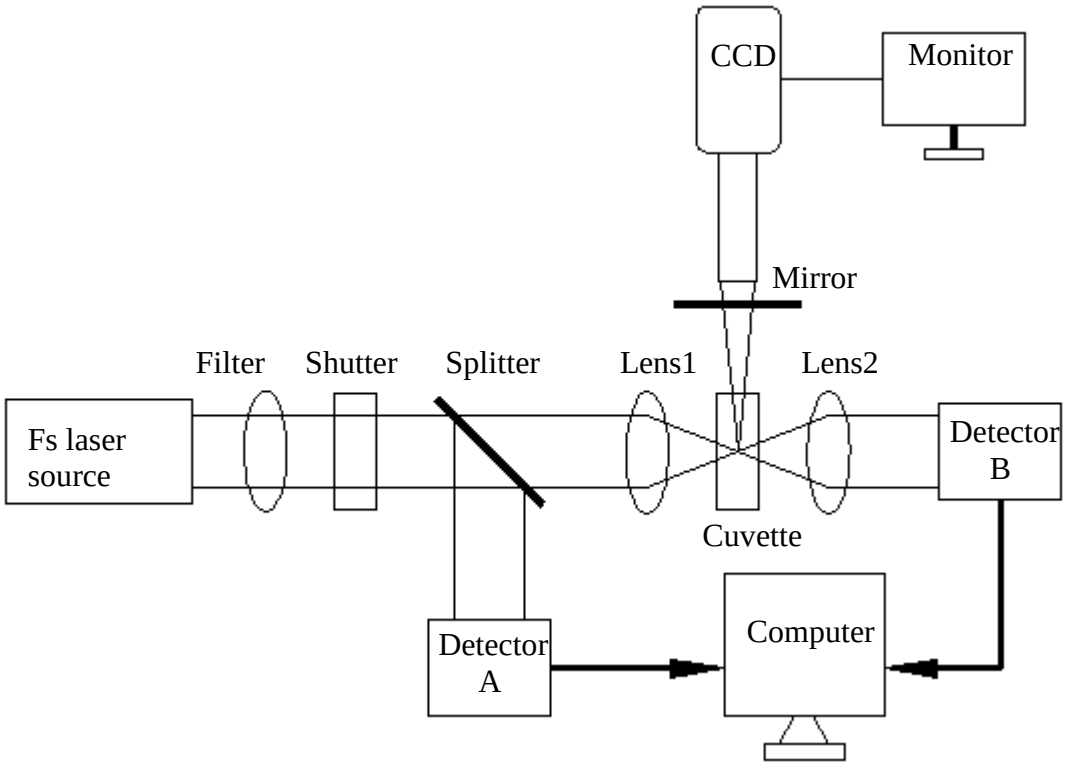

Figure 6.2 Optical Breakdown Threshold Measurement in Water

6.2.3 RESULTS AND DISCUSSION

Figure 6.3 shows the probability of vaporization in water by femtosecond laser amplifier. From the figure, it is known that the pulse energy threshold is 0.156 μJ (vaporization occurred at a probability of 0.5). Figure 6.4 shows the experiment result by a femtosecond oscillator, and the pulse energy threshold is 0.015 μJ . The pulse intensity threshold value achieved by an oscillator is less than 0.1 of that achieved by the amplifier. It benefits from the high pulse repetition rate of a femtosecond oscillator ($76\times10^6 Hz$). The working mechanisms may differ between the oscillator pulses of 76-MHz repetition rate and amplified pulses of 1 kHz repetition rate. Referring to reference [105], dissection at around 80 MHz repetition rate is performed in the low-density plasma regime well below the optical breakdown threshold and less than one order of magnitude higher than those used for nonlinear imaging. It is mediated by free-electroninduced chemical decomposition (bond breaking) in conjunction with multiphoton-induced chemistry, and is hardly related to heating or thermoelastic stresses. Dissection with 1-kHz repetition rate is performed using about 10-fold larger pulse energies and relies on thermoelastically induced formation of minute transient cavities that is probably facilitated by the free-electron-induced decomposition of biomolecules and by direct photochemistry.

Thereafter, a femtosecond oscillator together with a high numerical aperture objective and high repetition rate can overcome the pulse intensity threshold for optical breakdown. With a precise spot size, a pulse duration of around 200 fs and a repetition rate at 76MHz, only nanojoules pulse energy is necessary to achieve ablation. Potential intra tissue damage, which is dependent on the amount of applied laser energy, is minimized. The side effect such as self focusing may significantly reduced.

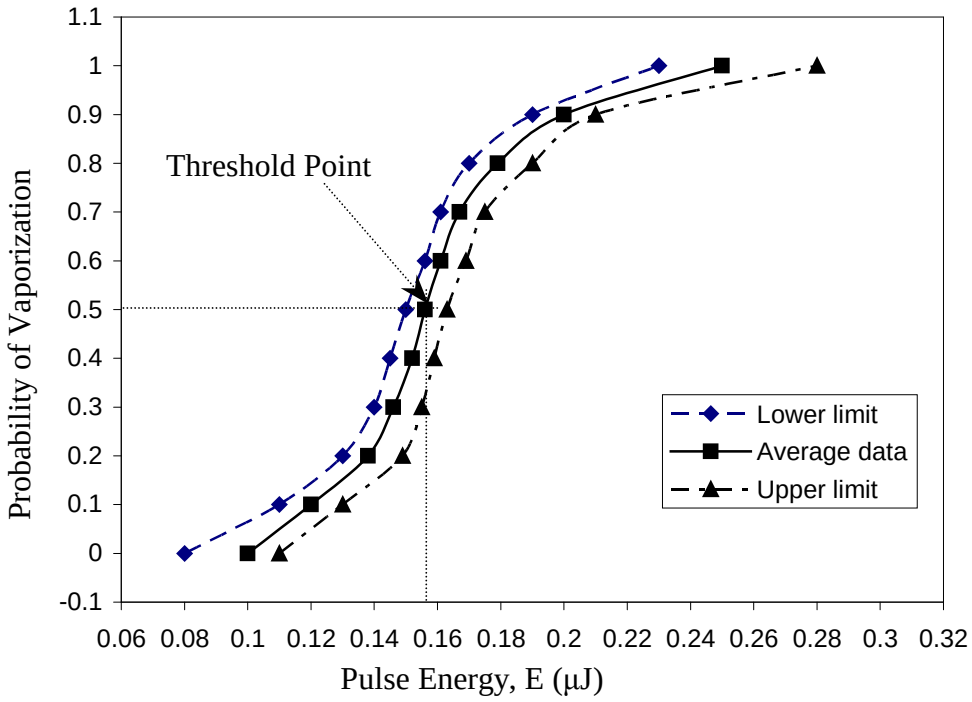

Figure 6.3 Probability of Vaporization in Water by a Femtosecond Amplifier

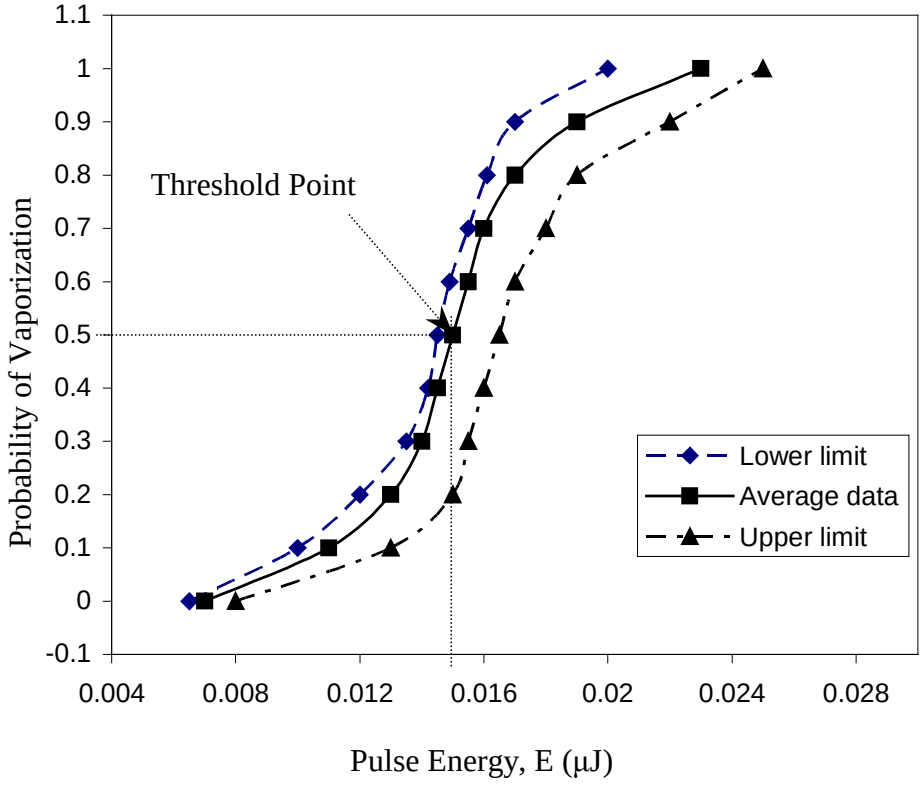

Figure 6.4 Probability of Vaporization in Water by a Femtosecond Oscillator

6.3 NANO JOULE PULSE ENERGY PROCESSING USING FEMTOSECOND OSCILLATOR

The samples were cornea and sclera from fresh pig eyes. For each sample, the light propagation observation experiments were conducted for five times in the same condition, and then the average data were used to perform the analysis.

Figure 6.5 shows the in-vitro experiment setup to record the light propagation process. It was almost the same as the setup shown in Figure 6.2. The laser source was a femtosecond oscillator. The maximum output power that can be produced by our femtosecond oscillator system and directed into the sample was 200 mW. The laser beam was focused 1 mm below the surface of the tissue sample. Through the CCD camera, the propagation status was shown simultaneously. The position of the CCD camera and the monitor were adjusted to observe the light propagation process in the ocular tissue. The detectors were used to measure the input and transmitted average power value. When the ratio of transmitted power (recorded by detector B) to input power (recorded by detector A) had a significant change, it meant that optical breakdown had occurred and the pulse energy deposited in the tissue was over the damage threshold. Using the measured power value, the corresponding laser pulse energy was calculated. The possibility of photodisruption was also investigated on the same experiment setup.

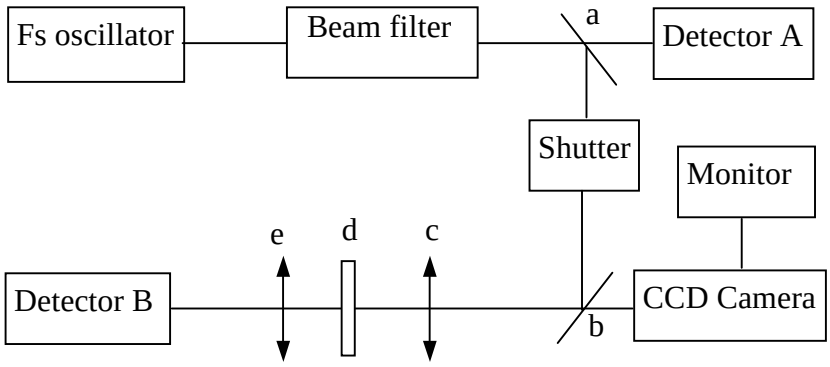

a: beam splitter; b: mirror with high reflection at 800 nm;
c: objective ($NA = 0.85$); d: tissue sample; e: focusing lens ($f = 50\ mm$)

Figure 6.5 Light Propagation and Energy Transmission Investigation Setup

Figure 6.6 shows the optical breakdown in cornea. During light propagation in cornea, when the power reached 60 mW, vaporization occurred. With power continuously increased, the output power was no longer linear with input power, as shown by the data recorded from the detectors A and B. The power value at which the light propagation changed from linear to nonlinear was defined as the critical power value for optical breakdown happening. The corresponding pulse intensity was the pulse intensity threshold, and subsequently, the pulse energy threshold E_{th} was calculated. In this experiment $E_{th} = 47.4\,\text{nJ}$. The Photodisruption happened when the output power increased to 115 mW, as shown in Figure 6.7.The corresponding pulse energy was 90.1 nJ.

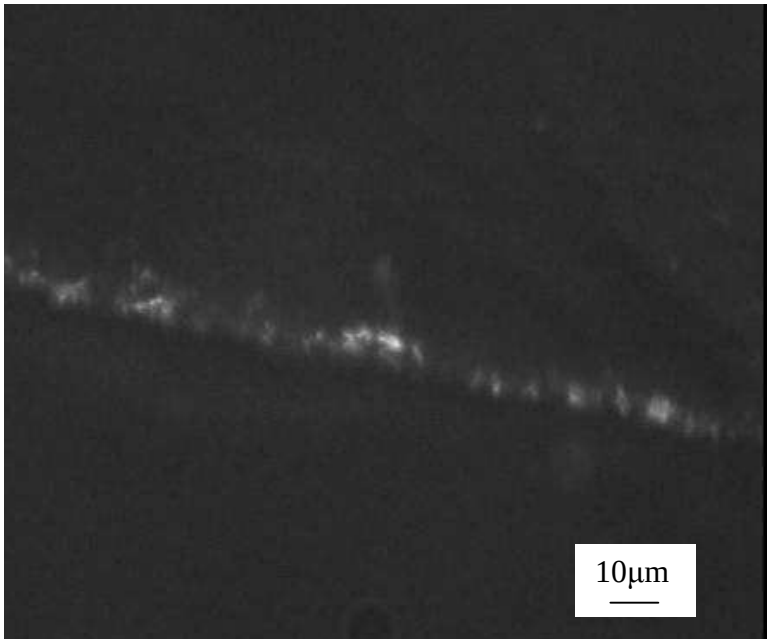

Figure 6.6 Vaporization in Cornea. ***NA*=0.85, *P = 60 mW*, E_{th} *= 47.4 nJ***

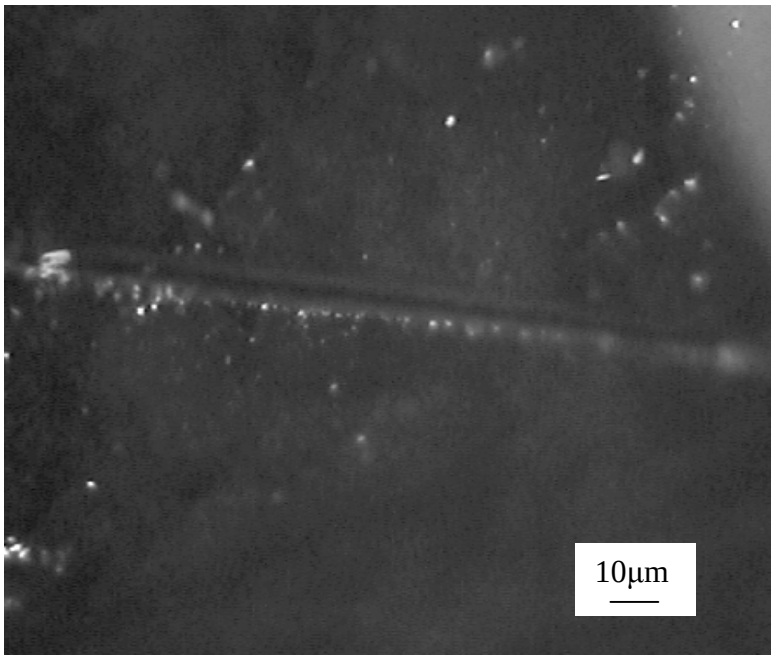

Figure 6.7 Photodisruption in Cornea. ***NA*=0.85, *P = 115 mW*, E_{th} *= 90.1 nJ***

Figure 6.8 shows the relationship between the input power and the transmitted power in sclera. The critical power value was roughly 170 mW. The corresponding energy threshold is 134 nJ. Below 170 mW, the input power and the transmitted power were in linear relationship; and above it, the relationship became nonlinear.

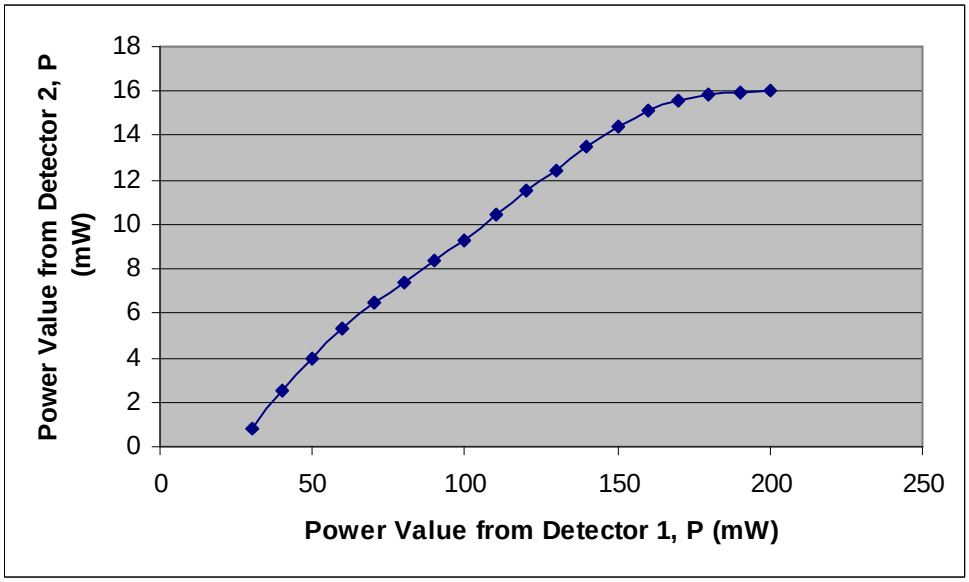

Figure 6.8 The Relationship between Input Power and Transmitted Power in Sclera

The results of light propagation in sclera show that optical breakdown may happen in fresh sclera; meanwhile, the ablation threshold cannot be reached with the current oscillator system. With some improvement on the femtosecond oscillator, such as adjustment of the repetition rate or using a higher NA objective [106, 107], there will be a possibility of photodisruption in the sclera.

6.4 SUMMARY

Both the femtosecond amplifier and the femtosecond oscillator were used for the measurement of femtosecond pulse intensity threshold in pure water. Through the vaporization probability analysis, it is known that the pulse energy threshold achieved by the oscillator is less than 0.1 of that achieved by amplifier. It benefits from the high pulse repetition rate of femtosecond oscillator ($76\times10^{6}\,Hz$). Dissection at high repetition rate is performed in the low-density plasma regime well below the optical

breakdown threshold and less than one order of magnitude higher than those used for nonlinear imaging, therefore pulse energy necessary for optical breakdown decreases.

In order to validate the feasibility of nano Joule pulse energy processing in glaucoma treatment, the light propagation in ocular tissue was investigated using a femtosecond oscillator. For pig cornea, nonlinear effects could occur in the tissue with 47.4 nJ pulse energy. Photodisruption in cornea could be achieved with 90.1 nJ pulse energy. For sclera, higher pulse energy was needed for optical breakdown. With some improvement on the femtosecond oscillator system, nanojoule pulse energy processing may be realized, which can minimize the intra tissue damage.

CHAPTER SEVEN

CONCLUSIONS AND RECOMMENDATIONS FOR FUTURE WORK

7.1 CONCULSIONS

The aim of this research was to apply femtosecond laser technology in glaucoma treatment. To study the feasibility of the femtosecond laser in iridotomy, a modified moving breakdown theory was applied to predict the breakdown threshold; thermal increase was calculated using the Heat Affect Zone model. A Monte Carlo simulation on light propagation in ocular tissue was performed for cyclophotocoagulation application. To investigate breakdown threshold and steady state ablation process, an in-vitro experimental study on fresh pig eye was performed using the amplified femtosecond laser system. Nano Joule pulse energy processing was investigated using femtosecond oscillator. The overall theoretical and experimental conclusions are summarized in the following sections.

7.1.1 OPTICAL BREAKDOWN THRESHOLD AND THERMAL INCREASE ANALYSIS FOR LASER IRIDOTOMY

Laser iridotomy is one of main types of the laser surgical methods for glaucoma treatment. To study the potential of femtosecond laser in iridotomy, the optical breakdown threshold in water was investigated. The corresponding thermal increases were calculated both in water and ocular tissues.

A femtosecond moving breakdown model was established to describe the femtosecond laser induced optical breakdown process. The comparison of the time dependent intensity in the focal region from nanosecond laser to femtosecond laser shows that, the pulse propagation should be taken into account during femtosecond laser processing.

For the laser-induced optical breakdown in water, from nanosecond region to femtosecond region, the pulse intensity threshold increases around 3 orders of magnitude, and the corresponding pulse energy threshold for optical breakdown decreases near to 3 orders of magnitude. Therefore there is potential to reduce the collateral damage.

For the thermal increase, in the nanosecond region, the temperature increase is over 100 K. While, with pulse duration decreasing, the temperature increase decreases rapidly. In femtosecond region, the temperature increase is less than 5 K for all the wavelengths studied. The results of thermal increase in femtosecond range show the safety of femtosecond pulses during laser-ocular tissue interaction.

7.1.2 MONTE CARLO SIMULATION ON LIGHT PROPAGATION IN MULTILAYERED OCULAR TISSUE FOR CYCLOPHOTO-COAGULATION

To investigate the potential of femtosecond laser in cyclophotocoagulation, light propagation in multilayered ocular tissue was numerically simulated.

Firstly, a multilayered model was established consisting of conjunctiva, sclera, ciliary muscle, and ciliary P.E. The optical properties of porcine ocular tissues were measured. An inverse adding-doubling algorithm was used to calculate the absorption coefficient and scattering coefficient. Then, light propagation was investigated at three different laser wavelengths (Argon at 488 nm, Ti:Sapphire at 800 nm, and YAG at 1064 nm). The results show that, among these three lasers, Argon laser has the largest radial expansion and has the smallest penetration depth. Inversely, YAG laser has a smallest radial expansion and has the largest penetrating nature. Ti:Sapphire shows a higher possibility of photon absorption compared to YAG laser. The results are essential for further study on femtosecond applications in cyclophotocoagulation.

7.1.3 KEY LASER PARAMETERS INVESTIGATION FOR TISSUE ABLATION

- **Wavelength**

During light propagation in the tissue, the wavelength affects the amount of scattering and absorption. It is not always a linear relationship between wavelength and the coefficients of scattering and absorption.

- **Pulse Duration**

The optical breakdown threshold is strongly dependent on pulse duration. With pulse duration decreasing, pulse energy threshold for optical breakdown can be reduced. Therefore the side effect during the laser tissue interaction can be limited to within an acceptable range.

- **Numerical Aperture**

Numerical aperture (NA) directly affects the energy density during laser processing. Smaller NA results in a smaller rate of multiphoton absorption, and thus a smaller ablation rate. Larger NA allows well-localized energy deposition at a low breakdown threshold. Meanwhile, conversion efficiency into mechanical energy may be associated with large NA, and it has the possibility for increasing the likelihood of mechanically induced side effects.

- **Pulse Intensity**

The electric field strength relies on laser pulse intensity. Due to the high pulse intensity, nonlinear effects can easily occur in the femtosecond region. The pulse duration and the repetition rate of our laser system is pre-set, therefore the laser pulse intensity depends on the output power.

- **Pulse Numbers**

Appropriate pulse numbers are necessary to achieve a desirable tissue ablation. The pulse number is controlled by the scanning speed and repetition frequency. With a fixed repetition frequency in our femtosecond laser system, the scanning speed at 0.3 mm/s was suitable for the in-vitro experiment study.

7.1.4 IN-VITRO EXPERIMENT USING FEMTOSECOND LASER AMPLIFIER SYSTEM

The optical breakdown threshold and the steady state ablation were studied through in-vitro experiment using femtosecond Ti:Sapphire laser system with amplifier equipment.

For the ablation threshold, fresh pig iris was used as the sample. Using a probability plotting method, the laser pulse intensity at 50% probability of ablation point was defined as the ablation threshold. Our experimental results show that the threshold intensity of iris ablation was about $1.7x10^{14}$ W/cm^2.

For steady-state ablation, besides minimal laser pulse intensity being necessary to reach the ablation threshold, a certain amount of energy and exposure time is also needed. In our in-vitro experimentation, a 50 μm-diameter hole can be ablated using 4.1 mJ energy; for a 90 μm-diameter hole, total energy of 8.4 mJ was needed.

7.1.5 NANO JOULE PULSE ENERGY PROCESSING USING FEMTOSECOND OSCILLATIR

To investigate the advantages of biomedical processing with a femtosecond oscillator, two laser sources (a femtosecond amplifier and a femtosecond oscillator) were used to measure the pulse intensity threshold in pure water for optical breakdown. The analysis of vaporization probability shows that the pulse energy threshold achieved by the oscillator is less than 0.1 of that achieved by using the amplifier.

The femtosecond oscillator system was then used to investigate the nanoJoule processing of ocular tissues. The aim was to overcome the limitations accompanied with a femtosecond amplifier system, such as high cost and possible intra-tissue damage. For light propagation in a pig cornea, the nonlinear effect occurred in the tissue during light propagation when the power reached 60 mW,

and the corresponding pulse energy was 47.4 nJ. Photodisruption in cornea could be achieved when the power equaled 115 mW, and the corresponding pulse energy was 90.1 nJ. For sclera, the optical breakdown can occur when the input power reached 170 mW. The corresponding pulse energy was 134 nJ.

7.2 RECOMMENDATIONS FOR FUTURE WORK

To develop a new instrument or a surgery procedure, typically large experimental and clinical studies are involved. Following up this research, the recommendations for future work are as follows.

- **Further In-Vitro Experimental Study**

An in-vitro experiment study has been carried out in this research; meanwhile, some aspects need to be further studied, which has not been done due to the breakdown of our amplified femtosecond laser system. In the proposed in-vitro experiment study, the optical set-up could be optimized (e.g. objective lens with bigger numerical aperture value) and better results could be expected. Histological analysis should be carried out using optical coherence tomography (OCT); both ablation size and depth can be exactly measured.

- **In-Vivo Experimental Study**

In-vivo experimentation could be performed on rat’s eyes. To observe the ablation effect, the level of intro-ocular pressure should be monitored in regular time interval after laser processing.

Ultimately, based on the in-vitro and in-vivo results, an optimized setup will be designed and tested, which is expected to improve the efficiency and minimize the collateral damage during laser glaucoma surgery.

RELATED PUBLICATIONS

Journal Papers:

1. B. K. A. Ngoi, D. X. Hou, L. H. K. Koh, S. T. Hoh. (2005). Femtosecond Laser for Glaucoma Treatment: A Study on Ablation Energy in Pig Iris. Lasers in Medical Science. 19 (4), 218-222.
2. B. K. A. Ngoi, D. X. Hou, S. T. Hoh, L. H. K. Koh, Y.Z. Deng. In-vitro Experiment Study on Ablation Parameters in Femtosecond-Ocular Tissue Interaction. Special Issue in International Journal of Nanoscience. International Journal of Nanoscience. 4(4), 483-488.

Conference Papers:

3. D. X. Hou, B. K. A. Ngoi, S. T. Hoh, L. H. K. Koh, Y. Z. Deng. (2004). the Comparison between Simulation and Experimentation Results on Ocular Tissue Removal, the International Conference on Experimental Mechanics.
4. D. X. Hou, B. K. A. Ngoi, S.T. Hoh, Z. W. Jiang, L.H. K. Koh. (2005). Light Propagation in Ocular Tissue with Femtosecond Oscillator at 800nm Wavelength. Proceedings of the International Symposium on Photonics, Biophotonics, and Nanophotonics'05. Chinese Optics Letters. 3.147-149.

REFERENCES

1. Breck Hitz, J.J. Ewing, Jeff Hecht (2001). Introduction to Laser Technology (3rd edition). New York: Wiley-IEEE Press.
2. Muncheryan, H.M. (1979). Laser Technology. Indianapolis: Howard W. Sams.
3. Hitz, C. Breck. (1985). Understanding Laser Technology: an Intuitive Introduction to Basic and Advanced Laser Concepts. Tulsa, Okla.: PennWell Books,
4. Silfvast, W.T. (1996). Laser Fundamentals. Cambridge, UK: Cambridge University Press.
5. Nolte, S., Kamlage, G., Korte, F., Bauer, T., Wagner, T., Ostendorf, A., Fallnich, C., & Welling, H. (2000). Microstructuring with Femtosecond Lasers. Advanced Engineering Materials, 2(1-2), 23-27.
6. Vogel, A., Venugopalan, V. (2003). Mechanisms of Pulsed Laser Ablation of Biological Tissues. Chemical Reviews, 103, 577-644
7. Fiscella, R.D. (2002). Pharmacological Considerations in the Treatment of Glaucoma. Managed Care: New Treatments for Eye Disease, 11(1), 16-20.
8. Sim, D.H.J (1999). Glaucoma Update- What Physicians and the Public Need To Know. Singapore Medical Journal, 40 (04).

9. Sacks ZS, Kurtz RM, Juhasz T, Mourau GA (2002). High Precision Subsurface Photodisruption in Human Sclera. Journal of Biomedical Optics 7(3), 442-450

10. Z. S. Sacks, F. Loesel, C. Durfee, R. M. Kurtz, T. Juhasz, and G. Mourou. (1998). Transscleral Photodisruption for the Treatment of Glaucoma. Light Scattering Technologies in Mechanics, Biomedicine and Material Science, Saratov Fall Meeting '98.

11. Z.S. Sacks, R.M. Kurtz, T. Juhasz, and G. Mourou. (2001). Femtosecond subsurface photodisruption in scattering human tissues using long infrared wavelengths. Proceedings of SPIE, 4241, 98-111.

12. Dausinger, F. (2003). Femtosecond Technology for Precision Manufacturing: Fundamental and Technical Aspects. RIKEN Review, 50, 77-82.

13. Rizvi, N.H. (2003). Femtosecond Laser Micromachining: Current Status and Applications. RIKEN Review, 50, 107-112.

14. Liu, X., Du, D. & Mourou, G. (1997). Laser Ablation and Micromachining with Ultrashort Laser Pulses. Journal of Quantum Electronics (IEEE), 33(10), 1706-1717.

15. Phipps, C. (2003). Laser Applications Overview: The State of the Art and the Future Trend in the United States. RIKEN Review, 50, 11-19.

16. Clark-MXR, Inc. (2003). Micromachining Handbook. Retrieved June 19, 2003, from the World Wide Web: http://www.cmxr.com/Industrial/Handbook/Introduction.htm

17. Fertein, E., Przygodzki, C., Delbarre, H., Hidayat, A., Douay, M. & Niay, P. (2001). Refractive-Index Changes of Standard Telecommunication Fibre

through Exposure to Femtosecond Laser Pulses at 810 cm. Applied Optics, 40 (21), 35063508.

18. Endert, H. Galvanauskas, A., Sucha, G., Patel, R. & Stock, M. (2002). Novel Ultrashort Pulse Fiber Lasers for Micromachining Applications. RIKEN Review, 43, 23-76.

19. Kondo, Y., Nouchi, K. & Mitsuyu, T. (1999). Fabrication of Long-Period Fiber Gratings by Focused Irradiation of Infrared Femtosecond Laser Pulses. Optics Letters, 24 (10), 646-648.

20. Hosokawa, Y., Mito, T., Tada, T., Asahi, T. & Masuhara, H. (2002). Laser-Induced Expansion and Ablation Mechanisms of Organic Materials. RIKEN Review, 43, 35-40.

21. Nakashima, S., Mizoguchi, K., Harima, H. & Sakai, K. (1998). Coherent Phonon Oscillations in Photo-Excited Semiconductors and Semimetals. Journal of Luminescence, 76&77, 6-14.

22. Bonchik, A.Y., Kijak, S.G., Gotra, Z. & Proszak, W. (2001). Laser Technology for Submicron-Doped Layers Formation in Semiconductor. Optics & Laser Technology, 33 (8), 589-591.

23. Kostrubiec, R., Lisik, Z., Pawlak, R., Jakubowska, K. & Korbicki, A. (2001). New Laser Technology for wire Bonding in Power Devices. Microelectronics Journal, 32 (5-6), 543-546.

24. M. Meunier, B. Fisette, A. Houle, A. V. Kabashin, S. V. Broude, P. Miller, (2003). Processing of Materials and Semiconductors by a Femtosecond Laser-Based Microfabrication System. SPIE Conference Proceedings, USE V. 6 4978-32

25. Wu, R., Xie, C.S., Hu, M., & Cai, W.P. (2000). Laser-Melted Surface Layer of Steel X165CrMoV12-1 and its Tempering Characteristics. Materials Science and Engineering A: Structural Materials: Properties, Microstructure and Processing, 278 (1-2), 1-4.

26. Ostendorf, A., Kamlage, G. & Chichkov, B.N. (2003). Precise Deep Drilling of Metals by Femtosecond Laser Pulses. RIKEN Review, 50, 87-89.

27. Alessio, L.D., Ferro, D., Marotta, V., Santagata, A., Teghil, R. & Zaccagnino, M. (2001). Laser Ablation and Deposition of Bioglass 45S5 Thin Films. Applied Surface Science, 183 (1-2), 10-17.

28. Wu, P.K., Ringeisen, B.R., Callahan, J., Brooks, M., Bubb, D.M., Wu, H. D., Pique, A., Spargo, B., McGill, R.A. & Chrisey, D.B. (2001). The Deposition, Structure, Pattern Deposition and Activity of Biomaterial Thin-Films by Matrix-Assisted Pulsed-Laser Evaporation (MAPLE) and MAPLE Direct Write. Thin Solid Films, 398-399, 607-614.

29. Mello, A.P., Bari, M.A. & Prendergast, P.J. (2002). A Comparison of Excimer Laser Etching and Dry Etching Process for Surface Fabrication of Biomaterials. Journal of Materials Processing Technology, 124 (3), 284-292.

30. D'Alessio, L., Teghil, R., Zaccagnino, M., Zaccardo, I., Ferro, D. & Marotta, V. (1999). Pulsed Laser Ablation and Deposition of Bioactive Glass as Coating Material for Biomedical Applications. Applied Surface Science, 138-139, 527-532.

31. Odde, D.J. & Renn, M.J. (1999). Laser-Direct Writing for Applications in Biotechnology. Tibtech, 17, 385-389.

32. Ball, M.D., Downes, S., Scotchford, C.A., Antonov, E.N., Bagratashvili, V.N., Popov, V.K., Lo, W.J., Grant, D.M. & Howdle, S.M. (2001) Osteoblast Growth on Titanium Foils Coated with Hydroxyapatite by Pulsed Laser Ablation. Biomaterials, 22 (4), 337-347.

33. Lootz, D., Behrend, D., Kramer, S., Freier, T., Haubold, A. & BenkieBer, G. (2001). Laser Cutting: Influence on Morphological and Physicochemical Properties of Polyhydroxybutyrate. Biomaterials, 22 (18), 2447-2452.

34. Sackmann, E. & Tanaka, M. (2000). Supported Membranes on Soft Polymer Cushions: Fabrication, Characterization and Applications. Tibtech, 18, 58-64.

35. Georgi Graschew, Matthias Bastian, Stefan Rakowsky, Theo A. Roelofs, Evangelos Balanos, Peter M. Schlag, Günter Steinmeyer, Thomas Elsaesser. (2004). Development of an Applicator for Multiphoton PDT. Proceedings of SPIE – Volume 5463, Femtosecond Laser Applications in Biology, 68-74.

36. P. Vérant, R. Serduc, J. A. Coles, R. Farion, C. Rémy, B. van der Sanden, J.C. Vial. (2004). A Method for Measuring Cerebral Blood Volume of Mouse using Multiphoton Laser Scanning Microscopy. Proceedings of SPIE – Volume 5463 Femtosecond Laser Applications in Biology, 1-12.

37. Muller, G., Dorschel, K. & Kar, H. (1991). The Tissue Photoablation Process with Short Pulsed Lasers. Bioptics: Optics in Biomedicine and Environmental Sciences, Proceedings of SPIE, 1524, 150-177.

38. Markolf H. Niemz. (1996). Laser-Tissue Interactions Fundamentals and Applications. Springer.

39. Lin, W.C., Motamedi, M. & Welch, A.J. (1995). Nonlinear Optical Behavior of Ocular Tissue during Laser Irradiation. Applied Optics, 34 (34), 7979-7985.

40. Mcham, M.L., Eisenberg, D.L., Schuman, J.S. & Wang, N. (1997) Eerbium: Yag Laser Trabecular Ablation with a Sapphire Optical Fiber. Experimental Eye Research, 65 (2), 151-155.

41. Andrea K. Ives, Wei R. Chen, Baha Jassemnejad, Kenneth E. Bartels, Hong Liu, John A. Nordquist, Robert E. Nordquist. (2000). Laser-Tissue Photothermal Interaction and Tissue Temperature Change. Laser-Tissue Interaction XI: Photochemical, Photothermal, and Photomechanical. Proceedings of SPIE, 3914.

42. Yingling, Y.G., Garrison, B.J. (2003). Photochemical Ablation of Organic Solids. Nuclear Instruments and Methods in Physics Research Section B: Beam Interactions with Materials and Atoms, 202, 188-194.

43. Lubatschowski, H., Heisterkamp, A., Will, F., Serbin, J., Bauer, T., Fallnich, C., Welling, H., Muller, W., Schwab, B., Singh, A.I. & Ertmer, W. (2002). Ultrafast Laser Pulses for Medical Applications. Commercial and Biomedical Applications of Ultrafast and Free-Electron Lasers, Proceedings of SPIE, 4633, 38-49.

44. G. Fabian Will, Ajoy Singh, Wolfgang Ertmer, Herbert Welling, Holger Lubatschowski. Extraluminal laser angioplasty (ELAN), a New Method for Treating Atherosclerotic Vessels. (2003). Proceedings of SPIE. 4949, p 477-87.

45. Konig, K., Krauss, O. & Riemann, I. (2002). Intratissue Surgery with 80 MHz Nanojoule Femtosecond Laser Pulses in the Near Infrared. Optics Express, 10 (3), 171-176.

46. Serbin, J., Bauer, T., Fallnich, C., Kasenbacher, A. & Arnold, W.H. (2002). Femtosecond Lasers as Novel Tool in Dental Surgery. Applied Surface Science, 8101, 1-4.

47. A. V. Rode, E. G. Gamaly, B. Luther-Davies, B. T. Taylor and J. Dawes, A. Chan, R. M. Lowe and P. Hannaford. (2002). Subpicosecond laser ablation of dental enamel. Journal of Applied Physics, 92 (4), 2153-2158.

48. Ali Javey. Laser Angioplasty: Applications of Excimer Lasers in Angioplasty. Retrieved June 19, 2003, from the World Wide Web: http://www.geocities.com/CapeCanaveral/Lab/3628/laser-angioplasty.html

49. Thompson, K.P., Ren, Q.S. & Parel, J.M. (2002). Therapeutic and Diagnostic Application of Lasers in Ophthalmology. In R.W. Waynant (Ed), Lasers in Medicine, 211-245. Boca Raton, USA: CRC Press LLC.

50. Steven F. Barrett, Cameron H. G. Wright and Ashley J. Welch (2002). Laser Ophthalmology. In D. R. Vij and K. Mahesh (Ed), Medical Applications of Lasers. Kluwer Academic Publishers.

51. Chao-Chien Hu, Hsuei-Yuh Lu, Hung-Che Chen, Cheng-Kuo Cheng and Chun-Nan Chen. (2005). Clinical Experience with Bausch & Lomb Technolas-217 Excimer Laser. Optical and Quantum Electronics, 37, 1457 – 1463.

52. Tingrui Pan, Matthew S. Stay, Victor H. Barocas, J. David Brown, and Babak Ziaie. (2005). Modeling and Characterization of a Valved Glaucoma

Drainage Device With Implications for Enhanced Therapeutic Efficacy. IEEE Transactions and Biomedical Engineering, 52 (5), 948-951.

53. University Eye Specialists: Glaucoma. Retrieved September 10, 2002, from the World Wide Web: http://www.ueseyecare.com/Glaucoma.htm

54. Pimentel, R.L., Carvalho, R.A., Oliveira, H.C., Goncalves, D.C., Silva, L.M. & Costa, V.P. Discrimination between Normal and Glaucomatous Eyes with Visual Field and Scanning Laser Polarimetry Measurements. British Journal of Ophthalmology, 85, 586-591.

55. Franck Villain, Jean-Marie PareI , Katakn Kiss, Rhard K. Parrish, François Kuhne, Yoshiko Takesue1, Patrick Hostyn, (1993). Laser Scierectomy and 5-FU controlled Drug Release Biodegradable Implant for Glaucoma Therapy. SPIE Proceedings: Ophthalmic Technologies III, 1877.

56. PATIENT INFO: Argon Laser Trabeculoplasty (ALT). Retrieved September 04, 2002, from the World Wide Web: http://www.djo.harvard.edu/meei/PI/glaucoma/ALT.html

57. Eye Procedures. Retrieved September 04, 2002, from the World Wide Web: http://www.eyemdlink.com/EyeProcedures.asp

58. Schwartz LW, Moster MR, Spaeth GL. (1986). Nd:YAG Laser Iridectomies in Glaucoma Associated with Closed or Occludable Angles. America Journal of Ophthalmology, 102, 41-4.

59. Del Priore LV, Robin AL, Pollack IP. (1988). Neodymium:YAG and Argon Laser Iridotomy –Long Term Follow-up in a Prospective, Randomized Clinical Trial. Ophthalmology, 95, 1207-11.

60. Zysset B, Fujimoto JG, Puliafito CA. (1989). Picosecond Optical Breakdown: Tissue Effects and Reduction of Collateral Damage. Lasers in Surgery and Medicine, 9, 193-204.

61. Vogel A, Busch S, Jungnickel K. (1994). Mechanisms of Intraocular Photodisruption with Picosecond and Nanosecond Laser Pulses. Lasers in Surgery and Medicine, 15, 32-43.

62. Vogel A, Busch S, Parlitz O. (1996). Shock Wave Emission and Cavitation Bubble Generation by Picosecond and Nanosecond Optical Breakdown in Water. Journal of Acoustic Society of America, 100, 148-65.

63. Gerd Geerling, Johann Roider, Ursula Schmidt-Erfurt, Kester Nahen, El-Sayed El-Hifnawi, Horst Laqua, Alfred Vogel. (1998). Initial Clinical Experience with the Picosecond Nd:YLF Laser for Intraocular Therapeutic Applications. British Journal of Ophthalmology, 82, 504-509.

64. Sami Toyran, Yaoming Liu, Sima Sinha, Sun Shan, Michael R. Cho, Robert J. Gordon, Deepak P. Edward. (2005). Femtosecond Laser Photodisruption of Human Trabecular Meshwork: an in Vitro Study. Experimental Eye Research, 81, 298-305.

65. Oraevsky, A.A., Da Silva, L.B., Rubenchik, A.M., Feit, M.D., Glinsky, M.E., Perry, M.D., Mammini, B.M., Small, W., Stuart, B.C.. (1996). Plasma mediated ablation of biological tissues with nanosecond to femtosecond laser pulses: relative role linear and nonlinear absorption. IEEE Journal of Selected Topics in Quantum Electronics, 2, 801-809.

66. Fan, C.H. & Longtin, J.P. (2001). Modelling Optical Breakdown Dielectrics during Ultrafast Laser Processing. Applied Optics, 40 (18), 3124-3130.

67. Fan, C.H., Sun, J. & Longtin, J.P. (2002). Breakdown Threshold and Localized Electron Density in Water Induced by Ultrashort Laser Pulses. Journal of Applied Physics, 91 (4), 2530-2536.

68. Zhigilei, L.V. & Garrison, B.J. (2000). Microscopic Mechanisms of Laser Ablation of Organic Solids in the Thermal and Stress Confinement Irradiation Regimes. Journal of Applied Physics, 88 (3), 1281-1298.

69. F.H. Loesel, A.-C. Tien, S. Backus , H. Kapteyn, M. Murnane, R.M. Kurtz , S. Sayegh, T. Juhasz. (1999). Effect of Reduction of Laser Pulse Width from 100 ps to 20 fs on the Plasma-Mediated Ablation of Hard and Soft Tissue. Proceedings of SPIE - The International Society for Optical Engineering, 3565, 116-123.

70. Heisterkamp, A., Ripken, T., Mamom, T., Drommer, W., Welling, H., Ertmer, W. & Lubatschowski, H. (2002). Nonlinear Side Effects of fs Pulses Inside Corneal Tissue during Photodisruption. Applied Physics B: Lasers and Optics, 74 (4-5), 419-425.

71. Schuöcker, D., 1999, High Power Lasers in Production Engineering, Imperial College. Press and World Scientific Publishing Co.

72. Kaiser, A., Rethfeld, B., Vicanek, M. & Simon, G. (2000). Microscopic Processes in Dielectrics under Irradiation by Subpicosecond Laser Pulses. Physical Review B, 61 (17), 437-450.

73. Docchio, F. (1991). Nd:YAG laser Ophthalmic Microsurgery. In M.L. Wolbarsht (Ed), Laser Applications in Medicine and Biology, Volume 5:. 85-140. New York, USA: Plenum Press.

74. Gan, C.H. & Longtin, J.P. (2000). Modelling of Moving Breakdown by Femtosecond Laser Pulses in Dielectrics. ASME International Mechanical Engineering Congress and Exposition, 3, 187-194.

75. Ramsden, S. A., and Savic, P.. (1964). A Radiative Detonation Model for the Development of A Laser-Induced Spark in Air. Nature, 203-217

76. Alcock, A. J., De Michelis, C., Hamal, K., and Tozer, B. A.. (1968) Expansion Mechanism in A Laser-Produced Spark. Physics Review Letter, 20: 1095.

77. 3 Meyer, I., and Stritzke, P.. (1976). Expansion of Laser Sparks Produced by a Mode-Locked Nd:glass Laser. Applied Physics, 10:125.

78. Raizer, Y. P. (1966). Breakdown and Heating of Gases under the Influence of A Laser Beam. Soviet Physics Uspekhi, 8:650.

79. Kester Nahen, Alfred Vogel. (1996). Plasma Formation in Water by Picosecond and Nanosecond Nd:YAG Laser Pulses—Part II: Transmission, Scattering, and Reflection. IEEE Journal of Selected Topics in Quantum Electronics, 2 (4).

80. Fan, C.H., Longtin, J.P. (2000). Modeling of moving breakdown by femtosecond laser pulses in dielectrics. ASME International Mechanical Engineering Congress and Exposition, 366,187-194.

81. Joachim Noack, Alfred Vogel. (1999). Laser-Induced Plasma Formation in Water at Nanosecond to Femtosecond Time Scales: Calculation of Thresholds, Absorption Coefficients, and Energy Density. IEEE Journal of Quantum Electronics. 35 (18), 1156-1167.

82. Oraevsky, A.A., Da Silva, L.B., Rubenchik, A.M., Feit, M.D., Glinsky, M.E., Perry, M.D., Mammini, B.M., Small, W., Stuart, B.C.. (1996).

Plasma mediated ablation of biological tissues with nanosecond to femtosecond laser pulses: relative role linear and nonlinear absorption. IEEE Journal of Selected Topics in Quantum Electronics. 2, 801-809

83. Vogel, A., Noack, J., Nahen, K., Theisen, D. Busch, S., Parlitz, U., Hammer, D.X., Noojin, G.D. & Rockwell, B.A. (1999). Energy Balance of Optical Breakdown in Water at Nanosecond to Femtosecond Time Scales. Applied Physics B: Lasers and Optics, 68 (2), 271-280.

84. Dickinson, J.T. (2002). Physical and Chemical Aspects of Laser-Materials Interactions Relevant to Laser Processing. Photon Processing in Microelectronics and Photonics, SPIE Conference Proceedings, 4637, 453-464.

85. Umit Cicekli. (2003). Computational Model for Heat Transfer in the Human Eye Using the Finite Element Method. Moscow State University of Civil Engineering, Russia.

86. Tuchin, V. (1999). Tissue Optics: Light Scattering Methods and Instruments for Medical Diagnosis. Washington, USA: SPIE Press.

87. J. L. Boulnois. (1986). Photophysical Processes in Recent Medical Laser Developments: A Review. Lasers in Medical Science, 1, 47-66.

88. Zhigang Geng, Xiaojuan Zhang, Ying Liu. (2003). Phase Function of Tissue and the Properties of Optical Parameter γ. Proceedings of the SPIE - The International Society for Optical Engineering, 5254 (1:8-11), 415-19.

89. Prahl S,Van Gemert M,Welch A.(1993). Determining the Optical Properties of Turbid Media by Using the Addingdoubling Method. Applied Optics, 32, 559–68.

90. S C Gebhart, W C Lin, A Mahadevan-Jansen. (2006). In Vitro Determination of Normal and Neoplastic Human Brain Tissue Optical Properties Using Inverse Adding-Doubling. Physics in medicine and biology, 51, 2011–2027.

91. Babak Nemati, Andrew Dunn, Ashley J. Welch, H. Grady Rylander lll. (1998). Optical Model for Light Distribution During Transscleral Cyclophotocoagulation. Applied Optics. 37 (4), 764-771.

92. Barton, J.K., Pfefer, T.J., Welch, A.J., Smithies, D.J., Nelson, J.S. & Gemert, M.J.C. (1998). Optical Monte Carlo Modelling of a True Port Wine Stain Anatomy. Optics Express, 2 (9), 391-396.

93. Tianghong Dai, Brian M Pillula, Lihong V Wang and Bahman Anvari. (2004). Comparison of human skin opto-thermal response to near-infrared and visible laser irradiations: a thermal investigation. Physics in Medicine and Biology, 49, 4861-4877.

94. Zeifman, M.I., Garrison, B.J. & Zhigilei, L.V. (2002). Direct Simulation Monte Carlo Calculation: Strategies for Using Complex Initial Conditions. Material Research Society Symp. Proceedings, 731, 3.8.1-3.8.6.

95. Boas, C.A., Culver, J.P., Stott, J.J. & Dunn, A.K. (2002). Three Dimensional Monte Carlo Code for Photon Migration through Complex Heterogeneous Media including the Adult Human Head. Optics Express, 10 (3), 159-170.

96. Wang, X., Yao, G. & Wang. L.H. (2002). Monte Carlo Model and Single-Scattering Approximation of the Propagation of Polarized Light in Turbid Media Containing Glucose. Applied Optics, 41 (4), 792-801.

97. Lux I, L. Koblinger. (1991). Monte Carlo Particle Transport Methods: Neutron and Photon Calculations. CRC Press.

98. Lihong Wang, Steven L. Jacques. (1992). Monte Carlo Modeling of Light Transport in Multi-Layered Tissues in Standard C. Laser Biology Research Laboratory, University of Texas M. D. Anderson Cancer Center.

99. Claude Reiss. (1989). Ultrashort Laser Pulses in Biomedical Research. In M.L. Wolbarsht (Ed), Laser Applications in Medicine and Biology, Volume 4:133-165. New York, USA: Plenum Press.

100. Janet Voke. Lasers and Their Use in Ophthalmology Part 3. (2001). Optometry Today.

101. Sowka, J. (2002). Laser Therapy for Glaucoma. Retrieved December 01, 2002, from the World Wide Web: http://www.nova.edu

102. Karsten Konig, Oliver Krauss, Iris Riemann. (2002). Intratissue Surgery with 80 MHz Nanojoule Femtosecond Laser Pulses in the Near Infrared. Optics Express, 10 (3), 171-176.

103. Audrius Dubietis, Rytis Butkus, and Algis Petras Piskarskas. (2006). Trends in Chirped Pulse Optical Parametric Amplification. IEEE Journal of Selected Topics in Quantum Electronics, 12 (12), 163-172.

104. Operator's Manual: the Coherent Mira Model 900-B Laser. Coherent Laser Group.

105. A. vogel, J. noack, G. h¨uttman, G. paltauf. (2005). Mechanisms of Femtosecond Laser Nanosurgery of Cells and Tissues. Applied Physics, B 81, 1015–1047.

106. Ajit P. Joglekar, Gregory Spooner, Alan J. Hunt. (2002). Ultra Fast Laser Pulses for Cellular Nanosurgery with Minimum Collateral Damage. Proceedings of the Second Joint EMBS/BMES Conference, 1779-1780.

107. A. Heisterkamp, I. Z. Maxwell, E. Mazur, J. M. Underwood, J. A. Nickerson, S. Kumar, D. E. Ingber. (2005). Pulse Energy Dependence of Subcellular Dissection by Femtosecond Laser Pulses. Optics Express, 13 (10), 3690-3696.